Reduction in the Run-up Distance for the Deflagration-to-Detonation Transition and Applications to Pulse Detonation Combustion

vorgelegt von
Joshua Allen Terry Gray, M.Sc.
aus Savannah, GA (USA)

Von der Fakultät V – Verkehrs- und Maschinensysteme
der Technischen Universität Berlin
zur Erlangung des akademischen Grades

Doktor der Ingenieurwissenschaften
– Dr.-Ing. –

genehmigte Dissertation

Promotionsausschuss:

Vorsitzender:	Prof. Dr. rer. nat. Valentin Popov
Gutachter:	Prof. Dr.-Ing. Christian Oliver Paschereit
Gutachter:	Prof. Dr.-Ing. Jonas Pablo Moeck
Gutachter:	Prof. Ephraim Gutmark, Ph.D., D.Sc. (University of Cincinnati, USA)

Tag der wissenschaftlichen Aussprache: 11. Mai 2017

Berlin 2018

Danksagung

Dieses Manuskript ist die Zusammentragung von ausgewählten Arbeiten, die ich am „Institut für Strömungsmechanik und Technische Akustik“ als wissenschaftlicher Mitarbeiter seit Juli 2011 durchführte. Für die finanzielle Förderung möchte ich in erster Linie der Deutschen Forschungsgemeinschaft im Rahmen vom Sonderforschungsbereich 1029 „Signifikante Wirkungsgradsteigerung durch gezielte, interagierende Verbrennungs- und Strömungsinstationaritäten in Gasturbinen“ bedanken. Gleichzeitig verdienen die mutigen Wenigen meinen größten Respekt, die den SFB damals ins Leben riefen. Vor dem Beginn der ersten Phase des SFB in Juli 2012 wurde meine Arbeit durch eine Anschubfinanzierung unterstützt. Dafür möchte ich auch ganz herzlich dem Präsidium der TU Berlin danken.

Am Ende meines Bachelorsabschlusses in den USA habe ich einen Studienplatz für den Master und eine anschließende Doktorstelle gesucht. Durch Empfehlung rief ich eines Tages Professor C.O. Paschereit an. Herr Paschereit und Daniel Guyot haben mir auf dem langen Weg geholfen, einen Studienplatz in Deutschland zu bekommen, obwohl ich damals gar keine Deutschkenntnisse hatte. Durch die Jahren hat Herr Paschereit mich mit größtem Vertrauen begleitet. Dafür werde ich immer dankbar sein.

Nachdem ich in das Studium gelangte, kontaktierte mich Professor Valentin Popov. Daraus entstand eine mehrjährige Zusammenarbeit als Übersetzer im Bereich Kontaktmechanik, die nicht nur dazu diente mein Studium zu finanzieren, sondern auch einen signifikanten Einfluss auf meine Deutschkenntnisse nahm. Über unseren Tee und Kekse beim Korrekturlesen werde ich mich lang mit einem Lächeln erinnern.

Während meines Masterabschlusses hatte ich das Vergnügen Jonas Moeck kennen zu lernen und als mein vorgesehenes Projekt für die Doktorarbeit langsam eine Form annahm und er Professor wurde, hatte ich das Glück und die Freude ihn auch als Teilprojektleiter zu gewinnen. Jonas hatte trotz seiner vielen Verantwortung am Institut immer ein offenes Ohr für mich und seine Beratung und Betreuung waren unverzichtbar.

Heiko Stolpe war stets da, um ein klaffendes Loch in meinem Wissen, nämlich das von der Elektrotechnik, mit seiner Hilfe und Beratung zu füllen. Ohne ihn wären die Prüfstände, die für diese Arbeit nötig waren, nur mit sehr viel mehr Mühe und Ärger gelaufen und ich durfte meine Aufmerksamkeit auf andere Punkte verlegen.

Robert Bahnweg möchte ich mich auch zutiefst bedanken. Dass er meine verrückten Ideen immer wieder zu funktionierenden Gegenständen schaffte, war manchmal erstaunlich. Dazu, dass er sich nicht davon abschrecken ließ, selber verrückte Ideen einzustreuen, war auch eine große Hilfe und ein Vergnügen.

Sebastian Schimek habe ich auch sehr für seine Unterstützung in der Bereitstellung des Labors zu danken. Ich lernte viel bezüglich Laborauslegung von ihm. Er war immer bereit einen helfenden Vorschlag zu machen oder selbst die Arbeit zu unterstützen.

Andy Göhrs stand immer mit Rat und Tat bereit. Sei es mit der Infrastruktur, Beratung für einen großen Umbau, oder ein dringendes Teil, das in drei Stunden gefertigt sein musste, Andy hat mir immer eine helfende Hand angeboten.

Mit Georg Mensah hatte ich das Glück ein Büro zu teilen. Leider wird “fun with languages” kein riesiger YouTube-Erfolg, aber die aufregende Unterhaltungen zwischen uns, fachlich als auch privat, freuten mich sehr. Georg habe ich natürlich auch zu danken, dass er dieses Manuskript zur Druckerei gebracht hat, während ich anderweitig im Ausland beschäftigt war.

Ich möchte mich auch bei einigen von meinen ehemaligen Studenten ganz herzlich für ihren mehrjährigen Einsatz bedanken. Niclas Hanraths und Fatos Yücel wünsche ich viel Erfolg am Institut als neue Doktoranden im Bereich pulsierender Detonationsverbrennung. Robert Kanisch wünsche ich einen erfolgreichen Abschluss des Studiums und alles Gute für die Zukunft.

Den weiteren Kollegen sowohl am Hermann-Föttinger-Institut als auch im Sonderforschungsbereich 1029 möchte ich auch für ihre Freundschaft danken. Meine Zeit an der TU war durch den täglichen Interaktionen und schönen Konferenzen und Reisen erheblich bereichert. Leider gibt es zu viele wunderbare Menschen um hier alle gerecht namentlich zu erwähnen. Ich hoffe aber, dass sie wissen wie viel sie mir bedeuteten und ich freue mich schon sehr auf die vielen weiteren Jahre, die unser Freundschaften sicherlich noch halten werden.

Many thanks to Professor Ephraim Gutmark for offering his advice and support as we attempted to get our pulse detonation program off the ground. Also, I would like to thank him for reviewing this manuscript and for serving on my doctoral committee.

Professor Deanna Lacoste has been very patient and has afforded me much flexibility in my transition between being a doctoral student in Berlin and beginning my postdoctoral research at KAUST. Without this flexibility, the final corrected version of this manuscript may never have come into existence. For this, I would also like to thank her greatly.

I would like to offer my sincere gratitude to Professor Tim Lieuwen, Rajesh Rajaram and David Scarborough from my time at Georgia Tech, who gave me a chance as a young Bachelor’s student and inspired me to become professionally what I am today. It has been a long journey and I owe a lot of it to these three men.

Last but not least, an English phrase that Germans love to use in the midst of the most convoluted deutsche Sätze, I would like to thank my loving family. My parents and sister have been there for me throughout this long haul in a foreign land without reserve. They have always been supportive of my decisions and continue to support me as these decisions now lead me even farther away from those Georgia marshes of my childhood. I love you...

Zusammenfassung

Seit einigen Jahrzehnten ist die druckerhöhende Verbrennung ein aktiver Forschungsgegenstand. Aufgrund des Potenzials den Wirkungsgrad von Gasturbinen um mehr als 10% zu steigern, bietet sie eine Möglichkeit immer knapper werdende Ressourcen zu sparen und stetig verschärfte Emissionsgrenzwerte einzuhalten. Wenn Wasserstoff als Brennstoff verwendet wird, lässt sich sogar die Bildung des Treibhausgases CO2 völlig vermeiden. Wasserstoff kann durch Elektrolyse mit Hilfe erneuerbarer Energien gewonnen werden. Bei geringem Energiebedarf kann Wasserstoff auf Vorrat produziert und dann bei höherem Energiebedarf verfeuert werden. Aufgrund ihrer kurzen Lastwechselzeiten sind Gasturbinen ideal für einen solchen flexiblen Betrieb geeignet.

Eine Art der druckerhöhenden Verbrennung stellt die pulsierende Detonationsverbrennung dar. Bei diesem zyklischen Prozess wird der Brennstoff durch eine Detonationswelle, die sich mit einer Geschwindigkeit von bis zu 2000 m/s ausbreitet, verbrannt. Wegen der kurzen Verbrennungszeit findet keine Expansion des Gases statt und die gesamte freiwerdende Energie führt zu einer Erhöhung des Drucks und der Temperatur. Dies ist als Fickett-Jacobs-Zyklus bekannt. Typischerweise wird eine Flamme mit einer schwachen Zündquelle initiiert und so lange beschleunigt bis diese in eine Detonation übergeht. Dieser Vorgang heißt Deflagration-zu-Detonations-Transition (DDT) und ist das Hauptthema dieser Arbeit. Die Reduzierung der Detonationsanlaufstrecke hat einen direkten Einfluss auf den Wirkungsgrad. Daher ist es erstrebenswert die Anlaufstrecke so kurz wie möglich zu gestalten.

In dieser Dissertation werden diverse Methoden zur Verkürzung der Anlaufstrecke diskutiert. Experimentelle Untersuchungen der initialen Flammenbeschleunigung durch ein Hindernis zeigten, dass das Verblockungsverhältnis der maßgebliche geometrische Parameter für dieses Hindernis ist. Bei Verwendung mehrerer Hindernisse zeigte sich, dass der optimale Abstand zwischen diesen bei knapp über zwei Rohrdurchmessern liegt. Untersuchung an einem anderen Prüfstand bestätigten diese Ergebnisse. Weiterhin stellte sich heraus, dass ein Rohrdurchmesser von ca. 40 mm nötig ist, um die DDT innerhalb einer angemessenen Anlaufstrecke zu garantieren.

Die Ergebnisse dieser Vorstudien halfen einen modularen Prüfstand für die pulsierende Detonationsverbrennung zu entwerfen. Das Gas wurde mit Sauerstoff angereichert, um die Betriebsbedingungen in einer Kleingasturbine zu simulieren. Dabei konnte eine DDT mit nur 2-3 Blenden erreicht werden, wenn der Detonationskammereinlass reflektierend geformt wurde, um die initiale Flammenbeschleunigung zu begünstigen. Weitere Untersuchungen mit einer stoß-fokussierenden Düse ermöglichten eine zuverlässige DDT auf einer Länge von 158 mm. Bei dieser Düse wird eine lokale Explosion vor einer stark beschleunigenden turbulenten Flamme durch Reflektion und Fokussierung des führenden Stoßes eingeleitet. Dadurch wird der Druck in der Umgebung des Fokus um mehr als 50 bar erhöht. Dieser Vorgang erwies sich als überaus deterministisch. Die Anordnung stellt daher ein vielversprechendes Mittel zur Erzeugung der DDT für Anwendungen mit pulsierender Detonationsverbrennung dar.

Abstract

Pressure-gain combustion has been a topic of research interest for several decades. Due to the potential of pressure-gain thermodynamic cycles of increasing gas turbine efficiency by more than 10%, they offer a strategy to combat the growing problem of continually scarcer resources by simultaneous enforcement of ever stricter emissions controls. Furthermore, when hydrogen is used as a fuel, emissions of CO_2, a known greenhouse gas, are eliminated. Hydrogen can also be obtained using electrolysis powered by renewable energy sources. In times of less demand, excess energy can be used to produce hydrogen, which can then later be used for combustion-based energy generation when demand once again rises. Gas turbines offer an ideal platform for this technology, due to their fast response times when compared to other sources of combustion-based energy.

One type of pressure-gain combustion is known as pulse detonation combustion. Using this cyclical concept, the fuel is combusted by means of a detonation wave propagating at around 2000 m/s. Because of the speed of propagation, there is no time for the gas to expand during the combustion process and almost the entirety of the energy release is directed towards increases in pressure and temperature. This cycle is known as the Fickett–Jacobs cycle. Due to energy considerations, a flame is typically ignited by a low-energy ignition source and accelerated until it transitions to a detonation. This process is called the deflagration-to-detonation transition (DDT) and is the main focus of this work. Reducing the run-up distance to detonation has a direct impact on efficiency. Thus, it is worthwhile to achieve this transition over as short a distance as possible.

In this thesis, various methods of shortening the run-up distance to DDT using obstacles are investigated. Experiments to characterize the initial flame acceleration caused by a single obstacle concluded that the geometry of the obstacle plays only a minor role when compared to its blockage ratio. Furthermore, when multiple orifice plates are used, the optimal separation distance was found to be just over two tube diameters. Experiments on a separate test bench confirmed this finding also in regards to DDT and found that a tube diameter of around 40 mm is necessary to obtain reliable DDT over a reasonable run-up length using orifice plates.

The results of these initial studies aided in designing a modular pulse detonation combustion test bench. Using oxygen enrichment to simulate the operating conditions of a micro gas turbine, DDT was achieved using only 2-3 orifice plates when a wave-reflecting geometry was used at the inlet of the detonation chamber to support initial flame acceleration. Further investigations on a shock-focusing nozzle were successful in producing reliable DDT over a length of just 158 mm. Using this nozzle, a local explosion is initiated ahead of a fast accelerating turbulent flame by reflection and focusing of the leading shock. The result is a pressure increase in the region of focus in excess of 50 bar. The process is also found to be very deterministic. Therefore, this geometry presents a very promising means of producing DDT for pulse detonation combustion applications.

Contents

List of Figures

List of Tables

Nomenclature

Symbols

p	Pressure (bar)
v	Specific volume (m^2/kg)
ρ	Density (kg/m^2)
u	Velocity (m/s)
h	Enthalpy (J)
q	Heat addition (J)
X	Molar fraction (-)
h_f	Heat of formation (J/mol)
$\dot{m}$	Mass flow rate (varies)
γ	Adiabatic index (-)
λ	Detonation cell width (mm)
χ	Stability parameter (-)
Δ_I	Induction length (mm)
ε_I	Reduced activation energy (-)
$\dot{\sigma}_{\text{max}}$	Maximum thermicity (J/s)
$\bar{M}$	Molar mass (kg/mol)
c_p	Heat capacity (J/(mol·K)
Y	Mass fraction (-)
T	Temperature (K)
m	Mass (kg)
S	Surface area (m^2)
v_c	Propagation speed (m/s)
R_{spec}	Specific gas constant (J/(K·K))
$M_{0,r}$	Mach number, incident, reflecting (-)
W	Shock speed (m/s)
D	Diameter (m)
n	Refraction index (-)

ν	Dynamic viscosity (m^2/s)
η	Kinematic viscosity (Pa$cdot$s)
I	Turbulence intensity (-)
U_0	Bulk velocity (m/s)
f	Frequency (Hz)

Abbreviations

CJ	Chapman–Jouguet
CW	Constant wave
DDT	Deflagration-to-detonation transition
LED	Light-emitting diode
LST	Laser sheet tomography
PDC	Pulse detonation combustor
PID	Proportional-integral-derivative
PIV	Particle image velocimetry
RDC	Rotating detonation combustor
SWACER	Shock amplification through coherent energy release
VI	Virtual Instrument
VN	Von Neumann
ZND	Zel'dovich–von Neumann–Döring

1 Introduction

In this day and age, energy use and production is a topic of paramount importance. Not only is energy demand constantly increasing, but the realization that many sources of energy have serious environmental implications has ushered in the sustainable energy transition. This pivotal shift involves not only increasing the share of renewable energies being used for transportation as well as heat and electricty production, but also increasing the efficiencies of more conventional energy sources, for instance, those based on combustion. Many renewable energy sources are dependent on uncontrollable factors and, especially in the cases of solar and wind energy, exhibit very fluctuating characteristics. Short-term fluctuations within one week exhibited by a local renewable network in eastern Germany are plotted in Fig. 1.1. The significant fluctuations in both wind and solar power provided are clearly evident. The residual power (i.e., the power that still remains to be produced for the consumer) fluctuates also fairly strongly due to changes in demand throughout the day. The majority of conventional power plants (such as nuclear or coal-based facilities) are not capable of compensating for these fluctuations. This is due to the fact that they are typically designed for a distinct operational load at which the efficiency is at a maximum and start-up or reaction times are too large. Due to this, these power plants are only suitable for providing base load. Gas turbines, on the contrary, have the ability to quickly react to changing demands and are, therefore, used in so-called peaking power plants. Referring once again to Fig. 1.1, it can be seen that at certain time intervals, excess power is produced. This means that the power produced by the combined wind and solar sources exceeds the current demand. This excess energy can be used to produce hydrogen, taking advantage of power-to-gas concepts to provide energy at times when demand once again exceeds renewable supply. By moderately increasing the amount of renewable energy sources, it is conceivable that the region in question can be supplied with power derived 100% from renewable sources. This is only possible if combustion systems are utilized that use the hydrogen produced from these renewable sources.

1.1 Hydrogen and Power-to-Gas

As mentioned above, gas turbines will play a decisive role in the sustainable energy transition. However, the fact that this technology is mostly based on fossil fuels such as oil and natural gas means that exhaust gas emissions still present a challenge. For example, about 24% of carbon dioxide (CO_2) emissions in the United States are due to the use of natural gas and 31% of these are from electricity

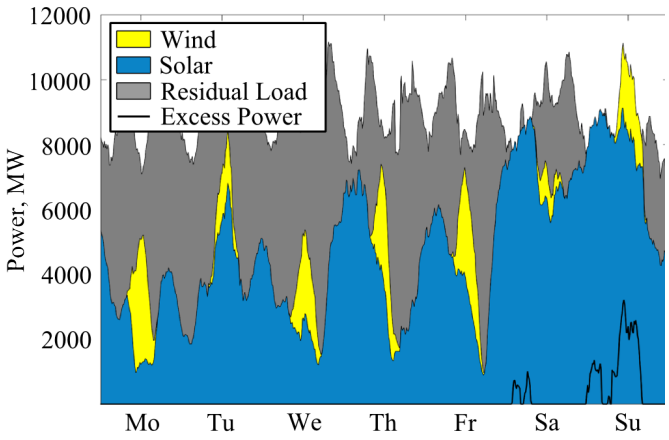

Figure 1.1: Energy production from renewable energy sources for an example week (10th–16th of February, 2014) in eastern Germany (Agora, 2014). Fluctuations illustrate the need for peaking power plants, such as those operated with gas turbines. An energy surplus shows the potential for power-to-gas technology, assuming a moderate, simultaneous increase in renewable energy sources.

production (CCES, 2017). Furthermore, carbon monoxide (CO), a highly toxic gas, is a by-product in the combustion of fossil-fuels. The use of hydrogen as a fuel eliminates both CO_2 and CO as combustion products.

Hydrogen may be produced by means of electrolysis[1], decomposing water into hydrogen and oxygen. This may seem couterintuitive, as this process requires energy; however, in combination with the fluctuating characteristics of typical renewables, it presents a viable option for energy storage. At times in which energy is in surplus, hydrogen may be produced and then burned when energy demand surpasses energy supply. This idea may be grouped under power-to-gas technologies. Currently, hydrogen produced with power-to-gas is used in one of three ways:

1. Hydrogen is injected directly into the natural gas grid. As hydrogen is much more reactive than natural gas, the amount may not exceed 15% by volume without increasing safety risks and requiring modifications of household appliances. At values above 20%, these risks may become severe (Melaina et al., 2013).

2. Hydrogen is added after the gasification process to increase the quality of biogas.

3. Hydrogen is combined with CO_2 to produce methane. This process is called methanation. As methane is the primary component in natural gas, it may also be directly injected into the natural gas grid, but without the disadvantages of direct hydrogen injection.

The consumption chain of the methanation variant is shown in Fig. 1.2a. This adds another method of complexity to the already complex energy network and carries with it another efficiency hit of 20%

[1]There are several other more prevalent methods, for example, steam reforming. Many of these processes, however, require fossil fuels themselves or produce a large amount of CO_2.

(Schaaf et al., 2014). However, if the hydrogen could be efficiently burned directly for energy production, as shown in Fig. 1.2b, a simpler and more efficient system could be realized.

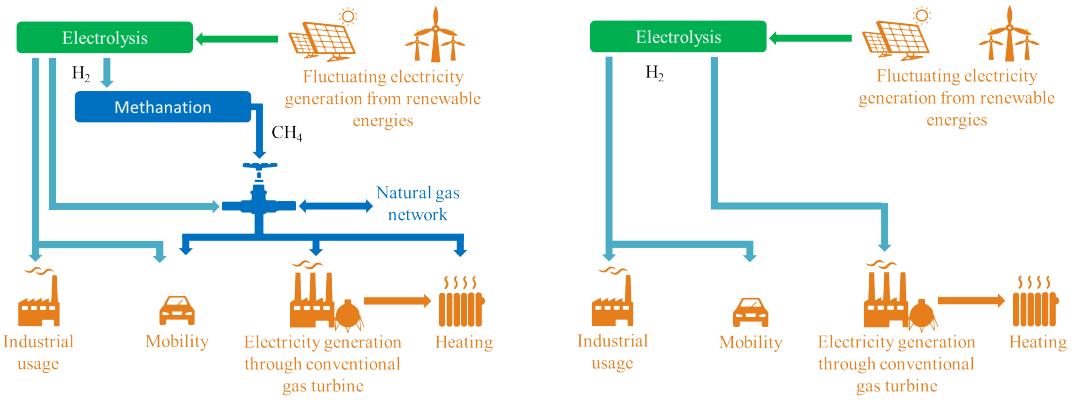

(a) Power-to-gas with methanation.

(b) Power-to-gas without methanation.

Figure 1.2: Consumption chain for power-to-gas concepts with and without methanation. Dispensing with methanation results in a less complex energy network and may result in higher total efficiencies, provided that suitable combustion technologies are developed for the direct use of hydrogen as a fuel.[2]

On the other hand, the direct use of pure hydrogen as fuel presents many challenges. For gas turbines, two problems prevent hydrogen from being used directly in machines that typically run on natural gas or liquid fuels. First, the turbulent flame speed for hydrogen flames is significantly higher than that for natural gas. This may result in flash back, a phenomenon which may seriously damage the gas turbine. Second, the adiabatic flame temperatures are much higher than those used in modern gas turbines. Even for lean mixtures, these temperatures are on the boundaries of modern material and cooling technologies. Furthermore, high temperatures exacerbate the problem of nitric oxide (NO) and nitrogen dioxide (NO_2) production, together known as NO_x. In the atmosphere, NO_2 can also react with moisture, resulting in more nitric acid. The process leads to a form of pollution known as acid rain. For this reason NO_x emissions have been stictly controlled since the 1970s. Another issue has less to do with the technical utilization of hydrogen in the machine, but more to do with the transport and storage of the hydrogen. The low density of this gas does not led itself well to being transported over large distances (i.e., through pipelines). This means that for the benefits of power-to-gas to be fully utilized, decentralized, smaller electrical generation plants should be built directly onsite near the renewable energy source.

1.2 Pressure-Gain Combustion

Conventional gas turbines are based on the Brayton cycle, which utilizes a constant-pressure heat addition combustion process, also known as a deflagration. Improvements in technology have led to higher

[2] Icons made by Freepik, www.flaticon.com

pressure ratios and turbine inlet temperatures, leading to even higher efficiencies. However, the limit to these technological improvements is beginning to become apparent. The improvement in simple cycle gas turbine efficiency over the past few decades is shown in Fig. 1.3. In spite of technological advancements, every point in efficiency is becoming more and more difficult to attain, leading to an ever flattening efficiency curve. Based on these data, Gülen (2016) argues that an increase in efficiency beyond 43% by the year 2035 is unrealistic. He also cites modern compressor and turbine efficiencies as both being around 90%. This leaves the combustion process, the process where the most entropy is produced, as being the main culprit for limiting efficiency gains.

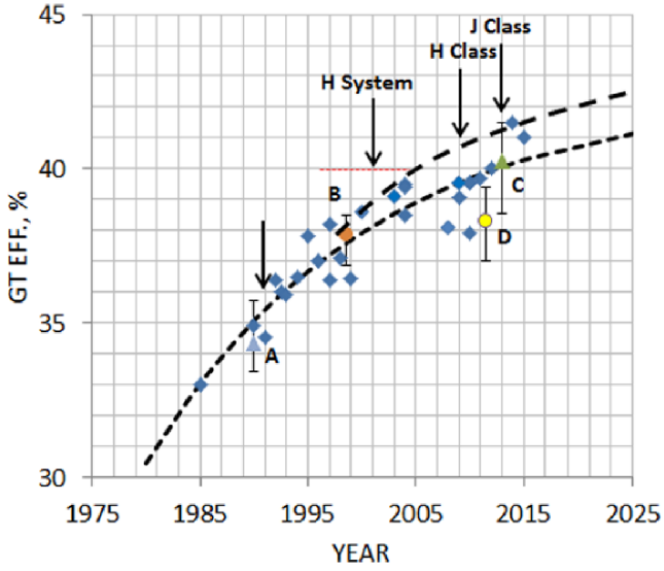

Figure 1.3: Trends in gas turbine efficiency over the last few decades. An ever flattening gain in efficiency can be attributed to technological boundaries. Gains beyond 43% by 2035 are unrealistic. Image taken from Gülen (2016). Original data are cited in this source.

One way of potentially breaking through this barrier is a paradigm shift in the way the combustion takes place in the first place and moving away from the typical isobaric heat addition process in favor of an isochoric, or constant-volume, process, the ideal cycle of which is known as the Humphrey cycle. As constant-volume combustion is associated with a pressure rise, this process is also referred to as a subset of pressure-gain combustion. There are several types of machines which are based on this cycle (e.g., pulse jets (Litke et al., 2005), wave rotors (Jones and Welch, 1996), etc.). Pulse jets, like the infamous German "V-1 Buzz Bomb" have been around for the better part of a century. Another type of combustion process has been around, at least in theory, for just as long. This detonation-based, pressure-gain concept is very similar to that of constant-volume and is known as a pulse detonation combustor (PDC). In 1940, Zel'dovich published the benefits of steady-state detonation waves for energy applications in Russia (Zel'dovich, 1940b). In the same year in Germany, Hoffmann published a propulsion concept based on pulsating detonative combustion (Hoffmann, 1940). In the 1950s research initial tests were successful in the United States (Nicholls et al., 1957), but until the 1980s, when a self-aspirating device was developed at the Naval Postgraduate School (Helman et al., 1986), research

activity was rather limited. Since then, the field has enjoyed times of much publication and times of low attention, due in part to the technical challenges associated with the PDC process, namely high temperatures, high pressures, short time scales required for mixing and injection, and the highly unstable environment at the tube exit, making the simple integration of a high efficiency turbine extremely difficult. In the last decade, a resurgence of research activity has occurred and several successful PDC programs are present to some degree around the globe. In fact, in 2008, the first PDC-based engine was operated for a short time in flight (Barr, 2008). For the sake of completeness, it should also be mentioned that another type of pressure-gain combustion has been the focus of much research in recent years. This promising concept also harnesses the benefits of detonative combustion and is known as a rotating detonation combustor (RDC). This is also an exciting new field and for a summary of RDCs, the reader is referred to Lu and Braun (2014); Stoddard et al. (2016). However, the focus of this work will remain on aspects of PDCs.

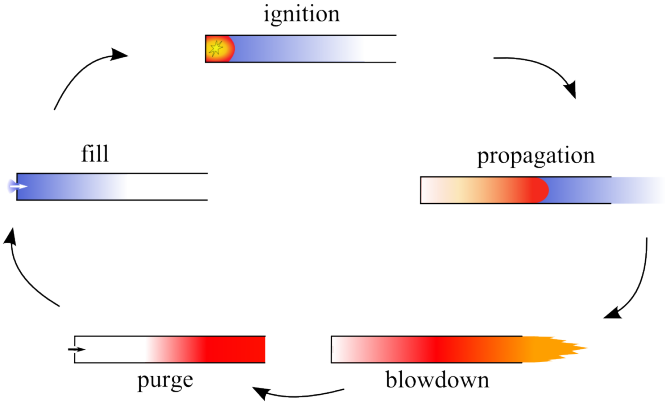

Figure 1.4: Cycle for pulse detonation combustion consisting of five phases: Fill, ignition, propagation and DDT, blowdown, and purge.

The pulse detonation combustion cycle can be broken down into five phases. First, the detonation chamber is filled with a fresh gas mixture. The mixture is then ignited, typically by means of spark. The reaction front then propagates through the chamber. Subsequently, the exhaust gases are expelled into the turbine. Finally, a non-reactive buffer is introduced in order to purge the tube of hot reactants and provide a certain degree of cooling. This cycle is summarized in Fig. 1.4. The cycle can also be depicted in terms of a pressure–specific volume diagram and a temperature–entropy diagram (see Fig. 1.5). In the p–v diagram, note the constant-pressure heat addition for the Brayton cycle. This is in stark contrast to the constant-volume heat addition for the Humphrey cycle. The Fickett–Jacobs cycle exhibits a near constant-volume cycle with a slight decrease in specific volume due to the detonation process. Considering the T–s diagram allows for the efficiency benefits of the Fickett–Jacobs cycle compared to the other two cycles to be readily seen. Kailasanath (2000) summarizes these efficiencies for a compressor pressure ratio of 3:1 for idealized cycles as 27% for the Brayton cycle, 47% for the Humphrey cycle, and 49% for the Fickett-Jacobs cycle. These efficiencies were substantiated by a thermodynamic analysis conducted by the author and colleagues at TU Berlin (Gray et al., 2016). To be fair, the efficiencies reported by Kailasanath are given in a domain where the PDC has a significant

advantage. As the compressor pressure ratio increases, the efficiency gain of over 20% diminishes, but still remains substantial (see Fig. 1.6). Gray et al. (2016) also determined that the non-steady effects of the PDC process had a detrimental effect on the efficiency of the turbo components of the gas turbine, negating some of the gains caused by the more efficient combustion mode. For further information in regards to research conducted in the field of pulse detonation combustion, the reader may refer to Roy et al. (2004) and Kailasanath (2009).

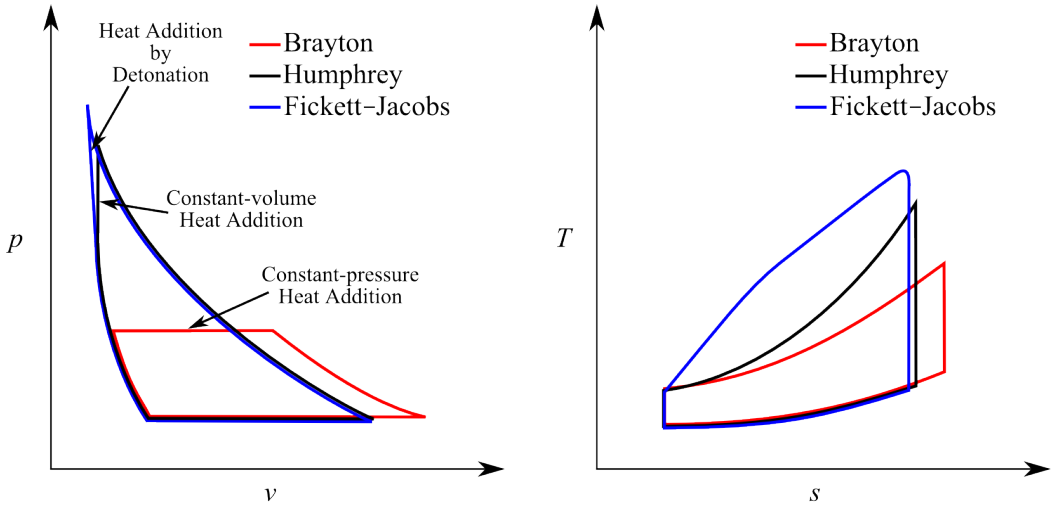

(a) Pressure–Specific volume diagram. Image adapted from Wintenberger and Shepherd (2006)

(b) Temperature–Entropy diagram. Image adapted from Heiser and Pratt (2002)

Figure 1.5: Thermodynamic diagrams depicting the Brayton, Humphrey and Fickett–Jacobs cycles. Note the different means of heat addition.

As a closing remark, the high reactivity of hydrogen makes it an ideal fuel for PDCs. A gas turbine utilizing a hydrogen-fueled PDC lends itself well to integration into the power-to-gas scheme discussed in the previous section. Flashback is no longer a problem in this particular mode of combustion. However, the higher temperatures will undoubtebly result in higher NO_x emissions if left unchecked. This is an issue that must be addressed for PDCs to be a viable alternative to conventional gas turbines.

1.3 Scope of this Thesis

The objective of this thesis is to present the work conducted during the foundation of the first pulse detonation combustion research program at the Chair of Fluid Dynamics at TU Berlin. As such, a good deal of initial investigations were required, because fundamental knowledge obtained from literature and that aquired from hands-on experience are not necessarily synonomous, but in fact, must complement each other. Technical aspects of experimental facilities are not always readily available in literature. Thus, this valuable knowledge was obtained *peu à peu*, so to say, and a decent amount of trial and error was involved in the development of this new research program. An attempt was made,

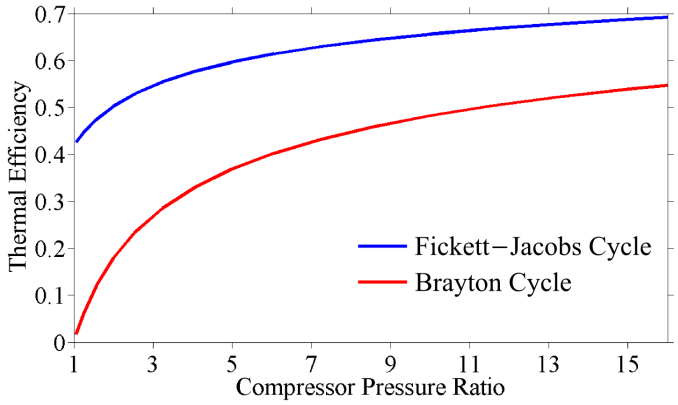

Figure 1.6: Theoretical efficiency of the Fickett-Jacobs cycles versus the Brayton cycle. Potential efficiency gains of over 20% can be realized at lower pressure ratios. As the pressure ratio increases, these gains are less significant, but still present.

however, to spare the reader from tedious and often misleading attempts that must be followed in such an endeavor. As such, the relevant work along the long path to this end is summarized in the pages to come.

The structure of the thesis is as follows:

Chapter 2 introduces the theoretical considerations necessary for a general understanding of the topics at hand. Some of the important work up to the end of the twentieth century dealing with the one-dimensional theory on shock and detonation waves is summarized. Subsequently, the theory put forward independently by Zel'dovich, von Neumann, and Döring in the 1940's identifying the structure of a detonation wave as a closely coupled shock wave and reaction zone separated by an induction zone is introduced. In fact, detonations exhibit a highly three-dimensional nature, as is also discussed along with the explanation of detonation cell width and its implications on reactivity and the deflagration to detonation transition (DDT). A model developed in recent years for estimating detonation cell width is then presented. An example relevant to this thesis is then provided applying this model. The initiation of detonations and the phenomenon of DDT is subsequently handled and various methods of producing it are discussed. The chapter is brought to a close with several pertinent examples involving flame propagation, shock wave reflection, and the focusing of a shock wave at a triangular-shaped endwall, the latter being important for the considerations presented in the remainder of this thesis.

Chapter 3 details the various experimental setups developed and utilized in the course of this work. The test bench on which investigations of the initial flame propagation and acceleration using one to three obstacles of various geometries is described. Here, laser sheet tomography (LST) was employed as the measurement technique. Subsequently, another test bench is presented in order to determine the influence of the number of and separation distance between multiple orifice plates on DDT. Experiments conducted in a water tunnel to characterize the flow field for various injection geometries are summarized. These experiments utilized particle image velocimetry (PIV) to evaluate the performance

of virtual obstacles for DDT enhancement. Afterwards, the design and development of the valveless modular pulse detonation test bench and the required associated infrastructure is summarized. A series of experiments designed to ascertain the effect of orifice plates on DDT in this configuration is described. Various geometries for the inlet to the detonation chamber are also presented. Finally, a novel concept involving an improved injection geometry and a method of shock focusing utilizing a converging–diverging nozzle is proposed for pulse detonation applications.

Chapter 4 presents the results of the initial investigations involving flame propagation and DDT on the two separate test benches. Also, the resulting flow fields obtained in the water test bench for the virtual obstacles are provided, with a note on the application of virtual obstacles in PDCs. These findings were applied to the development of the modular pulse detonation test bench. The results obtained while investigating orifice plates on this test stand as well as the influence of oxygen enrichment are then presented. Finally, the performance of the shock-focusing geometry is discussed. The findings are supported by evidence based on measurements with pressure transducers and ionization probes, high-speed imagery, and high-speed shadowgraphy. An attempt is then made to characterize the underlying processes responsible for reliable DDT. Finally, some comments on the multi-cycle operation of the modular PDC using both orifice plates and the shock-focusing nozzle are provided.

2 Theoretical Considerations

Sehen heißt verstehen
Seeing means understanding

Ernst Mach

This chapter deals with the fundamental theory behind detonation waves as well as other important aspects necessary for the comprehension of this thesis. As we have seen in Chapter 1 pulse detonation combustion, as a form of pressure-gain combustion, has the potential of significantly improving the gas turbine cycle, or rather, offering another cycle with a higher thermodynamic efficiency. But what is a detonation in and of itself?

2.1 The Discovery of the Detonation

In the early 1880s two French chemists at the Paris School of Mines, Ernest-François Mallard and Henri Louis Le Chatelier, both to become famous in their own time in their respective fields of chemistry, were motivated by a series of accidents involving explosions in mines to conduct experiments investigating the propagation of flames. Some of these experiments resulted in the rather spectacular "annihilation of the [measurement] apparatus" (Oppenheim and Soloukhin, 1973). Hearing of this, two scientists at the School of Pharmacy, P.E. Marcellin Bertherlot, the founder of organic chemistry, and Paul Vieille, began investigating this phenomenon. Oppenheim speculated the reason for their interest to be the vague belief at that time that explosions involved the "uncontrolled fission of organic molecules." Whatever their motivation, these two were successful at characterizing the process of detonations in gaseous mixtures, which had at this point only been observed in condensed explosives (Berthelot and Vieille, 1882). This new mode of propagation was in stark contrast to that of *flammes en naturelle*. Here, the propagation mode was obviously too fast to be explained by thermal conductivety and diffusion of exhaust species. In their more rigorous treatise of nearly 300 pages the following year, with a chapter dedicated to detonations, Mallard and Le Chatelier (1883) credit Berthelot and Vieille with the discovery of the detonation in gaseous mixtures. This phenomenon would be a topic of extreme interest for the next century.

2.2 Rankine–Hugoniot Jump Conditions

In order to actually describe the phenomenon of the detonation, a small step back must be taken. As with Navier and Stokes, establishing the fundamental equations of fluid motion, the rivalry between the English and the French schools of thought throughout the 18th and 19th century was very intense. As such, it was typical for British scholars to completely ignore the scientific work being done on the continent by their French counterparts and vice-versa (Salas, 2009). Due to this, common theories were very often developed and published twice independently. Such was the case between William Rankine and Pierre Hugoniot. At this time, the field of thermodynamics was in its infancy and the concept of entropy had not yet been developed. Furthermore, the prevailing belief that nature would not tolerate a discontinuity such as a that produced by a shock wave hampered the theoretical progress in the field.

Bernhard Riemann showed that due to the differing speeds of sound over an acoustic wave, a self-steepening effect would lead to a discontinuity, or a shock wave. Taking this into account, Rankine and Hugoniot showed that an isentropic shock would violate the energy equation. The resulting form of the energy equation would come to be known as the Hugoniot curve. This form of the energy equation describes the relationship between the states before and after a shock wave and will be discussed within the context of the next chapter. With this, the stage was set for another French–English pair to develop a theory to explain the curious observations of Berthelot and Vieille.

2.3 Chapman–Jouguet Theory

The following theory was independently developed by David Chapman and Émile Jouguet. To establish the equations for this theory, a steady-state reaction wave is considered with reactants approaching at state 0 from the right and products leaving the wave at state 1 to the left (see Fig. 2.1). The conservation equations can then be considered for this system:

Conservation of mass

$$\rho_0 u_0 = \rho_1 u_1, \tag{2.1}$$

Conservation of momentum

$$p_0 + \rho_0 u_0^2 = p_1 + \rho_1 u_1^2, \tag{2.2}$$

Conservation of energy

$$h_0 + q + \frac{u_0^2}{2} = h_1 + \frac{u_1^2}{2}. \tag{2.3}$$

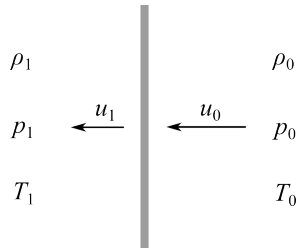

Figure 2.1: Sketch of a one-dimensional reaction wave based on Chapman–Jouguet theory in the wave-based frame of reference. The reaction is assumed to be a one-step process with immediate transition from initial to final state. Drawing adapted from Lee (2008).

Here, p is the pressure, u is the gas velocity, ρ is the density, h is the enthalpy, and q is the heat addition from the reaction.

The heat addition q is the difference between the molar-averaged enthalpies of formation h_f of the reactants and products:

$$q = \sum_{i}^{N_{\text{reactants}}} X_i h_{f,i} - \sum_{j}^{N_{\text{products}}} X_j h_{f,j}, \tag{2.4}$$

where χ is the mole fraction of the respective species in the reactants i and products j, and N is the total number of reactant or product species, respectively. Subsequently, Eq. 2.1 and Eq. 2.2 can be combined to obtain

$$\frac{p_1 - p_0}{v_0 - v_1} = \rho_0^2 u_0^2 = \rho_1^2 u_1^2 = \dot{m}^2, \tag{2.5}$$

in which the mass flux is $\dot{m} = \rho_0 u_0$ and $v = \frac{1}{\rho}$ is the specific volume of the corresponding state. Rearranging this equation results in

$$p_1 = p_0 + \dot{m}^2 v_0 - \dot{m}^2 v_1. \tag{2.6}$$

Assuming an initial state (v_0,p_0), it can be seen that Eq. 2.6 is simply a line, the slope of which is proportional to the square of the mass flux $\dot{m}$. This is known as the Rayleigh line and all possible states (v_1,p_1) lie along this line. Using Eq. 2.5, the velocities in Eq 2.3 can now be eliminated, resulting in the familiar form of the Hugoniot curve:

$$h_1 - (h_0 + q) = \frac{1}{2}(p_1 - p_0)(v_0 - v_1). \tag{2.7}$$

The Hugoniot curve is a rectangular hyperbola, the asymptotes of which correspond to

$$v = \frac{\gamma - 1}{\gamma + 1} \text{ as } p \to \infty$$

and

$$p = -\frac{\gamma - 1}{\gamma + 1} \text{ as } v \to \infty,$$

where γ is the adiabatic index.

Equations 2.6 and 2.7 can be represented in a pressure–volume diagram (see Fig. 2.2) and the solutions to the system correspond to possible states (p_1, v_1), which exist at the intersection of a Rayleigh line and the Hugoniot curve. A slightly different derivation is given in Lee (2008), however, this path includes the modern-day notion of the Mach number, a tool which Chapman and Jouguet may or may not have had at their disposal (Ernst Mach was a contemporary). Although it may have its merits, the additionally needed considerations were deemed unnecessary to furnish the basic ideas required for the understanding of this theory.

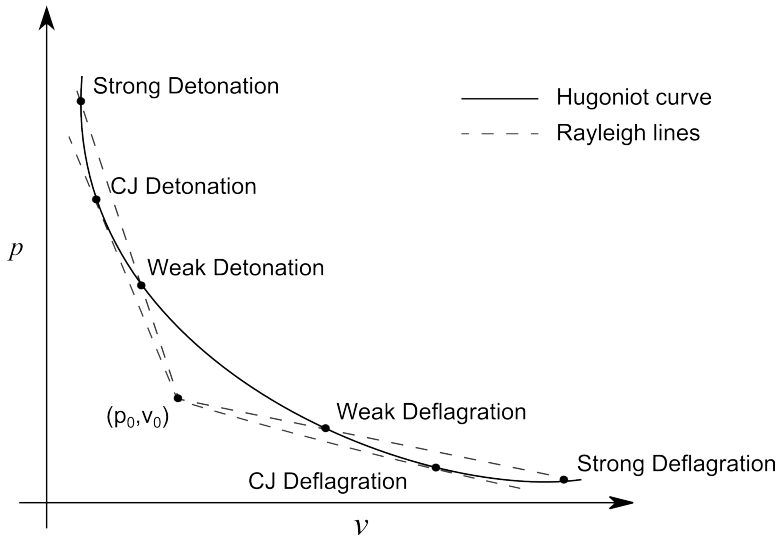

Figure 2.2: Rayleigh lines and Hugoniot curve derived from CJ theory. The solutions correspond to weak and strong deflagrations and detonations, respectively. The tangency solutions correpond to the CJ deflagration and CJ detonation. Drawing adapted from Lee (2008).

Depending on the slope of the Rayleigh line, which represents the mass flux through the reaction wave (or simply the velocity of said wave), either one or two solutions are possible. Low slopes correspond to larger increases in specific volume and smaller decreases in pressure (deflagrations). The first solution is known as a weak deflagration, behind which u_1 is subsonic with respect to the products. For a strong deflagration, u_1 is supersonic. Following the Rayleigh line from the initial state, we first intersect the reacting Hugoniot curve at the weak deflagration solution. A transition along this line to the strong deflagration solution requires a rarefraction shock, which is physically impossible. Due to this, only weak deflagration solutions exist in reality. Let it also be mentioned that deflagrations are highly dependent on the propagation mechanism. The flame propagation speed is dependent on many factors (turbulence, boundary conditions, etc.). This speed, in turn, alters the initial point (p_0, v_0) by means of a decoupled leading shock in many cases, altering the reaction Hugoniot by preconditioning of the reactants. Furthermore, the propagation of a deflagration is dominated by diffusive processes.

These are not considered in this approach, although they are the primary factors effecting the speed of propagation. Thus, Chapman–Jouguet (CJ) theory is inadequate at describing the true processes occurring in a deflagration.

The detonation branch in CJ theory is somewhat more straightforward. Here, there is also a weak solution and a strong solution. For a weak detonation, the velocity u_1 of the products is supersonic, whereas for a strong detonation, this velocity is subsonic. The fact that the products behind a strong detonation are subsonic, results in the attenuation of this wave from expansion effects propagating upstream. Thus, strong or overdriven detonations are normally not steady-state and usually short lived. The weak detonation requires very special conditions of the Hugoniot curve, which were only obtained by von Neumann half a century after Chapman and Jouguet. In general, however, because these conditions are rare, this solution can usually also be ruled out.

At this point, Chapman and Jouguet formulated two explanations for what would be known as the CJ velocity, or the experimentally observed steady-state propagation velocity of a detonation. Chapman (1899) stated that as only one propagation velocity is observed, it must be that for which the Rayleigh line is tangent to the Hugoniot curve. This is known simply as the tangency condition or the minimum velocity solution. Jouguet (1905) analyzed the entropy variation along the reactive Hugoniot curve. He determined that the point of minimum entropy correponds to the sonic condition, in which the exhaust gases exhibit a velocity away from the detonation wave at the speed of sound in the products, also known as the CJ particle velocity. With this information, he postulated that the point of minimum entropy is the solution for the steady-state detonation. His colleague Crussard proved shortly afterwards that Chapman's solution and Jouguet's solution are indeed equivalent (Crussard, 1907).

To give credit where it is due, the Russian physicist Michelson actually conducted a similar thermodynamic analysis. However, as his work was little known outside of Russia and his international publications were limited to German (Michelson, 1889), the theory described in this chapter came to be known as Chapman–Jouguet (CJ) theory. The Rayleigh line, however, is sometimes also referred to as the Michelson line.

In an effort to provide a more concrete theoretical foundation to the instantaneous transformation of reactants to products described by the CJ criterion, many scientists delved into the task of discerning the real structure of a detonation wave. Among these was Richard Becker, who focused on the entropy considerations developed by Crussard (Becker, 1917, 1936). He attempted to describe a shock wave across which chemical reactions take place. Due to the close coupling of the shock wave and the reaction zone, he postulated (incorrectly) that heat conduction and viscosity would play a decisive role in the course of the reactions. Even this mistake would bring the course of detonation research even further and it would be Becker's student (and two others) who would determine that the real structure is much more complex.

2.4 ZND Theory

Due to the race towards "the bomb," shock wave physics was given much scientific attention during and after the Second World War. Independently around the globe, research was conducted on detonations and blast waves leading to the development of a more detailed detonation theory (Krehl, 2009). Yakov Zel'dovich (Zel'dovich, 1940a), of the Soviet Union, John von Neumann (von Neumann, 1942), a Hungarian-American in the United States, and Werner Döring (Döring, 1943) of Germany independently developed the theory later to be known as the Zel'dovich–von Neumann–Döring (ZND) theory within a few years of each other. The basic premise of the theory is maintaining a discontinuous jump criterion for the shock, but applying finite-rate chemical reactions in the post-shock domain, essentially separating the shock and the reaction front. The reactants are compressed along the shock Hugoniot curve, which describes the relation between the pressure and specific volume in the case of zero heat release. As the speed of the shock is already determined by the Rayleigh line, the point to which the compression takes place is also determined. This state is known as the von Neuman state. After compression the reaction progresses along the same Rayleigh line in the opposite direction to the CJ state. This process is illustrated in Fig. 2.3.

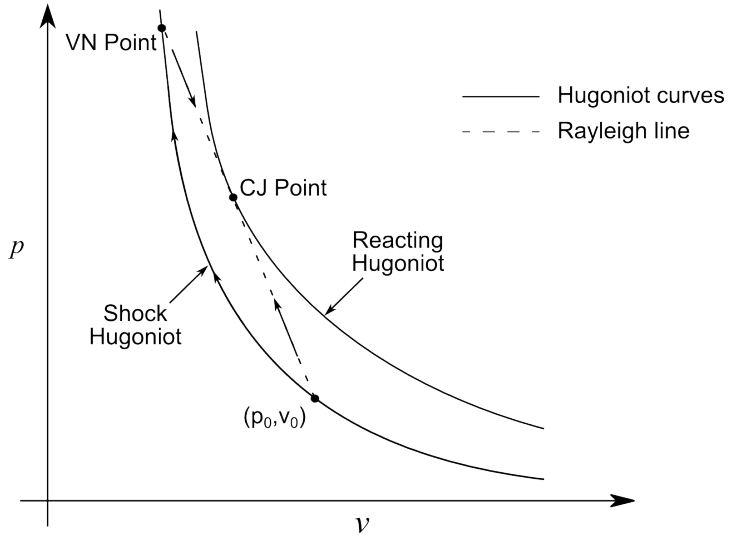

Figure 2.3: Illustration in the difference between CJ theory and ZND theory with respect to the process path. In CJ theory, the process follows the Rayleigh line directly to the CJ point without intermediate transitions. For ZND theory, the process first follows the shock Hugoniot curve to the von Neumann point and then approaches the CJ state along the same Rayleigh curve from the other direction.

The ZND structure itself is illustrated in Fig. 2.4a and more detailed in Fig. 2.4b. The gas is initially compressed by the shock wave, increasing the pressure and temperature to the von Neumann (post-shock) state. After a certain ignition delay time, dependent on the initial temperature, pressure, and gaseous mixture, combustion occurs. This is sometimes also called the induction time because the ignition delay time multiplied by the velocity of the fluid after the shock yields the induction length, or the distance between the shock wave and the beginning of the reaction zone. At the completion of

the combustion process, the products reach the Chapman–Jouguet state (see Sec. 2.3). In the case of a detonation propagating in a tube (as in a PDC), a zero-velocity boundary condition is imposed at the closed end. This state propagates from the closed end into the combustion products at the local speed of sound, resulting in a further expansion of the gases behind the detonation wave until the gases have achieved zero velocity. This state is known as the Taylor state. As the speed of sound in the products is lower than the CJ velocity, the length of the Taylor wave (the distance between the CJ point and the Taylor point) increases with time. At this point a theory has been described that portrays a one-dimensional detonation wave in a fairly detailed manner. However, in the overwhelming majority of events, real world physics does not limit itself merely to one dimension.

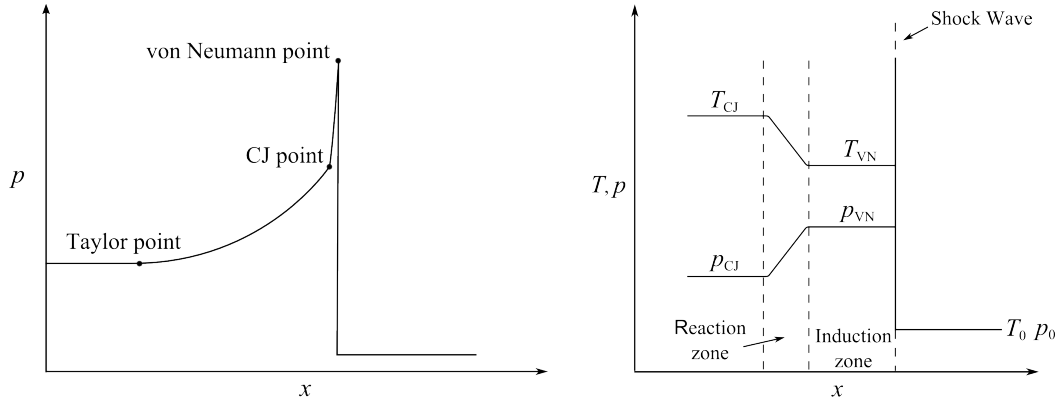

(a) Wave structure of ZND detonation.

(b) Detail of wave structure.

Figure 2.4: Illustration of the evolution of pressure and temperature along a ZND detonation. The shock initially induces a pressure and temperature increase to von Neumann conditions. After an induction zone, chemical reactions take place and are completed as the CJ state is reached. The CJ state is then followed by the Taylor wave, induced by the no-slip boundary condition at the ignition end of the tube. At the Taylor point, the gases have once again reached zero velocity through expansion processes. Drawings adapted from Lee (2008).

2.5 Multidimensionality of Detonations

Up until this point, we have considered detonations to be a one-dimensional phenomenon with varying degrees of complexity. The reality of the matter is that detonations exhibit highly complex, three-dimensional structures. These structures were first independently observed by Denisov and Troshin (1959) and White (1961). The detonation front is a very unstable boundary and any small disturbances, for example, inhomogeneities in the gaseous mixture, may create transverse instabilities which propagate at the speed of sound along the length of the front. These instabilities then coalesce into transverse waves. After a short time, a pronouced cellular structure develops (see Fig. 2.5). This cellular structure is due to the interaction between incident shocks, Mach stems, and transverse shocks. The point at which these three waves meet is known as the triple point. Detonation cells are formed by the trajectories of these triple points. At regular intervals along the front, two transverse shocks traveling in opposite directions meet. The resulting increase in pressure generates a local explosion at the apex of the cell, resulting in a new Mach stem, which essentially manifests as a short-lived, highly overdriven detonation traveling as much as 1.6 times the CJ velocity. This is the same as the strong detonation mentioned in Sec. 2.3. As such, it also exhibits a shorter induction length due to the higher pressure, as seen in Fig. 2.5. However, due to the subsonic flow behind the strong detonation, expansion waves reach the reaction zone and attenuate the detonation along this overdriven part of the front and the detonation decays quickly to a velocity as low as 0.6 times the CJ velocity, before being reinitiated by the subsequent collision of another two transverse waves. These variations in propagation velocity along one detonation cell were reported in Strehlow and Crooker (1974). Astonishingly, the average propagation velocity of the three-dimensional detonation is very close to the CJ velocity obtained from simple thermodynamics arguments.

The size of a detonation cell is dependent on several factors, including pressure, temperature, and the gaseous mixture itself. Generally, it is closely tied to the reactivity of the gas in question, due to the induction time, and is used as a reference of the sensitivity of the gaseous mixture to detonation (Lee, 1984). As the reactivity increases, the induction time and cell size decrease. At this point, a clarification must be made, as reference to cell size in literature frequently refers to cell size as one of two quantities: the cell length and the cell width. They are indeed related: $\lambda_w \approxeq 0.6\lambda_L$ (Lee, 1984), but simply referring to cell size is ambiguous. For this reason, the cell width will be preferred in the remainder of this work when referring to an actual quantity and will be denoted simply as λ, while cell size is reserved for general comparitive statements. Nevertheless, one last mention of cell length will be made, as Fig. 2.6 illustrates the variation of this quantity very clearly for various gas compositions.

Cell width is used as a quantity for characterizing several aspects of detonations. For instance, the critical tube diameter has been experimentally determined to be $d_{\text{crit}} \approx 13\lambda$. The critical tube diameter is defined as the diameter of the smallest tube from which a planar detonation may emerge and transition to a spherical detonation. At values below around 13 times the cell width, the shock wave decouples from the reaction zone and a spherical deflagration results (Lee, 1984). The cell width is also important for characterizing a self-sustaining detonation in a confined geometry. Lee (1984) also determined that a detonation is only able to propagate in tubes in which the circumference is at least one cell width. A

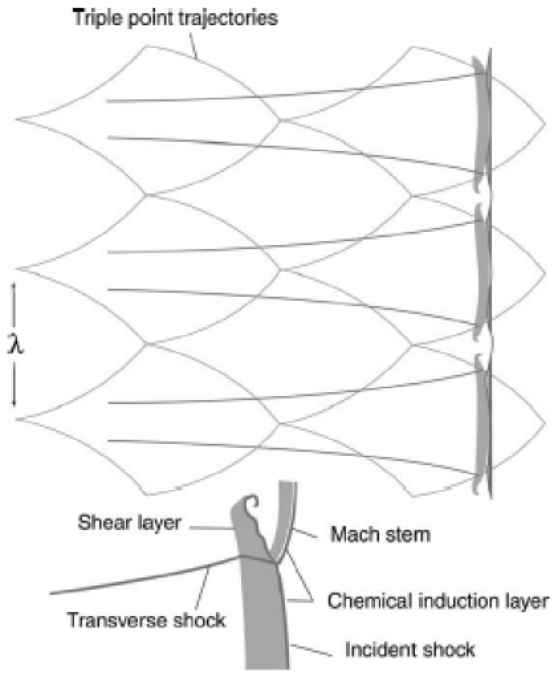

Figure 2.5: The cellular structure of a detonation wave traveling from left to right. The detonation cell is traced out by the triple points composed of the incident shock, transverse shock and Mach stem. Detonation cell width is identified by λ. Image take from Lee (2008).

detonation in such a tube is known as a spinning detonation, discovered by Campbell and Woodhead (1926), and travels along the axis of the tube at significantly lower velocities than CJ velocity. However, these marginal detonations are actually overdriven detonations traveling faster than CJ velocity at an oblique angle to the axis. As the circumference of the tube increases, the propagation velocity along the axis also increases until a CJ detonation is observed.

2.5.1 Detonation Cell Width Estimation

Cell width is not proportional to induction length as postulated by Shchelkin and Troshin (1965). The reason for this is due, once again, to the three-dimensional aspect of a detonation, over which the induction times vary significantly based on where the particular sub-volume of gas is located with respect to the complex shock system. Therefore, although a single induction time for a single gas mixture at a specific temperature and pressure is a good indicator of the general reactivity of the mixture, it does not present the entire picture.

Typically, detonation cell widths for particular mixtures have been determined experimentally. This is done either by using smoke foils or schlieren techniques (Strehlow and Crooker, 1974). It is, however, useful to have the capability of calculating the cell width for an arbitrary mixture at arbitrary conditions (pressure and temperature). Ng et al. have developed a half-empirical model (Ng et al., 2005, 2007)

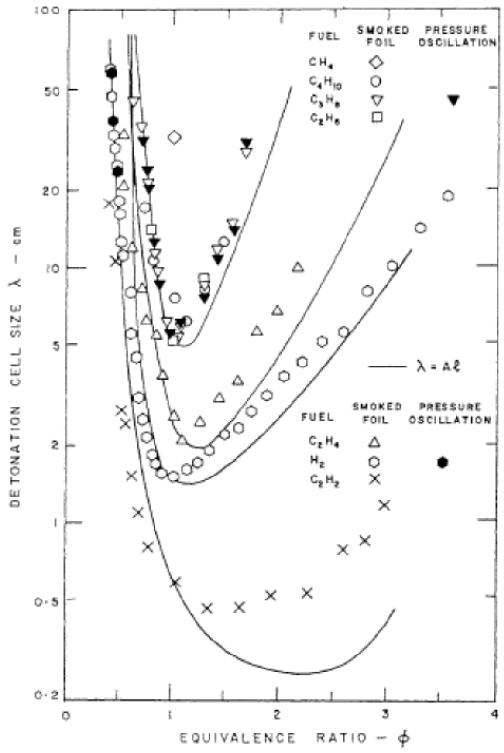

Figure 2.6: Experimentally determined cell size for various hydrocarbon–air mixtures. Image is taken from Knystautas et al. (1985). The cell size referred to here is, in fact, the cell length. A correlation to induction length is also provided, indicating that the two are closely coupled, but not proportional.

for calculating the cell width based on the induction zone length Δ_I and a so-called stability parameter χ:

$$\lambda = f(\chi)\Delta_I. \tag{2.8}$$

The stability parameter is defined as

$$\chi = \varepsilon_I \Delta_I \frac{\dot{\sigma}_{\max}}{u'_{\mathrm{CJ}}}, \tag{2.9}$$

where ε_I is the reduced activation energy, $\dot{\sigma}_{\max}$ is the maximum thermicity, and u'_{CJ} is the CJ particle velocity (velocity of the gas behind the detonation with respect to the reaction front). Ng et al. defined the function of χ to be

$$f(\chi) = A_0 + \frac{a_N}{\chi_N} + \ldots + \frac{a_1}{\chi} + b_1\chi + \ldots + b_N\chi^N \tag{2.10}$$

and determined the coefficients for calculating the detonation cell width to the third order (see Tab. 2.1).

Table 2.1: Empirically determined coefficients for cell width prediction (Ng et al., 2007).

Coefficients	Values
A_0	30.465860763763
a_1	89.55438805808153
a_2	-130.792822369483
a_3	42.02450507117405
b_1	-0.02929128383850
b_2	$1.026325073064710 \cdot 10^{-5}$
b_3	$-1.031921244571857 \cdot 10^{-9}$

2.5.2 Theoretical calculation of cell widths

In this section, the model of Ng et al. (2007) will be applied for various mixtures in order to describe how it was used within the framework of this dissertation and to explain the use of certain mixtures in the experimental investigations contained in this work. As this is an implementation of an existing model, it is included in this chapter rather than in those encompassing the original work contained in this thesis, although the implementation may vary slightly from Ng et al. (2007) in terms of how the required parameters for the model were obtained.[1] In order to describe the model, one additional quantity must be defined, namely, that of stoichiometry.

2.5.2.1 Stoichiometry

Although stoichiometry plays a secondary role in this work, as all mixtures considered were in fact stoichiometric, it is important to define this fundamental quantity before proceeding to the next section. Hydrogen is used as fuel for the entirety of this work, so the stoichiometric hydrogen–air reaction will be used:

$$2\mathrm{H_2} + \mathrm{O_2} + \frac{79}{21}\mathrm{N_2} \rightarrow 2\mathrm{H_2O}\ . \tag{2.11}$$

This results in a molar ratio of 4.76 moles of air ($\frac{79}{21}\mathrm{N_2} + 1\mathrm{O_2}$) to 2 moles of $\mathrm{H_2}$, or a ratio of 2.38:1. In this case, the oxygen in the air reacts completely with the hydrogen producing steam and leaving only the nitrogen in the air unreacted. A reaction in this proportion is known as stoichiometric. If more oxidizer is present in the reactants than may be consumed by the reaction, the mixture is said to be lean. If more fuel ($\mathrm{H_2}$) is present, the mixture is said to be rich. Due to Avogadro's law, the molar ratio may be directly interpreted as the volume ratio. Multiplication with the density ratio of hydrogen to air at atmospheric conditions results in the mass ratio (34.2:1). This ratio may be used to verify the mass flow rates of the experiments presented in Chap. 3. Another way of expressing the composition of a reactive mixture is the actual fuel to oxidizer ratio divided by the stoichiometric fuel to oxidizer ratio. This is known as the equivalence ratio:

[1] The implementation of the model was carried out by Niclas Hanraths within the course of his master's studies.

$$\phi = \frac{X_\mathrm{f}/X_\mathrm{ox}}{(X_\mathrm{f}/X_\mathrm{ox})_\mathrm{st}}, \tag{2.12}$$

where $\frac{X_\mathrm{f}}{X_\mathrm{ox}}$ represents the molar ratio of fuel to oxidizer of the actual mixture and $(\frac{X_\mathrm{f}}{X_\mathrm{ox}})_\mathrm{st}$, that of a stoichiometric mixture. Consequently, $\phi < 1$ corresponds to lean mixtures and $\phi > 1$, to rich mixtures.

2.5.2.2 Implementation of the model

As described in Sec. 2.5.1, four quantities are required in order to estimate the detonation cell width: ε_I, Δ_I, $\dot{\sigma}_\mathrm{max}$, and u'_CJ. However, obtaining these quantities requires determining several others along the way. Operations involving the calculation of chemical kinetics are conducted using Cantera (Goodwin et al., 2016) with the Burke chemical kinetics mechanism (Burke et al., 2012), a mechanism tuned to hydrogen–oxygen combustion at high pressures. The first step is to calculate the CJ velocity. However, the specific heat capacities c_p and c_v are not known, as they are temperature dependent. Furthermore, γ is not simply the ratio of the specific heats $\frac{c_p}{c_v}$ in this case and must also be determined. Details to these difficulties are presented in Gordon and McBride (1996). As a result, the CJ state must be obtained iteratively. The desired solution is the point of tangency of the Rayleigh line with the reacting Hugoniot curve, as described in Sec. 2.3.

The iteration scheme is based on an algorithm described by Zeleznik (1962)[2]. An initial estimate of p_CJ and T_CJ is made based on the initial pressure, temperature, and gas composition. For each iteration, successively more accurate values for the CJ state, adiabatic index, and heat capacity are obtained until the convergence criteria suggested by Gordon and McBride (1996) is achieved. After convergence, the following quantities are known: p_CJ, T_CJ, γ, the CJ particle velocity u'_CJ, the isobaric heat capacity, and the CJ velocity.

Once the CJ velocity is known, the post-shock (von Neumann) state can be determined by once again iterating to find the solution for the shock (non-reacting) Hugoniot curve and the Rayleigh line corresponding to the CJ velocity. The von Neumann state (p_VN, ρ_VN, and T_VN) is then used to calculate the induction time using a zero-dimensional constant-volume reactor in which the thermicity is also simultaneously calculated. The thermicity is a measure of the rate of transformation from chemical energy to thermal and mechanical energy, including not only heat release, but also effects due to a change in the number of moles. Kao and Shepherd (2008) define the thermicity as

$$\dot{\sigma} = \sum_i^N \left(\frac{\bar{M}}{M_i} - \frac{h_i}{c_p T} \right) \frac{\mathrm{D}Y_i}{\mathrm{D}t}, \tag{2.13}$$

[2]The source code for the iteration scheme is taken from NASA's Chemical Equilibrium with Applications (CEA) Software (Gordon and McBride, 1996) and uses first a rough iteration and then the Newton–Raphson iteration proposed by Zeleznik (1962).

where $\bar{M}$ is the mean molecular weight of the mixture, M_i is the molecular weight of the species i, h_i is its enthalpy, c_p and T the specific heat and temperature of the mixture, and $\frac{\mathrm{D}Y_i}{\mathrm{D}t}$, the convective time derivative of the species mass fractions. The maximum in the thermicity is then obtained and the induction time is chosen as the time between the start of the simulation and the time at which the highest temperature gradient is reached. The induction zone length Δ_I is then determined simply by multiplying the induction time with the CJ particle velocity.

Now, it only remains to determine the reduced activation energy, which is a measure of the sensitivity of the reaction zone to thermodynamic perturbations. These perturbations are achieved by varying the shock velocity by $\pm 1\%$ with respect to the CJ velocity, as proposed by Schultz and Shepherd (2000). The new post-shock states and the corresponding induction times are once again calculated and used to determine the reduced activation energy, also known as the effective activation energy parameter

$$\varepsilon_I = \frac{E_I}{RT_{VN}} = \frac{1}{T_{\mathrm{VN}}} \left(\frac{\ln\tau_+ - \ln\tau_-}{\frac{1}{T_+} - \frac{1}{T_-}} \right), \tag{2.14}$$

where τ_+ and τ_- are the induction times and T_+ and T_- are the von Neumann temperatures for the two perturbed states, respectively. Finally, the stability parameter is calculated from Eq. 2.9 and the cell width is obtained using Eq. 2.10 and Eq. 2.8. The model was validated using experimentally determined cell widths from the detonation database at the California Institute of Technology (Kaneshige and Shepherd, 1997) for stoichiometric hydrogen–oxygen mixtures at various pressures and 293 K and for hydrogen–air mixtures at 300 K and 1 bar for varying equivalence ratios (e.g., Ciccarelli et al. (1995)). Cell widths determined using this model are presented in Table 2.2 for stoichiometric oxygen–nitrogen–hydrogen mixtures at varying pressures and temperatures. The temperatures correspond to those resulting from isentropic compression of air at 293 K and 1 atm to the corresponding pressure:

$$\frac{T_2}{293\,\mathrm{K}} = \left(\frac{p_2}{1.013\,\mathrm{bar}} \right)^{\left(1-\frac{1}{1.4}\right)}. \tag{2.15}$$

At atmospheric conditions, oxygen enrichment to 40%-vol. results in the same cell width as for a stoichmetric hydrogen–air mixture isentropically compressed to 3 bar.

2.6 Detonation Initiation

Detonations may be initiated in a number of ways. The most straightforward is the direct initiation by introducing a large amount of energy in a short enough timespan that a blast wave results. This may be done, for example, by means of a spark (Knystautas and Lee, 1976; Lee and Matsui, 1977) or an explosion (Borisov, 1999). The use of an explosive, however, does not lend itself well to gas turbine applications. Furthermore, direct initiation by means of a spark requires large and expensive high-voltage equipment and large amounts of energy. Also, the electrodes are subject to extremely high levels of

O_2 in oxidizer, %-vol.	p, bar	T, K	λ, mm
21%	1.013	293	7.2
21%	2	357	4.1
21%	**3**	**401**	**2.9**
21%	4	435	2.35
30%	1.013	293	4.0
30%	2	357	2.3
30%	3	401	1.6
30%	4	435	1.3
40%	**1.013**	**293**	**2.9**
40%	2	357	1.6
40%	3	401	1.1
40%	4	435	0.9
50%	1.013	293	2.2
50%	2	357	1.3
50%	3	401	0.9
50%	4	435	0.7

Table 2.2: Estimated detonation cell widths obtained using the empircal model of Ng et al. (2007). Temperatures correspond to those reached due to isentropic compression to the given pressure. At atmospheric conditions, oxygen enrichment to 40%-vol. results in the same cell width as for a stoichmetric hydrogen–air mixture isentropically compressed to 3 bar.

wear (Panicker, 2008). Borisov (1999) determined that the minimum ignition energy for the direct initiation of a detonation using an explosion in a hydrogen–air mixture at atmospheric conditions is nearly 10 kJ. No data was found in literature for the direct detonation initiation of hydrogen–air mixtures using sparks; however, Litchfield et al. (1963) determined that detonation initiation in hydrogen–oxygen mixtures at atmospheric conditions by spark discharge required six to seven times more energy than the initiation of the same mixtures using an exploding wire.

Other means of detonation initiation involve the so-called deflagration-to-detonation transition (DDT). In such cases, a deflagration is initiated by a weak ignition source and a transition to detonation is achieved by various means. This has the advantage that the ignition process requires significantly less energy. Ono et al. (2007) achieved spark ignition of a stoichiometric hydrogen–air mixture at atmospheric conditions using less than 0.1 mJ, resulting in a flame. This is a difference eight orders of magnitude.

The first step of initiating DDT is to accelerate the flame resulting from the low-energy ignition. This is done most easily by the introduction of turbulence and typically achieved by introducing obstacles of various geometries, resulting in larger-scale flame folding as well as smaller-scale turbulent structures, which increase the turbulent flame speed. However, the contribution of turbulence to flame acceleration is typically limited to 10–20 times the laminar burning velocity. Beyond this point, additional turbulence begins to lead to quenching effects (Bray, 1990; Shy et al., 2000). At this point, the second phase begins and another mechanism for flame acceleration begins to take effect. When a flame propagates from the closed end of a tube, pressure waves are sent downstream ahead of the flame with a strength corresponding to the velocity of the flame. As the flame increases in velocity, these pressure waves eventually coalesce into a shock wave. This is known as a leading shock and may be likened to a piston moving at the speed of the flame as soon as the flame approaches the speed of sound of the reactants, at which point the shock wave no longer travels significantly faster than the flame. Furthermore, once this point is reached, the flame accelerates purely due to the existence of this shock. Shchelkin and Troshin (1965) present a very enlightening proof as to the origins of this phenomenon, in which the reader is referred to pages 165–174 for further reading. Suffice it to say that if an initial shock wave of strength Δp is present ahead of a flame, it creates an increase in flame propagation velocity Δv_f due to the higher temperature associated with the shock compression in the gas ahead of the flame. This velocity increase, in turn, results in an even further pressure increase $\Delta p'$, resulting in an ever accelerating flame front. Keeping this fact in mind, we will continue with our discussion of DDT. The third and final phase of this process is the transition itself. This may occur due to several different mechanisms, which will be discussed in the following.

Antoni Kazimierz Oppenheim was a pioneer in investigating the origins of DDT. In 1962, Oppenheim postulated the origin of detonation to be located in the so-called “explosion in the explosion” (Oppenheim et al., 1962). This is opposed to the deflagration accelerating and merging with the leading shock. According to the authors, pockets of gas are left behind due to the high turbulence in the deflagration front. This occurs frequently along the wall. These pockets are then “consumed by a deflagrative implosion, which can create locally an arbitrarily high pressure.” This pressure is then sufficient to create

an explosion triggering a detonation wave. Taking advantage of technological advances of the time (laser-based stroboscopic schlieren photography and soot-foils[3]), Urtiew and Oppenheim (1966) were able to prove Oppenheim's postulate. However, the authors added that this process is not the only way that DDT may occur and, in fact, it is highly stochastic and "may depend in turn on some minute local inhomogeneities in its development."

A seemingly competing mechanism was proposed by Zel'dovich et al. (1970) involving a gradient in ignition delay time in a non-uniform mixture. Non-uniform does not necessarily refer to composition but more often temperature gradients, which can even occur in gases of uniform composition. If autoignition occurs in a shock compressed medium at the position within the volume with the shortest ignition delay time, one of three scenarios will transpire. If the temperature gradient is very small, combustion will occur almost immediately in the rest of the volume, "propagating" in the direction of higher ignition delay times. This results in the near-simultaneous combustion of the mixture, which emulates constant-volume conditions. If the gradient is very large, a shock will form and rapidly travel away from the reaction front, resulting in a deflagration. At an intermediate gradient, a faster moving reaction zone couples with the resulting shock, transitioning to a self-sustaining detonation wave.

Finally, a compromising theory was postulated by Lee et al. (1978), in which microexplosions along the line of those envisioned by Oppenheim are amplified by Zel'dovich's temperature gradient mechanism. This hybrid mechanism is known as SWACER (shock wave amplification through coherent energy release) and is proposed by some to be universal, being the main contributor to DDT. Even DDT due to shock–obstacle interaction may originate to some degree from SWACER. Although this mechanism has been investigated now for over thirty years and many calculations have been conducted, "few of these can be directly and convincingly linked to a particular experimental result" (Ciccarelli and Dorofeev (2008), pg. 539). Whether or not the SWACER mechanism plays a role in shock–obstacle interaction and the ensuing DDT is for the purposes of this work irrelevant; and at this point, we will diverge from this more fundamental topic and return to the more practical consideration of producing DDT with obstacles.

Yakov Zel'dovich and Kirill Shchelkin conducted many experiments dealing with detonation and the initiation of detonation in rough tubes (Zel'dovich, 1944; Shchelkin, 1949). This eventually led to the development of the Shchelkin spiral, essentially a helical insert along the wall of a tube, increasing the generation of turbulence and aiding in the occurence of DDT. Roughnesses not only increase turbulence, allowing for increased flame acceleration, but also present a surface for the leading shock to be reflected, increasing the temperature and pressure at this point. Shchelkin spirals are frequently used in PDCs and fairly effective at reducing the run-up distance required for DDT (Schauer et al., 2001; Panicker et al., 2006), although they create additional drag during the filling and purging phases. More importantly, however, they are very prone to thermal loading and difficult to cool. An example of the damaged caused by thermal loading can be seen in Fig. 2.7.

[3] Interestingly enough, Ernst Mach, to whom the epigraph at the beginning of this chapter is dedicated, promulgated the use of schlieren techniques and introduced a precursor method to what would later to be known as the soot-foil method for the investigation of shock waves, although he had no direct contributions to the study of detonations.

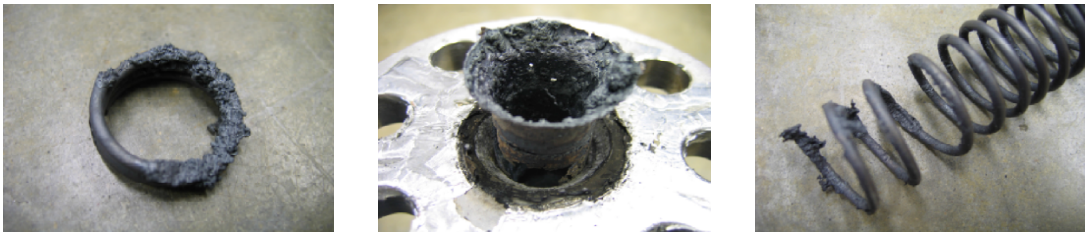

(a) (b) (c)

Figure 2.7: Damage suffered by Shchelkin spiral in a propane–oxygen PDC after 10–20 seconds of operation at 10 Hz. (a) Piece of spiral separated from the construction. (b) A portion of the spiral fused together. (c) A section of the spiral which has become melted, charred, and deformed. Photographs obtained from Panicker et al. (2006).

Other types of obstacles, such as orifice plates, may also be used for PDC applications in lieu of Shchelkin spirals (Cooper et al., 2002; Frolov, 2014). Such obstacles are characterized by the blockage ratio and the separation distances. Both of these properties play a different role in flame acceleration and DDT ensuing from shock–obstacle interaction. Many investigations have been conducted over the years with the goal of optimizing both blockage ratio and separation distance. As even the important works are too numerous to mention here, these will be referred to at the appropriate times in this manuscript with regards to the relevant experiments and results.

Detonation may also be initiated without an obstacle; the obstacle is replaced by an injected flow, creating a sort of virtual obstacle. Such a scheme removes the problem of thermal loading, as there is no physical obstacle present in the flow. Furthermore, the injection can be modulated in such a way that it is active only during the ignition and propagation phases of the cycle, resulting in less pressure loss during the filling and purging phases of the cycle (see Sec. 1.2).

Knox et al. (2011) investigated such a virtual obstacle in the form of a circumferential jet, forming what they called a "fluidic obstacle." A schematic of this principle is shown in Fig. 2.8. Essentially, the flow field behind a physical orifice is recreated in the detonation chamber using a circumferential slot injection scheme. Their investigations showed a significant decrease in pressure loss exhibited by the fluidic obstacle when compared to physical orifice plates of various sizes. In reacting studies using hydrogen–air mixtures, DDT was obtained with injection pressures in excess of 10 bar, but only at distances of over 1 m.

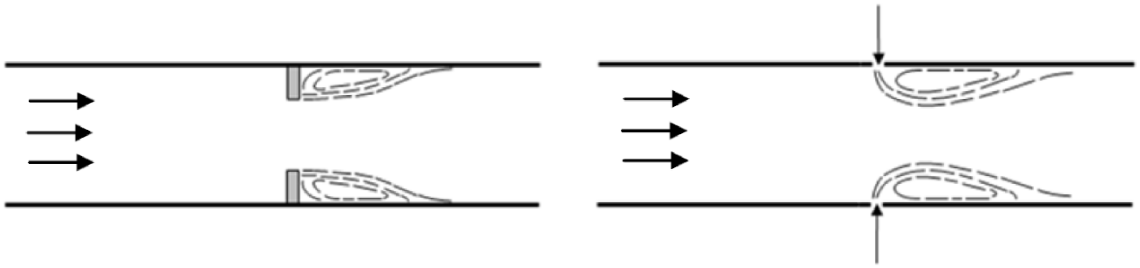

(a) Physical obstacle **(b)** Virtual obstacle

Figure 2.8: A schematic showing the working principle behind a virtual obstacle. Images taken from Knox et al. (2011).

A final, but very relevant method of detonation initiation is achieved by focusing a shock by means of reflection. When a shock is focused, the region in which it collapses upon itself experiences a much higher pressure increase than the original shock provides. Several experimental investigations have been conducted in which impinging shocks have been focused in combustible mixtures by a parabolic endwall (e.g., Achasov et al. (1994); Jackson et al. (2005); Gelfand et al. (2000)). Additionally, Gelfand et al. (2000) investigated shocks focused at endwalls of various geometries: two-dimensional wedges, semi-cylindric, and parabolic. The experiments were conducted on a shock tube setup with lean hydrogen–air mixtures. Both deflagration and detonation initiation were observed for different configurations and shock strengths. Most notable is the direct initiation of a detonation at the endwall with a half-angle of 45° (Fig. 2.9). Detonation initiation from the impinging shock was observed in this configuration for shocks with a Mach number $M \geq 2.52$ for the lean hydrogen–air mixture. Earlier investigations by Chan et al. (1990) showed this critical Mach number to drop to $M = 1.88$ in a similar configuration with a stoichiometric hydrogen–oxygen mixture and that a half-angle of 45° is most suited to the initiation of a detonation.

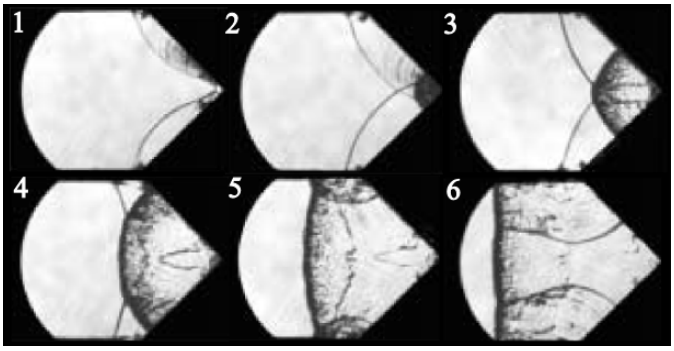

Figure 2.9: High-speed schlieren images of a shock impinging on an endwall with a half-angle of 45° resulting in the initiation of a detonation. Time between frames is 12 μs. Images taken from Gelfand et al. (2000).

2.7 Choked Flames and Quasi-detonations

During the process of DDT, the flame usually reaches a terminal velocity and propagates continuously at this speed until the boundary conditions allow for it to transition to detonation by means of one of the aforementioned mechanisms. This terminal velocity is around the speed of sound in the combustion products. For this reason, such a flame is known as a choked flame or a choked deflagration. After transition to a detonation, another phenomenon may be observed in which the detonation is seen to travel at a significant deficit to the CJ velocity. These detonations are known as quasi-detonations and result from the obstacles interfering with the detonation propagation. For an orifice plate, this occurs when the inner diameter of the orifice is significantly smaller than the critical tube diameter ($\approx 13\lambda$). As the diameter of the orifice opening approaches the critical tube diameter, the propagation velocity approaches CJ velocity. Both of these phenomena were recorded very methodically by Peraldi et al. (1986). For this reason, it is imperative for PDC applications to determine the number of necessary obstacles required for reliable DDT. More than this may result in quasi-detonations and more unnecessary sources of losses in efficiency.

2.8 Practical Examples for Propagating Flames and Shock Waves

In order to understand the mechanisms behind flame propagation and DDT through shock focusing, several examples are considered in the following. First, flame propagation from the closed end of an open-ended tube is discussed. Then, the gas dynamics involved in the propagation of a normal shock are presented. Finally, examples more relevant to this work, namely shock reflections, are discussed.

2.8.1 Propagating flame in a tube

First, we consider a flame propagating in a tube. The ignition end of the tube is closed and the end towards which the flame propagates is open. A schematic of this case is shown in Fig. 2.10. The problem may be approached simply using the continuity equation. The change in mass of the unburnt mixture (state 0) is defined as

$$dm_0 = -\rho_0 dV_0 = -\rho_0 S v_c dt, \tag{2.16}$$

where ρ_0 is the density of the unburnt mixture and dV_0 is its corresponding change in volume during the combustion process. This may be expressed over an infinitesimal time increment as $Sv_c dt$, where S is the surface area and v_c is the consumption speed. In the case of a planar, laminar propagating flame, this may be assumed to be equal to the laminar burning velocity. The resulting change in mass of the burnt mixture (state 1) is

$$dm_1 = \rho_1 dV_1 = \rho_1 S dx_f, \tag{2.17}$$

corresponding to the product of the surface area and the change in flame position. Due to conservation of mass, the negative change in mass of the unburnt mixture is equal to the positive change in mass of

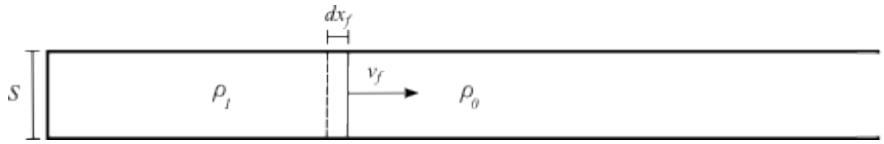

Figure 2.10: Schematic illustration of a propagating flame in a tube open at one end and closed at the ignition end.

the burnt mixture: $-dm_0 = dm_1$. Setting these expressions equal to each other and solving for the change in flame position per unit time allows for the flame propagation speed to be determined:

$$\frac{dx_f}{dt} = \frac{\rho_0}{\rho_1} v_c. \tag{2.18}$$

Here, it is clearly seen that the flame propagation speed is higher than the laminar flame speed by a factor equal to the density ratio of the unburnt to the burnt medium. For a stoichiometric hydrogen–air flame at atmospheric conditions, this is a factor of seven. This is an important aspect, resulting in an increase in propagation speed solely due to the expansion of the product gases and has implications on flame acceleration and DDT, which will be seen time and again in the rest of this work.

2.8.2 Propagating normal shock

Now, we consider a propagating normal shock through a quiescent gas in one dimension. As aforementioned, shocks are common ahead of fast propagating turbulent flames and, therefore, of interest. For this, the definition of the Mach number is required:

$$M_0 = \frac{u_0}{\sqrt{\gamma R_{\text{spec}} T_0}}, \tag{2.19}$$

where u is the velocity, γ is the adiabatic index, R_{spec} is the specific gas constant, and T is the temperature. Additionally, relations between the quantities before and after the shock are needed. These equations are derived in numerous books on gas dynamics (e.g., John (1984)) and will only be shown here in their final form:

$$\frac{p_1}{p_0} = \frac{2\gamma M_0^2}{\gamma + 1} - \frac{\gamma - 1}{\gamma + 1} \tag{2.20}$$

$$\frac{T_1}{T_0} = \frac{(1 + \frac{\gamma-1}{2} M_0^2)(\frac{2\gamma}{\gamma-1} M_0^2 - 1)}{M_0^2 (\frac{2\gamma}{\gamma-1} + \frac{\gamma-1}{2})} \tag{2.21}$$

$$\frac{u_0}{u_1} = \frac{(\gamma + 1) M_0^2}{(\gamma - 1) M_0^2 + 2}. \tag{2.22}$$

Subscripts 0 and 1 correspond to states before and after the shock wave, respectively. From these equations, the post-shock state may be calculated if the initial state of the gas (p_0, T_0, u_0, R_{spec}, and γ) and the shock propagation speed are known.

2.8.3 Normal shock impinging on a wall

Let us now examine the process of shock reflection, namely against a planar rigid surface (e.g., the endwall of a tube). Such experimental setups are actually quite common and are used, for instance, as shock tubes to measure ignition delay times in certain gas mixtures[4]. A schematic illustration is shown in Fig. 2.11 for the case of a shock reflecting from an endwall. First, a transformation into the shock-based frame of reference (stationary shock) is required, in order to determine the transformed velocities before and after the shock. Quantities in this frame of reference are designated with a circumflex (e.g., $\hat{u}_1$ and $\hat{u}_0$). As the shock is traveling into a stationary gas, $\hat{u}_0$ is equal to the impinging shock propagation speed W_i in the laboratory frame of reference and $\hat{u}_1$ is equal to $W_i - u_1$. From the initial conditions and W_i, the Mach number may be determined using Eq. 2.19. This, in turn, may be used to calculate p_1, T_1, and $\hat{u}_1$ using Eqs. 2.20, 2.21, and 2.22, respectively. The gas velocity u_1 behind the shock wave in the laboratory frame of reference may then be obtained from $\hat{u}_1$ using the aforementioned transformation and, subsequently, all properties after the passing of the impinging shock wave (state 1) are known.

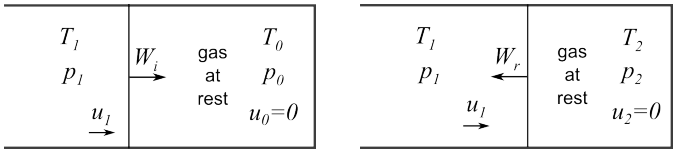

(a) Impinging shock **(b)** Reflected shock

Figure 2.11: Schematic illustration of a shock reflecting at a flat endwall. Due to the boundary condition at the wall, the gas at the wall is at rest both before and after the reflection, determining the shock reflection speed and dependent parameters.

Now, in order to determine the quantities at state 2, a zero-velocity boundary condition must be imposed at the endwall. This means that the gas at state 2 after the reflected shock is now at rest. We can use this to our advantage in determining the reflected shock propagation speed W_r. We have two unknowns, namely W_r and M_r and a system of two equations (Eq. 2.19 and Eq. 2.22). Writing these equations relative to the shock results in

$$M_r^2 = \frac{(\hat{u}_1 + W_r)^2}{\gamma R_{\text{spec}} T_1} \text{ and} \tag{2.23}$$

$$\frac{\hat{u}_1 + W_r}{W_r} = \frac{(\gamma+1)M_r^2}{(\gamma-1)M_r^2 + 2}. \tag{2.24}$$

[4]Interestingly, the first shock tube was developed by none other than Paul Vieille, the French pharmaceutist and co-discoverer of the detonation.

Solving this system of equations, we obtain W_r and M_r, from which p_2 and T_2 can be determined (u_2 is zero due to the imposed boundary condition). A specific example may be found in the book by John (1984).

2.8.4 Normal shock impinging on a v-shaped endwall

Finally, we will consider the example investigated by Gelfand et al. (2000), that of a shock impinging on a v-shaped endwall with a half-angle of 45° . The shock focusing aspect of this case has implications for the work presented in this thesis. The process from state 0 to state 1 is exactly the same as in the preceding example. Therefore, we will begin at the point at which the shock is reflected from the converging section of the endwall. A sketch of the shock reflection process is presented in Fig. 2.12. In this case, a boundary condition is imposed in which the velocity perpendicular to the endwall (top and bottom, respectively) is zero. As a result, the reflected shock then propagates back upstream at an angle of 45° with respect to the flow. Using Eq. 2.22 in the shock-based frame of reference, the Mach number of the reflected shock may be expressed as

$$\frac{u_{1n} + W_r}{W_r} = \frac{(\gamma + 1)M_r^2}{(\gamma - 1)M_r^2 + 2}, \tag{2.25}$$

where W_r is the reflected shock propagation speed, $u_{1n} = u_1 \cos 45°$ is the velocity of the flow normal to the reflected shock, and M_r is the corresponding Mach number of the shock wave, defined as

$$M_r = \frac{u_{1n} + W_r}{\sqrt{\gamma R_{\text{spec}} T_1}}. \tag{2.26}$$

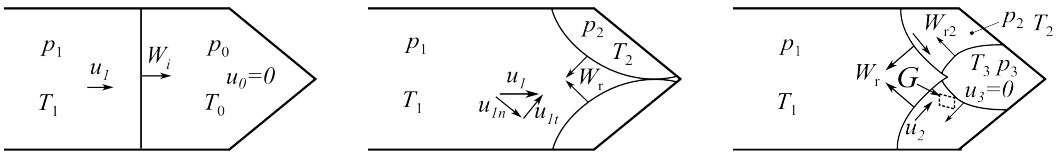

(a) Initial impinging shock

(b) Shock waves reflected at 45° with respect to u_1.

(c) Reflected shocks crossing in center region.

Figure 2.12: Schematic illustration of shock waves reflecting from a v-shaped endwall. The focusing of the reflected shocks results in significantly higher pressures and temperatures near the centerline.

At this point, obtaining an implicit solution to this system of equations becomes fairly messy, because with every step, the solution becomes a successively longer expression and its simplification presents a very tedious task. For this reason, the example will be continued explicitly. Let us assume an impinging shock Mach number: $M_0 = 2.53$. With the additional assumptions of $\gamma = 1.4$, $R_{\text{spec}} = 479.37\ \text{J/(kg} \cdot \text{K)}$, $T_0 = 293\ \text{K}$, and $p_0 = 1.013\ \text{bar}$, enough information is known to calculate state 2 and the propagation velocity of the reflected shock ($W_r = 510.5\ \text{m/s}$) from the previously

presented relationships[5]. State 3 can be obtained, for example, by considering a volume element just below the centerline in the region where the shock reflected from the bottom of the nozzle and the shock reflected from the top of the nozzle cross (labeled G in Fig. 2.12c). In this case, the shock wave traveling from bottom to top brings the gas to state 2 and the velocity of the gas at state 2 is zero in the direction perpendicular to the lower wall of the nozzle. After the shock waves cross, the shock reflected from the top wall of the nozzle travels into the gas already at state 2. Its propagation speed W_{r2} is also slightly higher than W_r, as the gas at state 2 is at a higher temperature and pressure due to the preceding shock (622 m/s). This is also illutrated in Fig. 2.12c. This second shock imposes the zero-velocity boundary condition from the bottom wall and brings the gas to rest. By once again using Eq. 2.25 and Eq. 2.26, W_{r2} and M_{r2} may be calculated, and consequently, p_3 and T_3 may also be determined.

In order to put the shock focusing aspect of the endwall into perspective, we may compare the respective pressure increase with that obtained for a shock wave impinging on a flat endwall (see Sec. 2.8.3). For a shock wave at $M_0 = 2.53$, the resulting pressure after the reflected shock is 31.9 bar. In contrast, the resulting pressure for an identical shock wave impinging on a v-shaped endwall is already 21.9 bar at state 2 after the first reflection and reaches 55.3 bar at state 3. The corresponding temperature at this state is 1197 K. The ignition behavior of this gaseous mixture at the elevated pressure and temperature may be analyzed with the help of a zero-dimensional reactor. Using Cantera with the Burke mechanism, as in Sec. 2.5.2.2, the ignition delay time may be calculated. The temperature with respect to time is presented in Fig. 2.13. The fact that the autoignition limits are surpassed by the initial pressure and temperature is shown by the sudden change in temperature due to the reaction. The ignition delay time is defined as the time until the maximum in the temperature gradient is reached. This occurs at around 70 μs. Thus, the conditions created by the focusing of the shock at a v-shaped endwall are sufficient to create the autoignition necessary for a hot spot synonomous to Oppenheim's "explosion in the explosion," which is a prerequisite for the initiation of a detonation, as described in Sec. 2.6.

[5]The gas constant is calculated for a stoichiometric mixture of hydrogen and air enriched to 40% oxygen, the reason for which will be explained later.

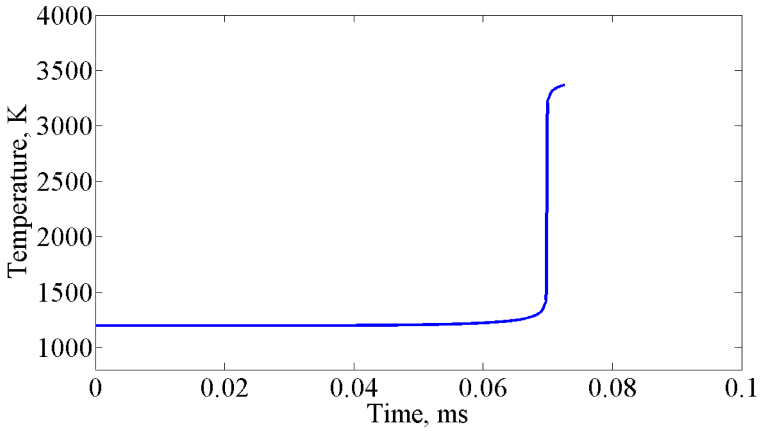

Figure 2.13: Simulation of ignition delay using a zero-dimensional reactor. The simulation was conducted for a stoichiometric mixture of hydrogen and air enriched to 40% oxygen, using initial conditions corresponding to state 3 in Fig. 2.12, namely, 55.3 bar and 1197 K.

3 Experimental Methods and Facilities

Richard Becker, under whom Werner Döring obtained his doctorate, published his noted work during his habilitation under Max Plank in Göttingen and shortly afterwards as a physics professor at the Technische Universität Berlin (then Technische Hochschule Berlin), where he conducted fundamental work on detonation waves during the 1920s and 1930s (Becker, 1922). However, since this time, there has been very little research carried out at the university in this field. As such, research on pressure-gain combustion at the Chair of Fluid Mechanics at TU Berlin was required to begin in the form of preliminary investigations. These investigations are summarized in the following. First, the required measurement techniques will be introduced and summarized. Then, the preliminary experiments conducted in the course of this work will be presented and described. Finally, the pulse detonation test facility will be introduced, including a novel approach for achieving DDT using shock focusing, being the culmination of the work contained in this thesis.

3.1 Instrumentation and Experimental Techniques

In this section, the various measurement techniques will be briefly described. Ionization probes were used to determined the velocity of reaction waves. Piezoelectric pressure transducers were also used in this respect, with the obvious advantage that pressure could be additionally measured. Laser sheet tomography (LST) was employed in order to investigate the influence of obstacles of varying geometry on initial flame propagation. Particle image velocimetry (PIV) was used in a water test bench in order to capture the flow field for various virtual obstacles. Finally, high-speed shadowgraphy was employed in order to visualize the leading shock and high-speed imagery was used to characterize DDT events.

3.1.1 Ionization probes

Ionization probes are frequently used for the purpose of flame and detonation detection (e.g., Kowalkowski et al. (2009), Driscoll et al. (2013)). In the case of detonation waves, they are a robust, inexpensive, and uncomplicated way of determining the propagation velocity. They function on the principle that ionized species created during combustion events allow for an electric current to flow between two electrodes when an electric potential difference is applied. In the presence of sufficient ionized gases, a current flows and the voltage between the electrodes falls to zero. In the automotive industry, this principle has been applied extensively for diagnostic purposes (e.g., Eriksson and Nielsen (1997)), simply using the spark plug as a probe during times between ignition events.

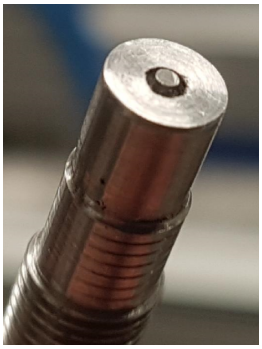

(a) Close-up of ionization probe.

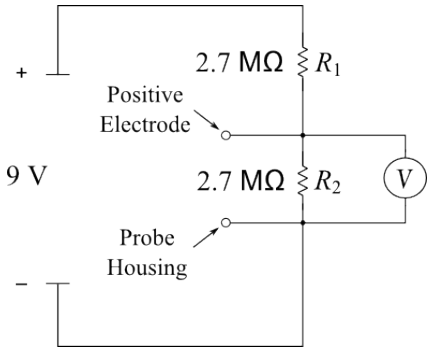

(b) Circuit diagram for the ionization probe.

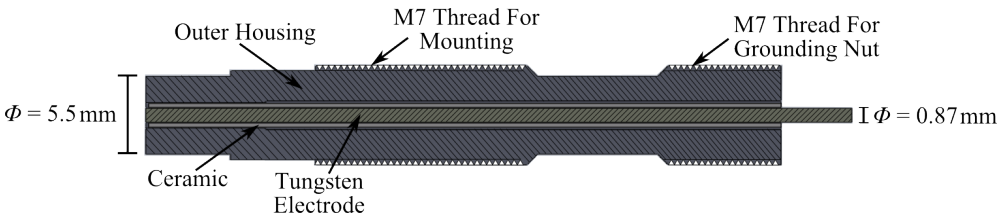

(c) Schematic of the ionization probe.

Figure 3.1: Ionization probe developed at TU Berlin. The geometry is compatible with the PCB pressure transducers in order to allow flush mounting in the same ports. A 9 V battery is used as a power supply. The voltage is measured over the positive electrode (tungsten rod) and the negative electrode (probe housing).

In the course of this work, two designs for ionization probes were used. For the first, a typical automotive spark plug was used with a diameter of 14 mm. As the spark plugs are fairly large and intrusive, a compact design was developed with a diameter of 5.5 mm, having the same general geometry as the pressure transducers (see Sec. 3.1.2). This allowed for the sensors to be easily interchanged using the same flush-mounting ports as the pressure transducers. A tungsten rod with a diameter of 0.87 mm was used as the positive electrode, separated from the housing by a ceramic sheath. The housing is grounded over the test rig and used simultaneously as the negative electrode. The geometry of the ionization probes is presented in Fig. 3.1, along with the electronic circuit used for the measurements.

A standard 9 V battery is used for the electric potential. Two high-resistance resistors (R_1 and R_2, 2.7 $M\Omega$) are installed in series in order to force a low current, extending battery life and allowing for a signal V of less than 5 V to be obtained. When ionized gases from the combustion are present between the positive electrode and the probe housing (negative electrode), current flow across this shorted connection and the potential drop across R_2 falls to zero. This event is registered as the arrival of a reaction front.

Ionization probes can be used at much higher operating temperatures than pressure sensors, allowing for multi-cycle operation. They also exhibit very quick response times. However, they provide merely temporal information on the arrival of a reaction front and give no information on the pressure, although it is possible to determine the post-combustion pressure based on the decay of ionized species (see Zdenek and Anthenien (2004)).

3.1.2 Piezoelectric pressure tranducers

Piezoelectric pressure transducers operate on the principle of the so-called piezoelectric effect. When a piezoelectric crystalline material (frequently quartz) is stressed, it generates a charge. This charge is proportional to the pressure on the crystal. However, this type of transducer is only suited to measuring relatively short-term changes in pressure. If a certain constant pressure is applied to the transducer, the charge will dissipate after a short time (typically one to several seconds). In the case of detonation and shock waves, the processes of interest take place at very small time scales, so this effect may be neglected.

Nevertheless, there are two clear disadvantages to piezoelectric pressure transducers. The first is the phenomenon known as thermal shock. Due to shock heating of the transducer housing and piezoelectric crystal, both the response of the crystal and its preset stress are compromised through changes in piezoelectric properties and thermal forces and moments, respectively, resulting in a short-term negative pressure bias (Birman, 1996). Furthermore, long-term heating of the transducer from successive firing events, may lead to a negative drift in the pressure signal due to similar effects. Both of these effects are illustrated in Fig. 3.2 for the passing of detonation waves at a frequency of 5 Hz. Here, it is shown that the negative bias from the thermal shock persists nearly throughout the entire cycle of 0.2 s and the long-term heating of the sensor results in a -3 bar drift after only seven cycles. Figure 3.3 illustrates how both ionization probes and pressure transducers may be used to determine the speed of reaction waves using the time-of-flight method.

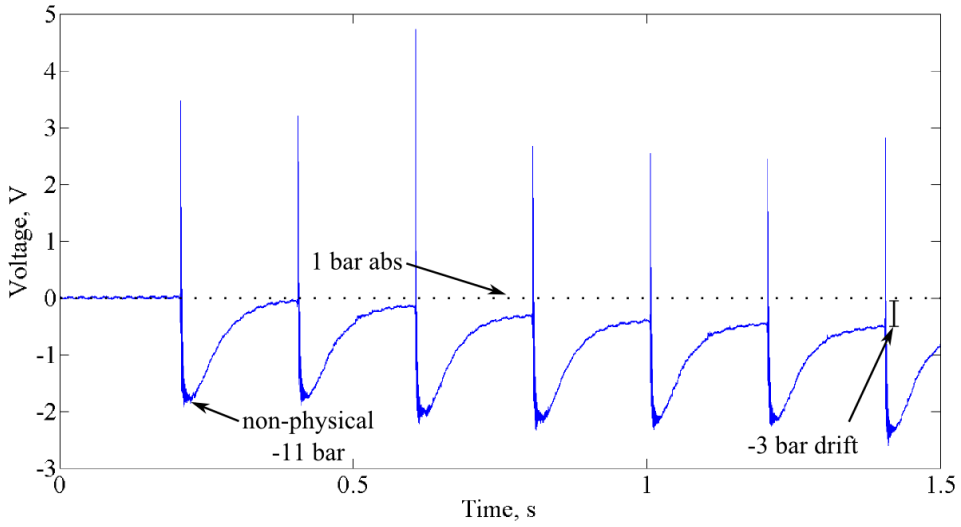

Figure 3.2: Thermal effects on piezoelectric pressure transducers for a firing frequency of 5 Hz. Thermal shock is evident by a non-physical pressure of -11 bar after every firing event. Long-term heating over several events manifests as a gradual negative drift over time (here -3 bar after 1.5 seconds).

3.1.3 Laser sheet tomography

Frequently in combustion experiments, a technique called laser sheet tomography is used to identify the interface between burnt and unburnt gases (flame front). Several works may be found taking advantage of this technique (Chew et al., 1989; Shepherd, 1996). The principle is based on the fact that fine droplets are evaporated during the combustion process. A laser sheet is produced and directed into the measurement area. The droplets, typically composed of olive oil or silicon oil are seeded into the flow. These droplets are illuminated by the laser and the scattered light may be captured by a camera. As the flame travels through the tube, in the case of a propagating flame, or as the unburnt gases travel through the flame, in the case of a stationary flame, the droplets are vaporized and the laser light is no longer scattered. This results in the burnt gases appearing as dark regions. Fig. 3.4 presents images of the "tulip flame" phenomenon taken using LST on the setup described in Sec. 3.2.

Flammable oils, such as olive oil, may also burn in this process, somewhat changing the heat release and chemical processes that occur. Therefore, such oils may not be suitable for some applications, for example, those in which a very accurate laminar flame speed is desired. The endothermic process of vaporization of the oil droplets, also requires heat even if the oil is non-flammable, effectively stealing energy from the system and changing the temperature and rate of reactions. However, Zhang et al. (1988) determined based on the latent heat of vaporization of silicon oil and measurements conducted in their laboratory that fine oil droplets (2–4 μm) at typical concentrations took only 0.2% of the heat release to be vaporized. Thus, this effect may be neglected at least for the setup considered by these authors with propane–air flames. Furthermore, Barnard and Bradley (1984) determined that the vaporization of a 3 μm droplet takes around 10^{-5} s, allowing for the interface between burnt and unburt

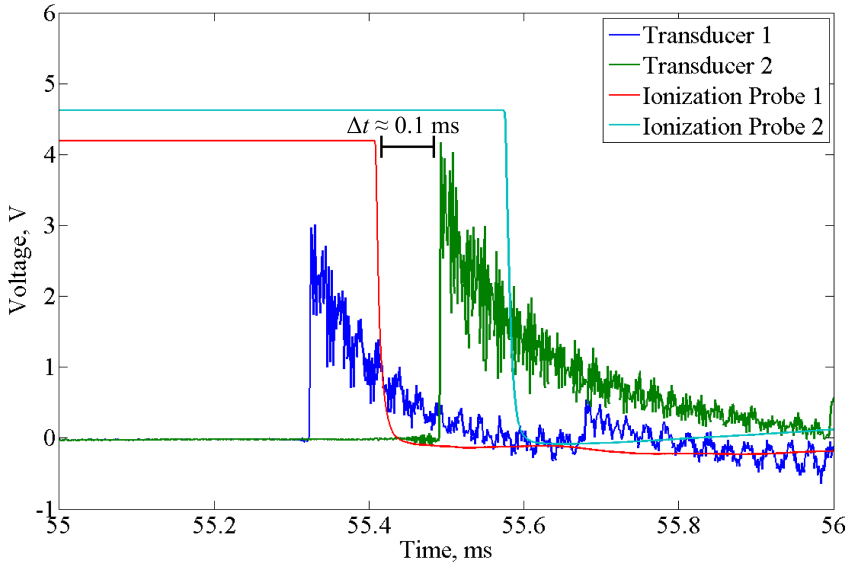

Figure 3.3: Signals from alternately placed pressure transducers and ionization probes at 200 mm intervals. By determining the times between the arrival of the reaction wave at each position, the wave velocity may be determined using the time-of-flight method.

gases to be accurately located. Both Zhang et al. (1988) and Barnard and Bradley (1984) profess that at the high temperatures present in the flame, even silicon oil would burn; however, based on the low concentration of oil droplets, the resulting heat release is "almost certainly negligible."

3.1.4 Particle image velocimetry

Particle image velocimetry is an optical measurement technique used to measure the velocity field in fluids. In the most basic configuration, a laser sheet is directed through a field of interest, illuminating seeding particles (or even smoke). The particles scatter the light, which is then captured by a single camera perpendicular to the light sheet. If two images are captured within a short succession, an image pair is obtained. This image pair must be post-processed in order to calculate the two-dimensional velocity components in the plane of the laser sheet.

In essence, the displacement of the particles in the timespan between the two images corresponds to the flow velocity in the region of these particles. However, the reality is much more complex. Simply tracking the particles themselves results in much noise and high error margins, since the single particles are barely resolved by the camera. Yet, small particles must be used in order to reduce their inertia and allow them to follow the fluid motion. Much higher quality data may be obtained if a cross-correlation scheme is employed. Essentially, a cross-correlation function is calculated. A region of the flow field, also known as the interrogation window, is considered for the first image of the pair $f(m, n)$, where m

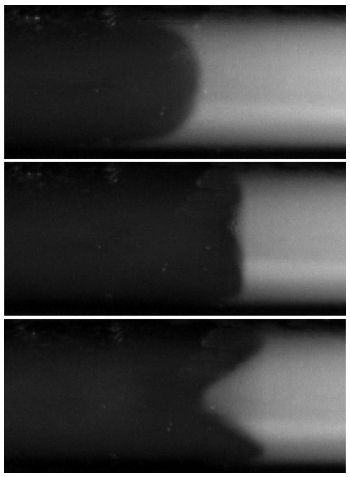

Figure 3.4: Tulip flame observed using LST on the test bench described in Sec. 3.2. As the flame propagates from left to right (frame 1), it comes to a halt due to the acoustic field in the tube (frame 2), and an instability develops in the flame front (frame 3). The interface between burnt and unburnt gases is made visible by the evaporation of oil droplets in the burnt gas which no longer reflect the laser light.

and n are the x and y coordinates, respectively. The output region $g(m, n)$ from the second image then relates to the first image as follows:

$$g(m, n) = [f(m, n) * s(m, n)] + d(m, n), \tag{3.1}$$

where * denotes the two-dimensional spatial convolution of the two functions $f(m, n)$ and the spatial shifting function $s(m, n)$. This spatial shifting function may be considered in the discrete case to be a Dirac delta function in two dimensions: $s(m, n) = \delta(m - i, n - j)$. When the additive noise process $d(m, n)$ is considered negligible, the spatial shifting function may be determined from a cross-correlation between the two images $f(m, n)$ and $g(m, n)$, ideally resulting in a cross-correlation coefficient near one. In this case, the value of the spatial shifting function corresponds to the average displacement of the particles within the interrogation region. Decreasing the size of the interrogation windows increases the spatial resolution of the calculated flow field, but also increases the noise in the system, which at some point, no longer remains negligible. The art of PIV is finding a balance between accuracy and flow field resolution. A more comprehensive summary of digital PIV is given by Willert and Gharib (1991).

3.1.5 Shadowgraphy

Shadowgraphy takes advantage of the fact that light is refracted when passing through a volume with density gradients. When parallel light is sent through a volume with such gradient, this results in areas of higher and lower intensities, accentuating areas of density gradients. A detailed overview of shadowgraphy systems and techniques is given by Settles (2001). The first shadowgraph visualizations seem to be a curious bi-product described by Robert Hooke in his *Micrographia*, in which he primarily

presented his work in microscopy, where he first coined the biological term cell; However, Hooke, understood the optical phenomenon and described it in suprising detail (Hooke, 1665). Shadowgraph systems typically have a lower sensitivity when compared to schlieren systems, as they capture only the second spatial derivative of density, as opposed to the first spatial density gradient. However, they have the advantage of capturing these density gradients in two dimensions and their alignment is less tedious, allowing for the system to quickly be adjusted to investigate different measurement volumes.

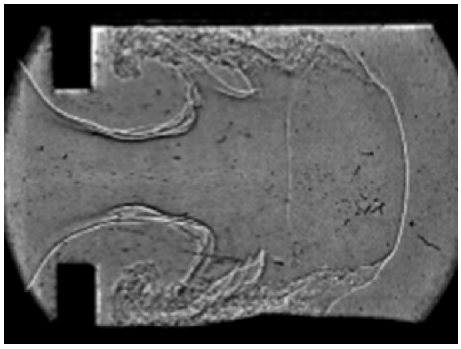

Figure 3.5: Example shadowgraph image of an initially laminar, stoichiometric, hydrogen–air flame passing through a gate-type obstacle. Image was taken with the setup described in Sec. 3.6.3.

3.2 Experimental Setup for Flame Acceleration

As efficient flame acceleration is imperative to reliable DDT, experiments were first conducted in order to sufficiently characterize this process using obstacles. For these investigations, an experiment was designed using LST (see Sec. 3.1.3) in order to visualize the flame propagation. The effects of a single obstacle of varying shape were first investigated. The obstacle shapes used in the measurements are shown in Fig. 3.6, each having a blockage ratio of 0.43. This value has proven to be advantageous for flame acceleration in several studies (Lee et al., 1985; Guirao et al., 1989; Ciccarelli and Dorofeev, 2008). The blockage ratio is defined as the ratio of the cross-sectional area blocked by the obstacle to the entire cross-sectional area. In the case of an orifice plate, for example, this equates to

$$\text{blockage ratio} = \frac{D_t^2 - D_o^2}{D_t^2}, \tag{3.2}$$

where D_t is the inner diameter of the tube and D_o is the diameter of the orifice. The obstacles were designed to create turbulence and flame folding in different cross-sectional locations and on different scales. Orifices create an axisymmetric recirculation zone on the walls of the tube while discs create an axissymmetric recirculation zone in the middle of the tube. Plates, on the other hand, create non-axisymmetric recirculation zones. Plates of varying geometries were used in order to create interacting recirculation zones and turbulence on different scales. Furthermore, geometries with serated edges were used to produce finer turbulence. All obstacles have a thickness of 2 mm.

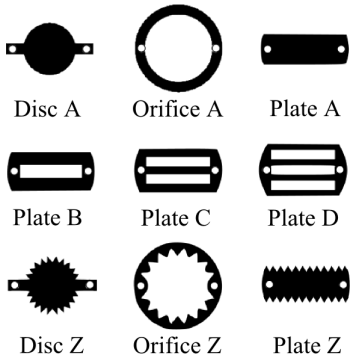

Figure 3.6: Various types of obstacles investigated for the purpose of flame acceleration. All obstacles have been sized to have a blockage ratio of 0.43 for a tube with an inner diameter of 30 mm.

Each of the obstacles were installed at a distance of 100 mm by means of two rods with a diameter of 2.5 mm. Additionally, experiments were conducted in which no obstacle was installed. A constant wave (CW) diode-pumped solid-state laser (Quantum Finesse, 532 nm) was focused into a light sheet with a thickness of around 1 mm using a series of collimating lenses and a cylindrical lense. The resulting light sheet was directed down the center of an acrylic glass tube with a diameter of 30 mm. The combustion air was first directed through an oil seeder (Palas AGF 10.0) producing droplets of dioctyl sebacate ($C_{26}H_{50}O_4$) with a mean diameter of 0.5 μm and a cutoff diameter of 10 μm. The laser light reflected from the seeding droplets was recorded using a high-speed camera (Photron FASTCAM SA1.1) at 16,000 fps. The result is a cross-sectional visualization of the propagating flame. Based on the aforementioned evidence from Barnard and Bradley (1984) and Chew et al. (1989), both the vaporization heat and the heat release during combustion of the droplets was considered to be negligible. Even if the influence is more substatial than in the cited studies, the main goal of this investigation is to compare the performance of various obstacles for the same mixture. As such, the influence of the oil droplets is assumed to be immaterial.

The experimental setup and example LST images are shown in Fig. 3.7. Due to the fact that the seeding droplets scatter the light, it was necessary to shorten the tube to 350 mm. Otherwise, so much light is scattered along the length of the tube that the area of interest is insufficiently illuminated. However, this length is sufficient for investigating initial flame acceleration. A stoichiometric hydrogen–air mixture was used with mass flows of 3.1 kg/h of air and 0.092 kg/h of hydrogen. The mass flow rates were measured using Endress + Hauser Coriolis mass flow meters (air: Promass A; hydrogen: Promass 80). The tube was filled with the mixture for ten seconds in order to ensure that recirculation areas behind the obstacles contained the correct mixture. After simultaneously ceasing the flow of both gases by closing pneumatically controlled valves, the mixture was given ten seconds to reach a nearly quiescent state, afterwhich the mixture was ignited using a spark plug. A region of air from outside of the tube was observed to penetrate the tube during the settling time, but did not reach the obstacles. After ignition, however, this gas was expelled well before the flame arrived, having little to no effect on the experiment.

Finally, in order to determine the optimum spacing of the obstacles, investigations were also conducted using two and three orifice plates (corresponding to Orifice A in Fig. 3.6). In these investigations, the first obstacle was placed at 50 mm from the spark plug. The same procedure was used as for a single obstacle.

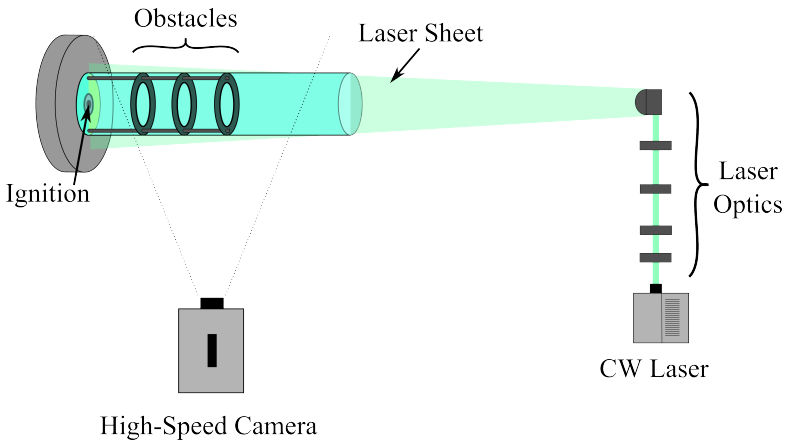

(a) Experimental setup

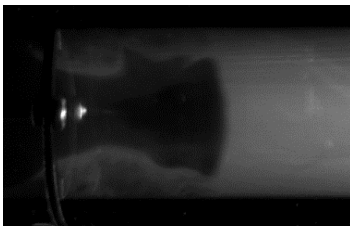

(b) Example image for Orifice A

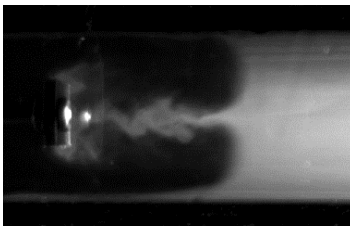

(c) Example image for Plate A

Figure 3.7: Experimental setup for LST measurements for the investigation of flame acceleration. A laser sheet is directed into a tube, illuminating silicon oil seeding droplets which are then recorded by a high-speed camera. Example photographs are shown in (b) for Orifice A and (c) for Plate A.

3.3 DDT Test Bench

After conducting experiments in flame acceleration, an experiment was designed with enough obstacles to cause DDT. The intent of this setup was to determine the minimum number of required obstacles and the optimum obstacle spacing for reliable DDT. Furthermore, the effect of the inner diameter of the tube on DDT was investigated. Based on the results from the flame acceleration experiments (see Sec. 4.1), it was decided that orifice plates would be the most sensible type of obstacle to investigate. A tube with a length of 1,500 mm and an inner diameter of 39 mm was used as an outer sheath into which tubes with smaller inner diameters (30 mm and 32.8 mm) could be inserted. Orifice plates were manufactured for each tube diameter having a blockage ratio of 0.43. For the two smaller diameters, inserts were prepared with lengths of 40 mm to 100 mm in 10 mm increments. These inserts were used as spacers to separate the orifice plates. This principle is shown in Fig. 3.8 along with the rest of the

test bench. The entire construction of inserts and orifice plates was held in place with an end plate and a spring at the downstream end of the tube. For the tube of largest diameter, no inserts were able to be used and the orifice plates were positioned using the technique described in Sec. 3.1.3.

(a) DDT test bench

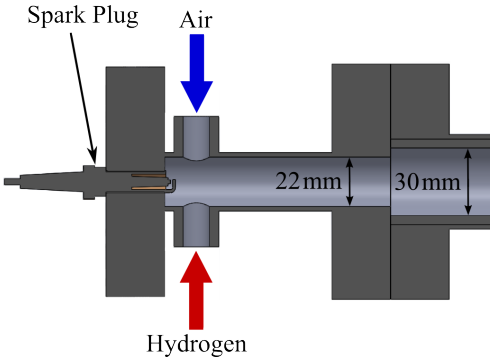

(b) Injection geometry

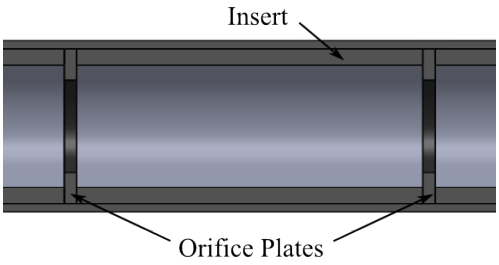

(c) Assembly for inserts and orifice plates assembly

Figure 3.8: Test bench for DDT investigations showing details of the injection geometry and the assembly of the inserts and orifice plates. A variation with an insert inner diameter of 30 mm and a length of 85 mm is shown.

The tube was filled with a stoichiometric mixture of hydrogen–air from opposing openings with a diameter of one quarter inch into a mixing section with a length of 100 mm. Mass flow rates were the same as in Sec. 3.2, measured using the same Coriolis mass flow meters. A spark plug is installed at the center of the headwall of the tube. The reaction wave was recorded using ionization probes in the form of a further four spark plugs with a separation distance of 200 mm. As in Sec. 3.2, the tube was filled for ten seconds. After this time, the hydrogen and air valves were closed simultaneously. Ten seconds were then given for the mixture to reach a quiescent state, at which point, the ignition signal was sent by the data acquisition system (NI cDAQ-9188) using an analog output module (NI 9265). The signals from the ionization probes were recorded using an oscilloscope (Agilent Technologies, DSO-X 3024A) with a sampling rate of 200 MHz.

3.4 Investigation of Virtual Obstacles: Water Test Bench

Based on experiments conducted at the Air Force Research Laboratory's Pulse Detonation Research Facility (Knox et al., 2010, 2011), investigations into virtual obstacles were deemed to be a sensible endeavor. A water test bench was developed for flow field measurements using PIV for various types of injection schemes. The basic infrastructure of the test bench was designed and built by Bernhard Bobusch for the purpose of mixing investigations within the Collaborative Research Center 1029 (Bobusch, 2015). It consists of a main water circuit supplied by a 300 L tank. The water pressure is supplied by a pump and the flow rate is regulated by a hand-operated gate valve. After the water is

pumped through the test bench, it is returned via a hose positioned above the water tank. The setup is shown in Fig. 3.9 and will be discussed in more detail in the following. Another flow circuit is used for the injection flow. In the case of PIV measurements, the same medium may be used and the circuit draws water from the same tank as the main circuit. Here, another pump provides the pressure for the injection circuit. A proportional control valve is used to regulate the injection flows using a National Instruments data acquisition system (NI cDAQ-9172), with an analog output module (NI9264).

The volume flow rates of the main flow circuit were calibrated by setting the gate valve in various positions and recording the time required to fill a 50 L tank. Desired flow rates were then determined by trial and error until obtained. Experience showed that calibration runs were repeatable to within about 2 seconds. The highest flow rate investigated in the main circuit was 67.9 L/min, resulting in a bulk velocity of 0.9 m/s and an error of 4.5%. This was deemed acceptable for the current investigation. Calibration of the injection circuit was also conducted using this technique, setting the valve position using the data acquisition system. Injection flow rates of up to 9 L/min were investigated. The smaller volume flow rates (compared to the main circuit) also allowed for much more precise calibration of the injection circuit.

The geometry of the experimental setup is shown in Fig. 3.9 and will be discussed in more detail in the following. The setup is constructed out of acrylic glass using the geometry for the modular pulse detonation combustor setup (see Sec. 3.6). The inlet geometry consists of a centerbody simulating that designed for the combustion test bench and a porous plate in order to improve mixing during the filling phase. The porosity at the inlet taking the slot, centerbody, and porous plate into account is around 44%. Three orifice plates with a blockage ratio of 0.43 were installed to replicate the flow field in the combustor with a separation distance of 85 mm, the first being installed at 50 mm from the porous plate. Since, the highest thermal loading of the orifice plates occurs at the point of DDT, the position of the fourth orifice plate was designed for the installation of various discs. At this position, not only could an orifice plate be installed, but also discs designed to provide different types of jets in crossflow, in order to create the virtual obstacles. The measurement domain is within an acrylic glass block. The outer surface of the block is square (110 mm x 110 mm) and the inner surface was circular, corresponding to the inner diameter of the rest of the test bench (40 mm). The length of this section is 170 mm.

The reason for the square cross-section is to reduce optical refraction at the outer interface. Refraction results in distortion of the image. This concept is illustrated in Fig. 3.10. When a beam of light impinges at an angle upon an interface between two materials exhibiting differing refractive indices, for instance air ($n = 1$) and acrylic glass ($n = 1.49$), it is refracted to a degree proportional to the inverse ratio of these indices according to Snell's law:

$$\frac{\sin\theta_1}{\sin\theta_2} = \frac{n_2}{n_1}, \tag{3.3}$$

where θ_1 is the incidence angle, θ_2 is the refraction angle, and n_1 and n_2 are the respective refractive indices. The curved interface between the acrylic glass and the water cannot be avoided without altering the geometry of the measurement domain and, thus, the flow field. However, the ratio of the refractive indices between water ($n = 1.33$) and acrylic glass is significantly closer to 1 than that of the ratio

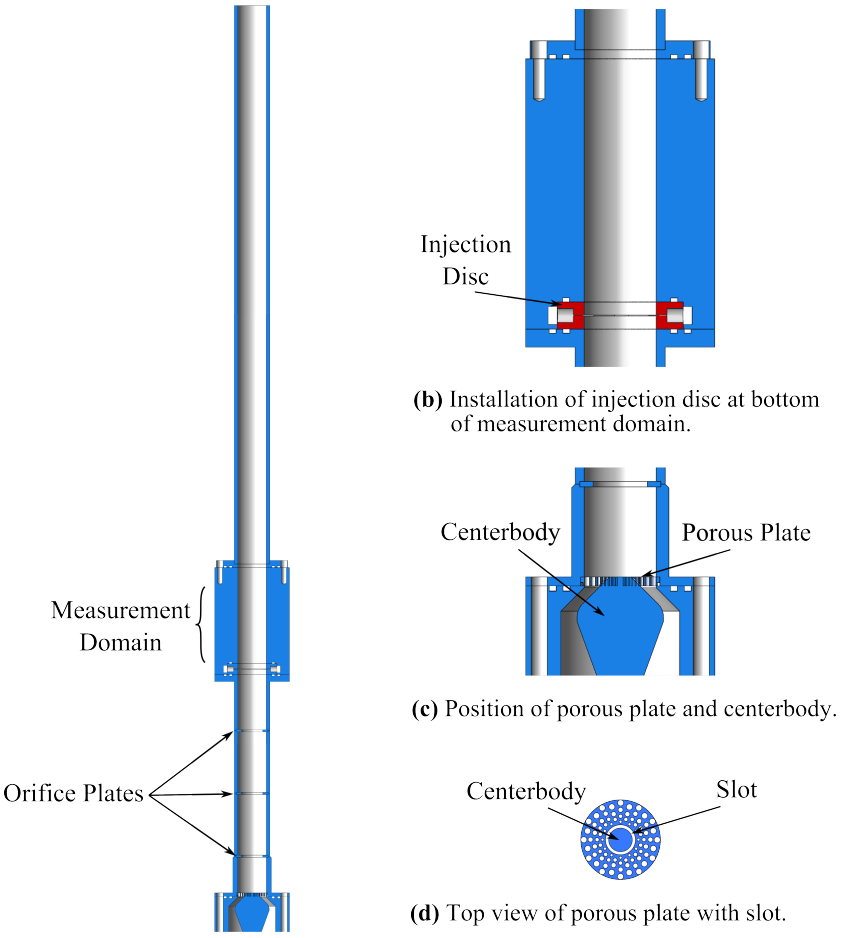

(a) General view.

(b) Installation of injection disc at bottom of measurement domain.

(c) Position of porous plate and centerbody.

(d) Top view of porous plate with slot.

Figure 3.9: Water test bench with details of the injection geometry and installation of the injection disc. Three orifice plates with a blockage ratio of 0.43 are installed upstream of the measurement domain. The tube has an inner diameter of 40 mm.

between acrylic glass and air and, therefore, poses less of a problem. The square cross-section results in an incidence angle of near 0° and removes this source of distortion from the image. This is important, because the more distorted the image is, the more inaccurate the calculated velocity measurements will be for the corresponding component.

The disc variations investigated in this study are shown in Fig. 3.11. The different injection schemes are intended to produce various flow fields and a variance in the spatial distribution of the turbulence intensity. These injection schemes included thirteen round jets (diameter 1.3 mm), thirteen square jets (1.5 mm x 1.9 mm), a circumferential slot (slot width of 0.4 mm) and thirteen sweeping jets created by fluidic oscillators. Fluidic oscillators may be designed to produce a sweeping jet at the outlet if a steady-state flow is imposed at the inlet. The premise is to increase turbulence and mixing in the injection plane compared to steady-state injection schemes. Fluidic devices include an entire family of

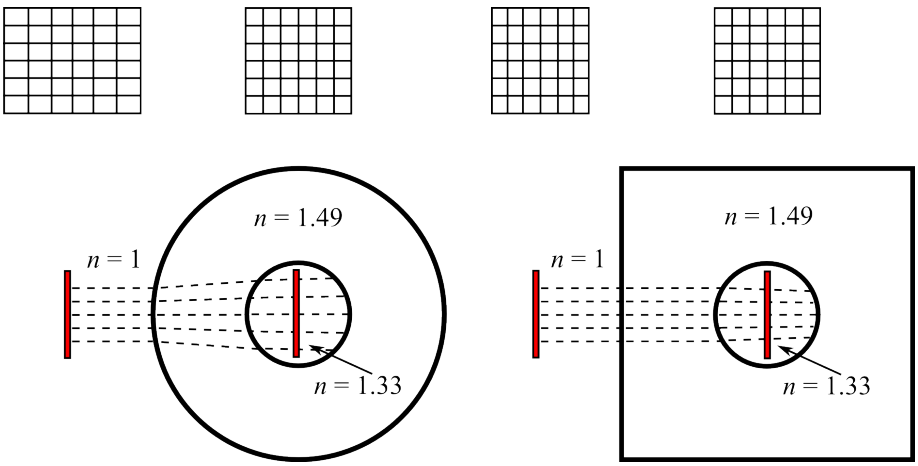

(a) Round outer interface. **(b)** Square outer interface.

Figure 3.10: Illustration of the light refraction at the interfaces between air ($n = 1$), acrylic glass ($n = 1.49$), and water ($n = 1.33$). The grid depicts how an image at the center of the water will be distorted when viewed from the air. The image viewed through two curved interfaces will appear elongated, while the image viewed through only one curved interface will be slightly compressed.

various geometries, including diodes, bistable switches, amplifiers, etc. Details on these devices, which have no moving parts, and the fundamentals on how they operate may be found in Angrist (1964). The fluidic oscillators used in this work are described in Bobusch et al. (2013). The inner diameter of the discs corresponds to the inner tube diameter. The injector outlet is located at this diameter. The openings in the outer surface sit in an annular chamber fed by four tubes connected to the outlet of the proportional control valve, serving as the injector inlet. Additionally, a standard orifice plate with a blockage ratio of 0.43 with no injection could be installed at the same position to provide a baseline.

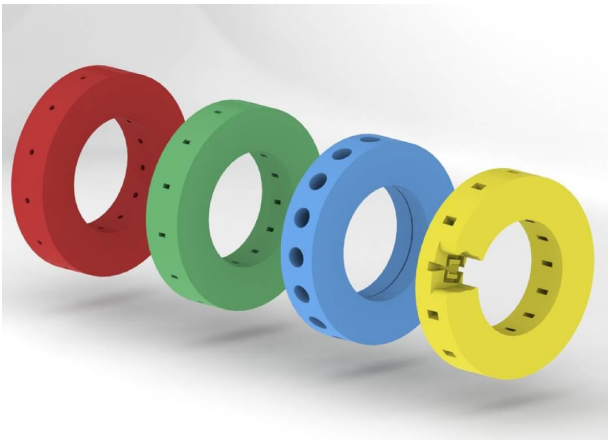

Figure 3.11: Injection discs for virtual obstacles. From left to right: round jets, rectangular jets, circumferential slot, and fluidic oscillators. Geometries developed by and image taken from Bobusch (2015).

The PIV system consisted of a high-speed laser (Quantronix Darwin Duo 100 Nd:YLF) and a Photron

FASTCAM SA1.1 high-speed camera. The laser exhibits a frequency doubler to obtain green light at 527 nm. A band-pass filter was used to remove light at other wavelengths (532 $\pm$2 nm, half-power bandwidth 20 $\pm$2 nm). Using an articulated mirror arm equipped with a cylindrical lens, the laser was expanded into a sheet with a thickness of around 1 mm and directed through the center of the measurement domain, illuminating an axial plane of symmetry in the test bench beginning just above the porous plate. Furthermore, an orange flourescent foil was applied to the portion of the inner wall where the laser sheet impinges upon the rear wall as a beam dump. This results in a shifting of the wavelength of the reflected light to some degree reducing the intensity of the reflections within the pass band of the filter used. Reflections and refractions due to the laser initially entering the measurement domain (the sheet is not infinitely thin) are still present as will be seen in the following, but presented little to no problems for the post-processing. A target with a square grid with lines every 5 mm was inserted into the filled test bench in the measurement plane in order to create a reference image. This image allows for the resolution of the images (7.5 pixels/mm) and the distortion of the image in the radial direction due to the curved acrylic glass–water interface to be obtained. The supply tank was seeded with silver coated hollow glass spheres with a nominal diameter of 15 μm. These particles reflect the laser light and allow for the velocity field to be obtained (see Sec. 3.1.4). The images were recorded at 1500 fps with a pulse delay of 200 μs for each image pair.

Post-processing was conducted with the software PIVview (PivTec GmbH) using standard digital PIV processing techniques (Willert and Gharib, 1991). Iterative multi-grid interrogation was used (Soria, 1996) with a final interrogation window size of 16 x 16 pixels and an overlap of 50%, resulting in roughly one velocity vector calculated for every square millimeter. A mask was used to remove irrelevant data and a background image was produced using the minimum of every pixel over the first 10 images. This background image was then subtracted from all images before calculating the velocity vectors, removing erroneous data resulting from reflections and refractions from the laser on the tube wall. Finally, a Gaussian high-pass filter was used to increase contrast and improve the interrogation technique. The instantaneous velocity components for each image pair were then calculated using the PIVview software. Outliers (vectors differing significantly from their neighboring vectors) were interpolated, although these were very rarely observed for the parameters chosen.

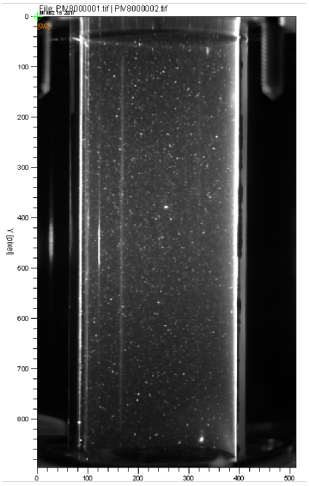

(a) Original image A.

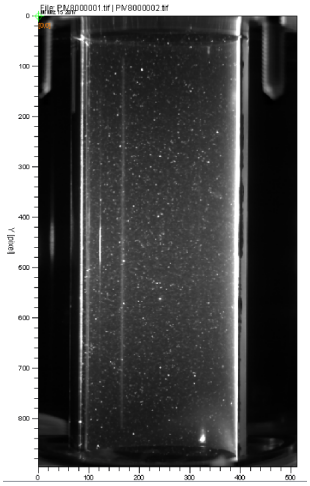

(b) Original image B.

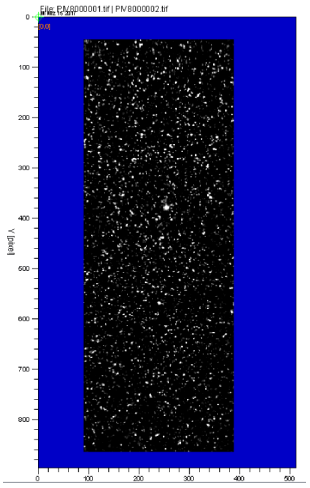

(c) Filtered image with background subtraction and mask. Notice the reduction of reflections and the improved contrast.

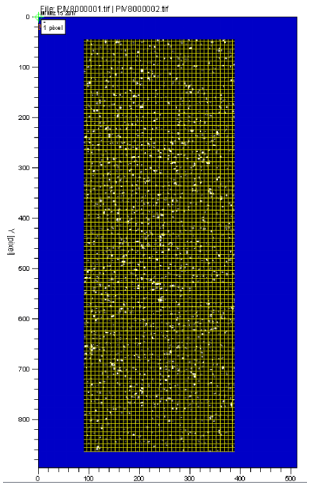

(d) Image with interrogation grid 16 x 16 pixels with 50% overlap.

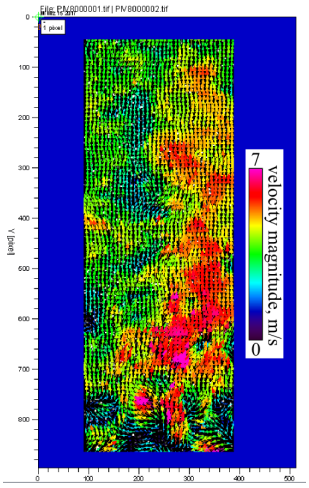

(e) Calculated instantaneous velocity field for image pair A–B.

Figure 3.12: Post-processing of PIV images for a single image pair. The original images are shown in (a) and (b), respectively. Original image A is shown in (c) after application of a mask, background substraction, and filtering. The interrogation grid is shown in (d). The calculated instantaneous velocity field is shown in (e) for the examined image pair.

3.4.1 Reynolds similarity

The Reynolds number, defined as

$$Re = \frac{u_{\text{bulk}} D}{\nu_w}, \tag{3.4}$$

where u_{bulk} is the bulk velocity, D is the tube inner diameter (40 mm), and ν_w is the kinematic viscosity of water ($1.004 \cdot 10^{-6}$ m^2/s), is limited to around 36,000 for this test bench, due to the limitations of the main pump. When this is compared to the same geometry with air at 300 K (kinematic viscosity of $1.568 \cdot 10^{-5}$ m^2/s), the resulting bulk velocity is 14.1 m/s. This corresponds to an air mass flow rate of 76.5 kg/h in a detonation tube of the same inner diameter. As will be shown in Sec. 3.6.4, this is around the middle of the operating range for multi-cycle operation of the modular pulse detonation combustor. However, the situation is made more complicated by the addition of hydrogen and the viscosity for the multi-component gaseous mixtures must be calculated. A simplified model was proposed by Brokaw (1968) based on mean-free-path arguments:

$$\eta_{\text{mix}} = \sum_{i=1}^{N} \frac{X_i \sqrt{\eta_i}}{\frac{\chi_i}{\sqrt{\eta_i}} + \sum_{j=1, j\neq i}^{N} \frac{S_{ij} A_{ij}}{\sqrt{\eta_j}} \chi_j}, \tag{3.5}$$

where η is the respective dynamic viscosity ($\frac{\nu}{\rho}$), N is the number of components in the gas, and χ is the respective molar fraction. S_{ij} is assumed to be 1 for non-polar gases. The factor A_{ij} is a function of the molecular weight ratio of the component gases and is defined as

$$A_{ij} = m_{ij} \left(\frac{M_j}{M_i}\right)^{1/2} \left[1 + \frac{\left(\frac{M_i}{M_j}\right) - \left(\frac{M_i}{M_j}\right)^{0.45}}{2\left(1 + \frac{M_i}{M_j}\right) + \frac{1 + \left(\frac{M_i}{M_j}\right)^{0.45}}{1 + m_{ij}} m_{ij}} \right] \tag{3.6}$$

where m_{ij} is defined as

$$m_{ij} = \left(\frac{4 M_i M_j}{(M_i + M_j)^2} \right)^{1/4}. \tag{3.7}$$

Taking this model into consideration, the dynamic viscosity of the stoichiometric hydrogen–air mixture may be calculated, and by using the molar-averaged density calculated from the density of the component gases, the kinematic viscosity for the gaseous mixture may be determined ($9.247 \cdot 10^{-6}$ m^2/s). This is around 40% less than that of air and has a marked influence on the Reynolds number, resulting in an equivalent bulk velocity of only 8.3 m/s. Taking once again the molar-averaged densities of the gases into consideration, the resulting mass flow rate for air is merely 33.5 kg/h. This is on the low end of the operating range for the combustor as will be shown in Sec. 4.5.4.

3.5 Experimental Test Facility for the PDC

Parallel to preliminary experiments, an entirely new laboratory was designed, built, and equipped for the new modular PDC test bench. The facility is known as the Energy Laboratory and in addition to the room set aside for pressure-gain combustion, in which the pulse detonation test bench is located, accomodation for three other laboratories was accomplished in which combustion experiments dealing with highly-humidified combustion, thermoacoustics, plasma actuation, etc. are conducted. Specifics to this test facility as a whole and specifically those in the pressure-gain facility are described in the following.

3.5.1 Air system

The air supply is delivered by a compressor with a maximum output of 1200 kg/h, providing air at 14 bar. It can also be run in blow-down mode, for a short time at higher flow rates. In the pressure-gain laboratory, the air supply is split into a main supply line, allowing for a maximum mass flow of roughly 600 kg/h, and six secondary supply lines, capable of being used for cooling air or purging flows. The secondary supply lines are each equipped with a rotameter for measuring the volume flow rate and a single pressure regulator upstream of the six lines. The air supply tableau is shown in Fig. 3.13.

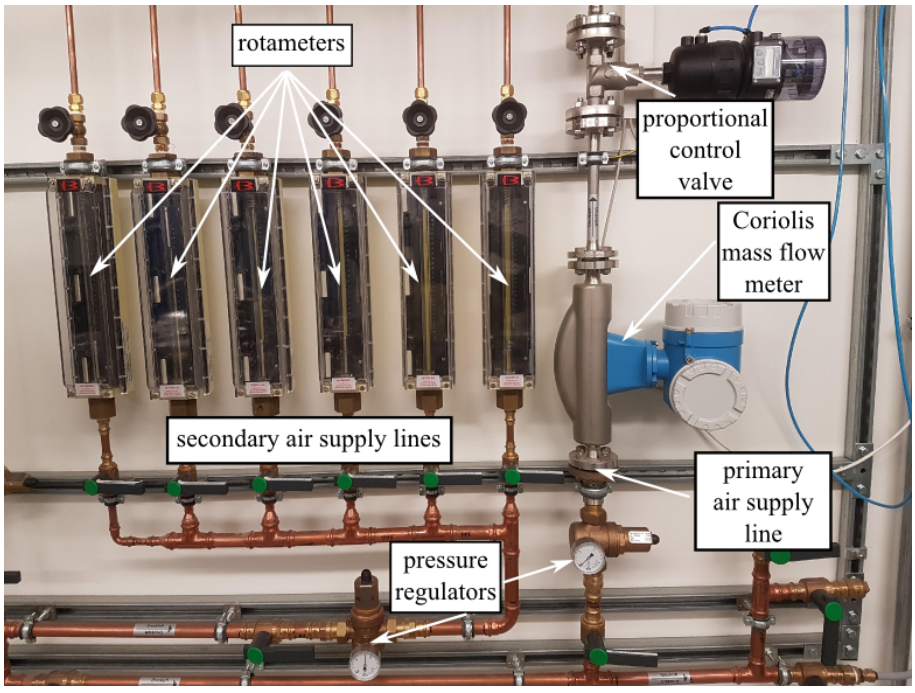

Figure 3.13: Primary and secondary air supply lines with associated measurement and control devices.

The primary air system is also equipped with a pressure regulator followed by an Endress + Hauser Coriolis mass flow meter (Promass F). A pneumatically-operated proportional control valve (Bürkert,

Type 2712) is installed downstream of the mass flow meter. These devices may be operated in tandem with a proportional-integral-derivative (PID) controller implemented within a LabVIEW virtual instrument (VI) in order to achieve a constant mass flow.

3.5.2 Gas system

All laboratories have the capability of creating arbitrary fuel mixtures from a common mixture tableau. This allows, for instance, investigations of syngas variants. Methane, nitrogen, hydrogen, carbon monoxide, and carbon dioxide are available from 300 bar gas cylinders located outside of the building. The gases may be arbitrarily mixed, with each line having a dedicated Coriolis mass flow meter and proportional control valve.

As the combustion of hydrogen is the focus for this thesis, additional attention will be paid to this system. In order to allow for higher flow rates of hydrogen, an additional supply line was added to the mixture tableau without a mass flow meter or a control valve, in order to reduce pressure loss. The gas supply tableau in the pressure-gain combustion laboratory then draws the prepared gas mixture from the mixture tableau. Additionally, a direct nitrogen supply line is available to purge the system after use.

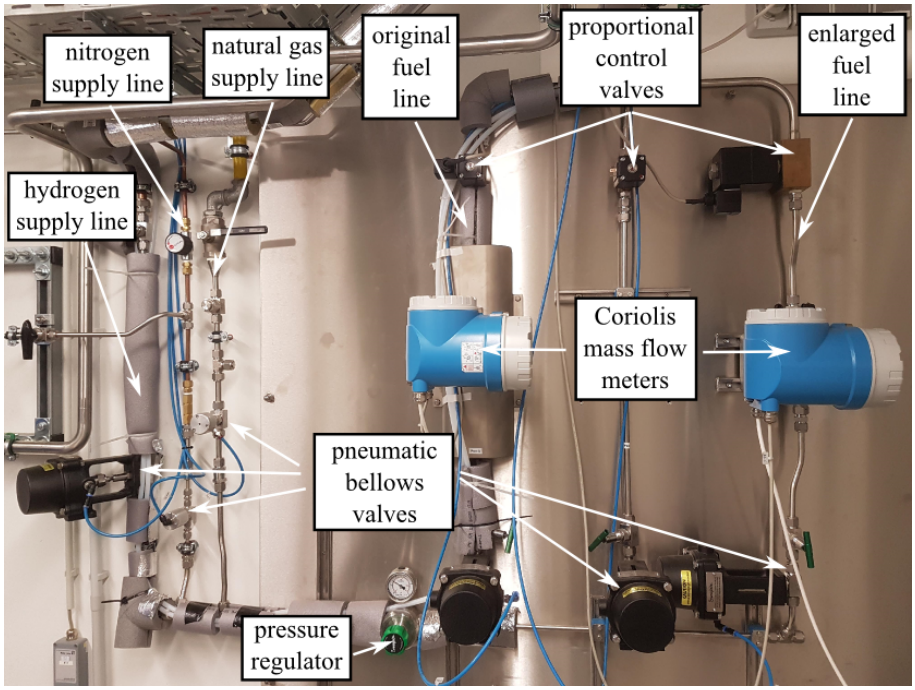

Figure 3.14: Gas supply tableau in the pressure-gain laboratory. In addition to natural gas and methane (for purging), a gas mixture from the mixing tableau may be obtained (here labeled as hydrogen). An additional line was added for multi-cycle operation, shown as enlarged fuel line. A third fuel line, in the middle, is currently not in use.

The gas supply tableau in the laboratory is shown in Fig. 3.14. To date, only pure hydrogen is drawn from the mixing tableau for all PDC experiments. There are three available fuel lines for hydrogen use. The line labeled "original fuel line" contains a Coriolis mass flow meter (Endress + Hauser, Promass A) and a proportional control valve (Bürkert 2875). This line was used for the majority of the single-shot experiments and allows for a mass flow rate of just over 3 kg/h. This proved insufficient for multi-cycle operation and an "enlarged fuel line" was added. Here, a larger tube diameter was installed as well as a larger Coriolis mass flow meter (Endress + Hauser, Cubemass DCI) and proportional control valve (Bürkert 2836). Additionally, several components in the general supply line (e.g., filters, hand valves, etc.) and all bellows valves were replaced in favor of a larger version. Through these enlargements, mass flow rates in excess of 10 kg/h were made possible.

The mass flow rate is controlled by means of Coriolis mass flow meters as well as proportional control valves. As the hydrogen is operating at pulsating conditions, a PID controller is ineffective. Instead, the mass flow rate of the hydrogen is typically metered using steady-state conditions. The proportional control valve is set to obtain the desired mass flow rate over a period of ten seconds, although the filling time for the actual single-shot experiments was limited to one second in order to conserve hydrogen. This method is sufficient for the single-shot tests, as the hydrogen injection valves may be opened long enough for the pressure in the supply line to stabilize. However, it does have implications for multi-cycle operation. These will be discussed in Sec. 3.6.4.

3.5.3 Oxygen system

A supply line for oxygen was also installed in order to allow for the scaling of the cell width by increasing the reactivity of the gas (see Sec. 2.5.2.2). The control was implemented similar to the air system with a PID controller connected to a Coriolis mass flow meter (Endress + Hauser, Promass A) and a proportional control valve (Bürkert 2875). The supply line was also retroactively enlarged for multi-cycle operation with a larger tube diameter as well as a new Coriolis mass flow meter (Endress + Hauser, Promass 80F) and proportional control valve (Bürkert 2712).

3.5.4 Safety provisions

The laboratory is equipped with an exhaust system capable of removing 5000 cubic meters of air per hour, essentially replacing the air in the laboratory roughly every minute. This prevents a flammable mixture of being present in the exhaust system in the case of misfires for mass flow rates of hydrogen up to 18 kg/h. The lower flammability limit for hydrogen–air mixtures is 4% by volume.

A gas warning system is also installed in the laboratory. Flammable gas detectors are installed at the floor and ceiling. The sensor threshold is set to 20% of the lower explosive limit. Additionally, sensors for CO (threshold 30 ppm), NO_2 (threshhold 5 ppm), and oxygen are installed above the test bench. When the threshold of a sensor is reached, warning lights are illuminated and at double the threshold, all bellows valves and control valves in gas and oxygen lines are automatically closed, all air valves are opened to full, and a siren is activated. The CO sensor has the added advantage that it is cross-sensitive

to hydrogen and detects this gas well before the flammable gas detectors. The experiments are operated from a control room separated from the laboratory by several concrete walls. Furthermore, two security cameras are installed that may be continuously monitered on the desktop of the control station. Finally, a nitrogen line is integrated in order to purge the hydrogen and oxygen lines after operation.

3.5.5 Data acquisition

The experiments are operated using two computers, one for the basic control and monitoring of the control valves, bellows valves, Coriolis mass flow meters, and thermocouples. The other computer is used for high-speed applications at 1 MHz. This includes controlling the injection valves and recording the signals from the ionization probes and pressure transducers.

The control and monitoring of the steady-state aspects of the test bench is achieved using a National Instruments data acquistion system (cRIO-9074) and a LabVIEW VI. The VI allows for the mass flows of air and oxygen to be set and maintained using a PID controller. The analog input and output modules are NI-9207 and NI-9264, respectively. Furthermore, temperature at various locations may be observed using K-type thermocouples using a NI-9217 module.

The high-speed control of the periodic PDC cycle is controlled using a different National Instruments data acquisition and control device (MXI-Express NI-9154). The signals for injection valves and ignition are provided over an analog output module (NI-9265) with a temporal resolution of 10 μs (100 kHz). Data acquisition for the pressure transducers and the ionization probes is achieved with several analog input modules (NI-9223) at a higher sampling frequency (1 MHz).

3.6 Modular Pulse Detonation Combustor

The PDC test bench exhibits a valveless, air-breathing design. This means that the air flow is continuous and the gas flow is pulsed using injection valves from the natural gas automobile industry (Bosch NGI2). A standard configuration uses four injectors connected via two valve banks to the test bench (Fig. 3.15). Up to eight injectors may be used with four in each bank. Initiation of the flame was desired at the center of the back plane at the entrance of the combustor and the inlet geometry was designed accordingly. This geometry is shown in Fig. 3.16b. A porous plate is used to separate the mixing chamber and the combustion chamber. As for the experiments in the water test bench, the porosity of the plate–centerbody plane is 44%. The purpose of the inlet is to increase the mixing of fuel and air by increasing the turbulence of the flow, but allowing support to the initial flame propagation (see Sec. 2.8.1). The hydrogen is injected just upstream of the porous plate. In experiments with oxygen enrichment, the oxygen is added to the air well upstream of the inlet plane (roughly 1000 mm) to allow for as homogeneous a mixture as possible.

The modularity of the test bench is ensured by the design of inserts of various lengths of tubes with an inner diameter of 40.3 mm and obstacles using sheath-type connections. The obstacles and tube

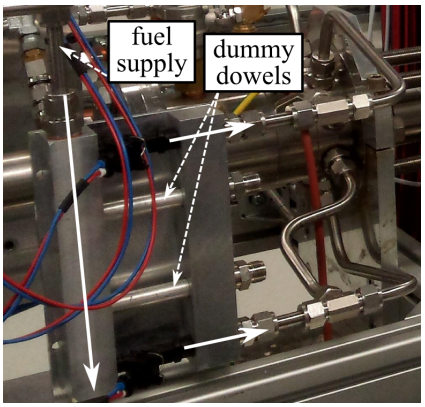

Figure 3.15: Fuel bank for the injection of hydrogen. Two banks are installed, each with the capacity of four injection valves. Unused positions are occupied with aluminum dummy dowels fitted with the same o-rings as the injection valves. The flow direction is indicated by solid white arrows.

inserts are held together using four threaded rods with a diameter of 16 mm. Thus, the number and separation distances of the obstacles is highly variable. The entire test bench is shown in Fig. 3.16a and the connection scheme is shown in Fig. 3.16c. A measurement section with a length of 800 mm is installed downstream of the acceleration section. Here, four pressure transducers (PCB112A05) are installed in order to measure not only the pressure of the reaction waves, but also the wave speed, via the time-of-flight method. All ports are designed for flush-mounting of the pressure transducers and the distances between ports is 200 mm.

3.6.1 Initial design and experiments

Initially, orifice plates were investigated. These were also designed with a blockage ratio of 0.43, as in the previous experiments. Up to eight orifice plates were investigated with separation distances of 85 mm. The first orifice plate was installed at 100 mm from the inlet plane. In the initial studies, single-shot tests were performed. The air flow was set to 68 kg/h and the hydrogen flow, to 2 kg/h (quasi steady-state setting). This corresponds to a stoichiometric hydrogen–air mixture. A fill time of one second was used, after which the injection valves were closed and the ignition spark was simultaneously triggered. The pressure signals were obtained and used via time-of-flight to calculate the propagation speed of the reaction wave. This speed was compared to the known CJ velocity for this mixture (1965 m/s) in order to determine whether or not the configuration successfully produced DDT.

Experiments with oxygen enrichment were conducted at reduced mass flow rates, as the oxygen flow at the time of the investigation was not sufficient. These mass flow rates were 25 kg/h for air, 1.6 kg/h for hydrogen, and 7 kg/h for oxygen. At these mass flows, the air was enriched to 40% oxygen by volume and the mixture was once again stoichiometric. This mixture reproduces a detonation cell width of 2.9 mm, corresponding to the operating conditions of a micro gas turbine, based on the reactivity scaling described in Sec. 2.5.2.2. The same experimental procedure was used as above and the CJ

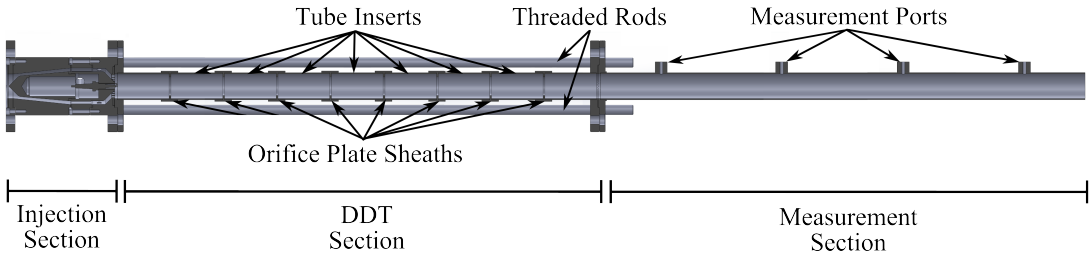

(a) General view of the test bench divided into three sections: the injection section, the DDT section, and the measurement section.

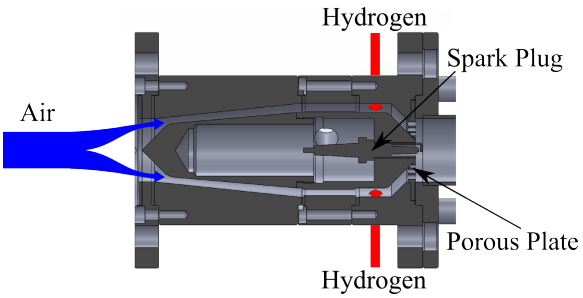

(b) Injection geometry with centerbody and porous plate.

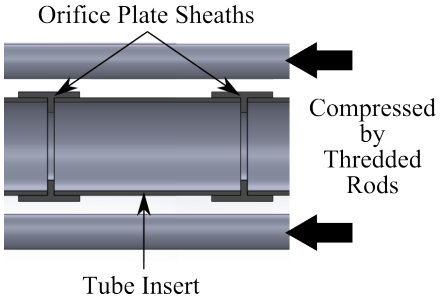

(c) Assembly scheme for orifice plate sheaths and tube inserts

Figure 3.16: Valveless modular pulse detonation combustion test bench. The injection geometry consists of a centerbody in which a spark plug is installed. Hydrogen is injected perpendicular to the air flow just upstream of a porous plate. In the DDT section, a varying number of orifice plate sheaths may be installed with tube inserts of varying lengths. The entire construction is held together with threaded rods. In the measurement section, four ports are available for the flush mounting of piezoelectric pressure transducers or ionization probes.

velocity was once again compared to the calculated value for this mixture (2287 m/s). If successful DDT was obtained consistently, one orifice plate was removed until the transition began to fail.

3.6.2 Shock-focusing geometry

Orifice plates possess several disadvantages for pulse detonation combustor applications. First, they generate recirculation zones directly downstream. In the event of an insufficient purge time, these zones result in the hot exhaust gases being trapped from the previous cycle. When a fresh gas mixture is then injected for the next cycle, these hot gases have the potential of igniting the fresh mixture prematurely. This is known as contact burning and prevents proper operation of the combustor. Second, these same recirculation zones cause additional pressure loss during the filling and purging phases of the cycle, resulting in decreased efficiency. Furthermore, heat transfer to the obstacles during the combustion process can result in an additional decrease in efficiency, which may even outweigh that of the drag. A one-dimensional model implemented by Paxson et al. (2009) indicates a decrease in specific impulse by more than 10% due to obstacles and suggests that the number of required obstacles should be kept to a minimum and the length over which obstacles are installed should be as short as possible.

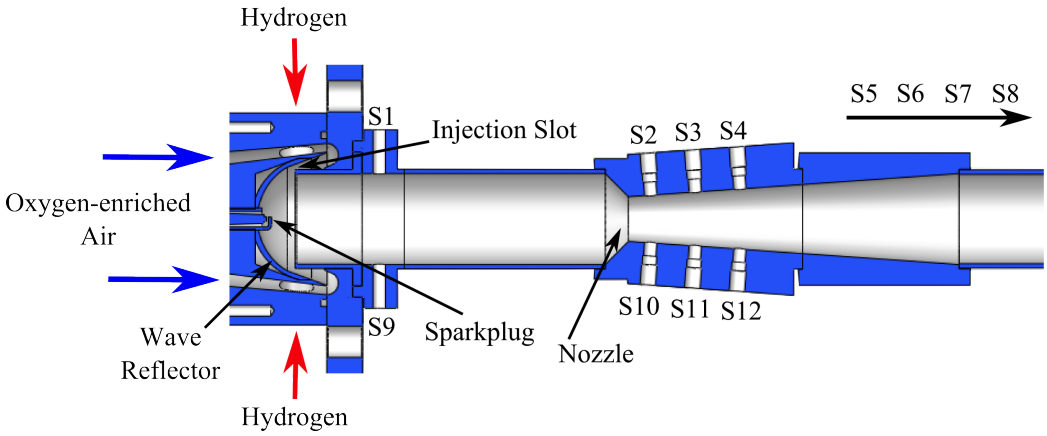

Figure 3.17: Shock focusing geometry used on the modular PDC test bench. Oxygen-enriched air is directed around a centerbody where hydrogen is injected perpendicular to the flow. The resulting gas mixture is then guided through an injection slot with a width of 0.75 mm and into the detonation chamber. A wave reflector is installed at the end of the centerbody where a spark plug is installed. A converging-diverging nozzle with a converging area ratio of 4.0 may be installed at varying locations downstream. Measurement ports are available at twelve different positions: two upstream of the nozzle, six immediately downstream of the nozzle, and four farther downstream in the measurement section.

Several alterations of the test bench were undertaken in order to replace the orifice plates as a means of inducing DDT. First, in an effort to increase the velocity of the initial flame propagating, the injection geometry was altered significantly. The porous plate concept was replaced with one utilizing a hemispherical cavity (referred to in this work as a wave reflector) situated at the end of a larger centerbody (see Fig. 3.17). The mixture flows around the centerbody and is directed through an injection slot with a width of around 0.75 mm. It was found that the exact width of the slot varied slightly based on the seals used and the force applied over the threaded rods, although values between 0.6 mm and 0.8 mm produced consistent results.

This geometry was inspired by the work of Achasov et al. (1997), although the underlying premise and goal is significantly different. Achasov et al. (1997) used a hemispherical focusing body to initiate a detonation in a mixture using the shocks emanating from supersonic jets. In the current configuration, there are no supersonic jets and the purpose is not to directly initiate a detonation. Instead, the wave reflector geometry is designed to act as a fluidic diode and support the initial flame propagation. During the filling process the flow is guided by the curvature upstream of the injection slot and experiences less pressure loss. After an ignition event, the expanding gases behind the flame experience a much higher pressure loss when traveling upstream through the injection slot, inhibiting this effect to some extent. Additionally, pressure waves emanating from the flame that travel upstream impact the wave reflector and the majority are reflected back in the downstream direction. This is not necessarily the case for the perforated plate. The result is that the initial flame propagation is supported by the pressure of the expanding gases and is more quickly accelerated.

The other primary alteration to the test bench was the installation of an axisymmetric, shock-focusing

nozzle (also shown in 3.17). This geometry was simplified from that of Frolov and Aksenov (2009) in that the parabolic contour was substituted in favor of a conical nozzle. The functioning principle is also different as the pressure waves emanating from the flame itself are focused, without the use of a bursting diaphram, which is imperative for the multi-cycle operation of a PDC. The nozzle has a convergent half-angle of 45°, a converging area ratio of 4.0 (throat diameter of 20 mm), and a diverging half-angle of 4°. It was installed at varying distances from the wave reflector.

Flush-mounting measurement ports are incorporated at several positions (also shown in Fig. 3.17): Upstream of the nozzle at 56.7 mm from the center of the wave reflector (S1 & S9), at three axial positions 10 mm, 30 mm, and 50 mm downstream of the throat of the nozzle, respectively (S2–S4 & S10–S12), and in the measurement section farther downstream described in Sec. 3.6.1 (S5–S8). The experimental procedure was identical to that described above with the perforated plate inlet geometry, although the majority of the tests were performed with oxygen-enriched air. Additionally, high-speed imagery was made possible by replacing a section of the tube between the wave reflector and the nozzle with an acrylic glass tube of the same inner diameter with a wall thickness of 20 mm. Images were recorded using a Photron SA-Z high-speed camera.

3.6.3 High-speed shadowgraphy

In order to observe the leading shock wave ahead of the turbulent flame, a detonation chamber was developed in which high-speed shadowgraphy experiments could be conducted. This requires a rectangular cross-section in order to have parallel light in the detonation chamber, which is not possible with a curved geometry. The cross-section of the detonation channel measured 30 mm by 30 mm with the side walls constructed from acrylic glass plates with a thickness of 20 mm. The visualization section has a length of 345 mm, downstream of which the measurement section used in the previous sections is installed. The top and bottom sections in the visualization section are constructed out of aluminum. In these plates, various obstacles could be attached and pressure sensors could be installed. Both gate-type obstacles (such as those used by Teodorczyk et al. (2009)) and ramps were investigated. These obstacles correspond to their axisymmetric equivalents of orifice plates and nozzles. The gate-type obstacles have a blockage ratio of 0.43 and the ramps have a converging area ratio of 4.0 with a convergent half angle of 45° and a divergent half-angle of 4°, also corresponding to the axisymmetric geometries. The visualization section is shown in Fig. 3.18 with a ramp geometry installed. Both inlet geometries (porous plate and wave reflector) could also be installed. The round inlet geometries were retained from the previous studies in order to reduce the fabrication effort. Because of this, a transition section was required to allow for a gradual change from the round cross-section the square cross-section over a length of 27.5 mm. The discontinuity in the cross-section downstream of the visualization section from square back to round is considered irrelevant at this point, as it has little to no effect on the processes to induce DDT upstream.

In addition to investigations in which the injection velocity was varied, experiments were also carried out with initially laminar flames in a quiescent mixture. This was accomplished by sealing the setup with two 40 mm ball valves, one upstream of the inlet and one at the exit of the detonation chamber.

Figure 3.18: Visualization section for the shadowgraphy measurements. In this figure, a ramp geometry is installed with a converging area ratio of 4.0, a convergent half-angle of 45°, and a divergent half-angle of 4°.

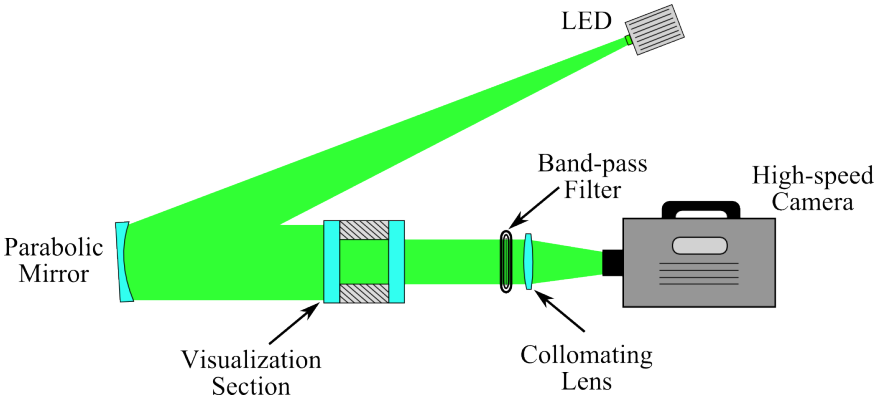

Figure 3.19: Shadowgraphy setup used for the characterization of the leading shock. The setup utilized a V-type configuration with a high-speed LED as a point source, a parabolic mirror to obtain parallel light, a band-pass filter to remove light emission from combustion, and a collimating lens to focus the remaining light into a high-speed camera.

The setup was then evacuated with a vacuum pump. Subsequently, the tube was filled with the desired mixture using the technique of partial pressures back up to a pressure of 1 bar. The mixture was then circulated for a period of five minutes using a pumped circuit connected upstream of the inlet and upstream of the ball valve at the end of the chamber. Afterwards, the ball valve at the exit was slowly opened and the mixture was ignited. The experimental procedure for non-quiescent mixtures was conducted as in all previous experiments on this test bench.

The high-speed shadowgraph setup used for the present work is shown in Fig. 3.19, utilizing a typical v-type configuration. A high-speed, high-intensity green light emitting diode (LED) is used as a point light source (Luminus CBT-120 Series). The control of the system is based on the design of Willert et al. (2012), allowing light pulses in the sub-microsecond domain. The LED was placed at the focal length (1594 mm) of a parabolic mirror with a diameter of 70 mm. The parallel reflected light was then directed from the mirror through the measurement volume. A band-pass filter (532 $\pm$2 nm, half-power bandwidth 20 $\pm$2 nm) was used to filter the majority of the light emission from the combustion. A collimating lens with a focal length of 250 mm and a diameter of 40 mm then focused the image into a high-speed camera (Photron SA-Z).

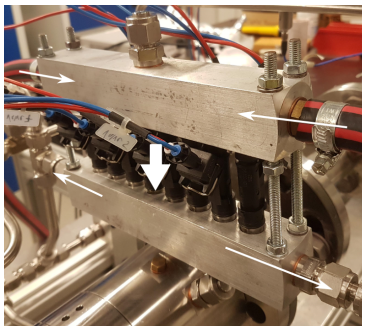

Figure 3.20: Purging element used to purge the fuel lines with air between cycles. Eight injection valves are installed and operated simultaneously. The flow direction is indicated by the white arrows.

3.6.4 Multi-cycle operation

In order to realize multi-cycle operations, several modifications were made to both the infrastructure and the test bench itself, among these being the aforementioned enlargement of the supply lines. Furthermore, a purging element was installed in order to purge the fuel lines leading from the fuel injection banks to the test bench. The purging device is constructed from two aluminum blocks and eight injection valves (also Bosch NGI-2) and is shown in Fig. 3.20. The valves are operated in parallel and the purging air is drawn from the secondary air lines.

One period for multi-cycle operation is composed of several phases. First, the signal is sent to the valves for the injection of hydrogen. A duty cycle of 50% was used for the presented investigations. This means that half of the total cycle period is used for the filling phase. A signal is sent to the ignition circuit to begin charging the coil 5 ms before the end of the filling phase. After 5 ms, the injection valves are closed and the control signal for ignition is set to zero, causing the coil to discharge into the spark plug. Shorter charging times resulted in a weaker spark and more frequent misfires. A period of 5 ms is then allowed for DDT and blown down of the detonation chamber to occur, after which the purging valves are opened to clear the fuel lines of excess hydrogen in preparation for the next cycle. The purging valves are then closed 5 ms before the beginning of the next cycle. An example of the necessary control signals is given in Fig. 3.21 for an operating frequency of 5 Hz at a duty cycle of 50%. Multi-cycle operation was conducted with stoichiometric hydrogen–air mixtures using eight orifice plates and oxygen enrichment using the nozzle. Maximum investigated mass flow rates were 120 kg/h for air, 42 kg/h for oxygen, and 8.8 kg/h for hydrogen.

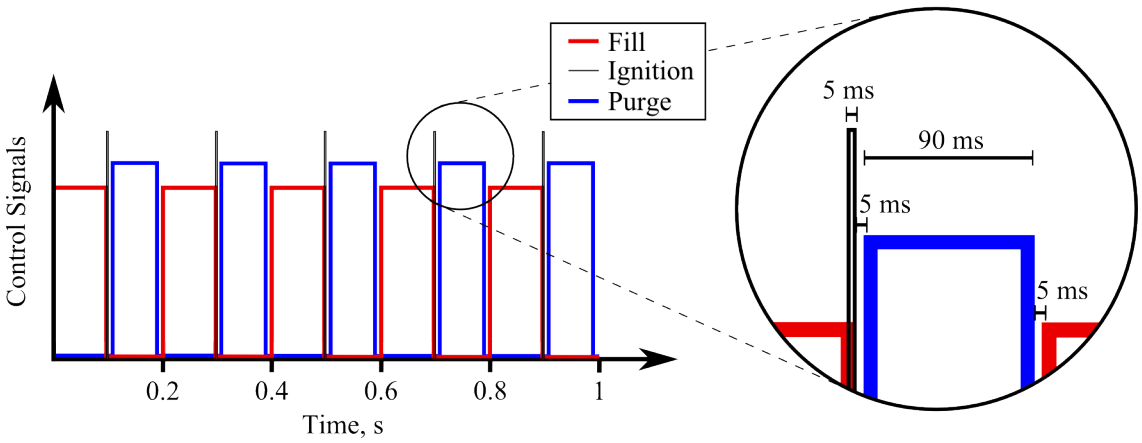

Figure 3.21: Control signals for multi-cycle operation. The operating frequency shown is 5 Hz with a duty cycle of 50%. The amplitude of the signals is arbitrary for the sake of clarity. The real signals exhibited a high value of 5 V.

4 Results and Discussion

In this chapter, the results of the preliminary studies on flame acceleration and DDT are discussed. Furthermore, the operation of the modular pulse detonation test bench in various configurations is examined and an insight into the underlying processes behind the occurrence of DDT using a shock-focusing nozzle is provided. To this end, high-speed imagery and shadowgraphy are utilized. Finally, some aspects of multi-cycle operation for various configurations are presented.

4.1 Results of Initial Flame Acceleration Studies

In this section, the results of the investigations on initial flame acceleration are presented. These tests were conducted on the experimental setup described in Sec. 3.2 using laser sheet tomography. A series of LST images are presented in Fig. 4.1 for Orifice A (left) and Plate A (right). The images were recorded at 16,000 fps and every fifth image is shown ($\Delta t \approx 313\,\mu$s). The recirculation areas formed by the propagating gases ahead of the flame are evident in the first few frames. As the flame (indicated by the dark area) passes the obstacles, it is accelerated. After this acceleration, the flame maintains the same propagation speed throughout the rest of the frames (roughly 100 m/s). The flame acceleration exhibited by Orifice A and Plate A are, thus, roughly comparable. In fact, almost all of the investigated obstacle shapes performed the same or worse with respect to flame acceleration. The flame position based on the point farthest dowstream is plotted in Fig. 4.2 for several geometries. For the purpose of clarity, not all geometries are shown. The geometries with serated edges performed slightly worse compared to the other geometries. Based on these results, it was concluded that the geometry of the obstacles has little influence on flame acceleration, if the blockage ratio is held constant. For this reason, a single obstacle geometry with a blockage ratio of 0.43 was chosen for further experiments. Orifice A was chosen to fill this role, as orifice plates are frequently used in DDT and PDC applications (Guirao et al., 1989; Ciccarelli and Dorofeev, 2008; Frolov, 2014). Furthermore, due to the fact that the orifice plate exhibits the highest surface area contact with the wall of the combustion chamber, heat may be more efficiently transported away from the obstacle, resulting in a lower thermal loading and longer lifetime in the machine without failure when compared to the other geometries investigated in this preliminary study.

The tests conducted with multiple orifice plates were carried out with the goal of determining the optimal spacing between obstacles. First, two orifice plates were investigated. A separation distance of

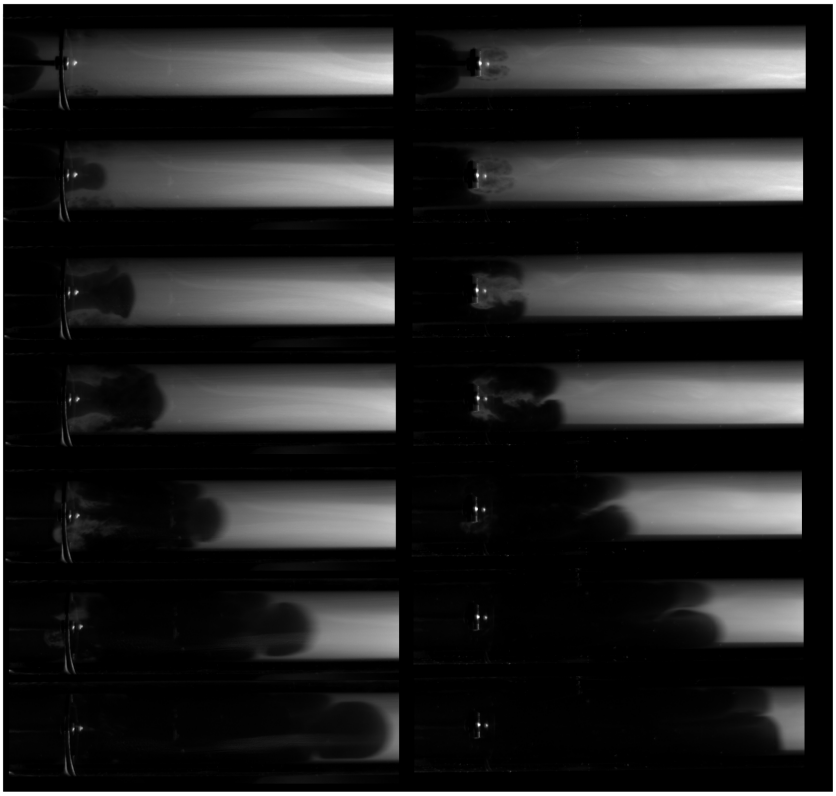

Figure 4.1: Images of a propagating flame around an Orifice A (left) and Plate A (right). The images were recorded at 16,000 fps. Every fifth image is shown, resulting in roughly 313 μs between frames.

75 mm (or 2.5 times the tube inner diameter) proved to result in the highest flame acceleration, resulting in propagation speeds of nearly 300 m/s. For three orifice plates, an initial separation distance of 30 mm resulted in propagation speeds of 260–270 m/s, somewhat less than the optimal spacing for two orifice plates. Increasing this distance to 60 mm resulted in an acceleration to 470 m/s. At larger separation distances, the flame propagation became so fast that it was no longer able to be captured with the high-speed camera used in this setup (Photron SA-1.1). This leads to the conclusion that, at least for this setup, the optimum separation distance between two obstacles is around 2.5 times the inner diameter and somewhat above two tube inner diameters for three obstacles.

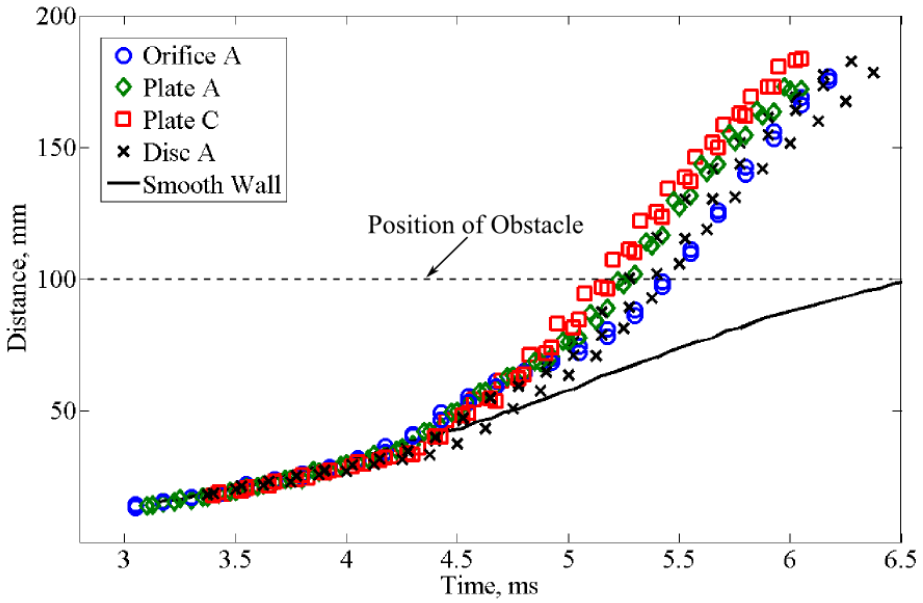

Figure 4.2: Propagation velocities for a hydrogen–air flame obtained using LST in a tube with an inner diameter of 30 mm. The flame acceleration caused by four different obstacles, corresponding to those shown in Fig. 3.6, is plotted and compared to the propagation of the flame in a smooth tube. Blockage ratio of all obstacles was 0.43.

4.2 Results of Preliminary DDT Investigations

These experiments were conducted in order to determine an initial geometry sufficient for producing reliable DDT for later use in the modular pulse detonation combustor (see Sec. 3.6), especially in terms of the number of orifice plates and their optimal separation distance. The tests were conducted with a stoichiometric hydrogen–air mixture and the respective experimental setup is described in Sec. 3.3. In the smallest tube, with an inner diameter of 30 mm, no detonations were observed with up to four orifice plates. In the tube with an inner diameter of 32.5 mm, only one instance of DDT was confirmed. This is not to say that detonations cannot propagate in tubes of these diameters. This is already well known to be the case, as the cell width for this mixture of 7.2 mm is well below the tube inner diameter (Frolov and Gelfand, 1993). This only means that the run-up distance for achieving DDT with the investigated geometry has not been reached within the existing tube length. Unlike cell width, the run-up distance is not only a property of the mixture, but also of the tube size and the geometry and number of the obstacles (Chan et al., 1995). The tube with an inner diameter of 39 mm showed the most promise in terms of reliable DDT. The results of these experiments are shown in Fig. 4.3. The symbols correspond to the average of the highest detected propagation speed from ten ignition events and the distribution bars correspond to the standard deviation of the propagation speed of these events.

Without any obstacles, the flame reached speeds of around 450 m/s within the length of the tube. The addition of one obstacle increased this speed to around 630 m/s. An additional obstacle did not increase

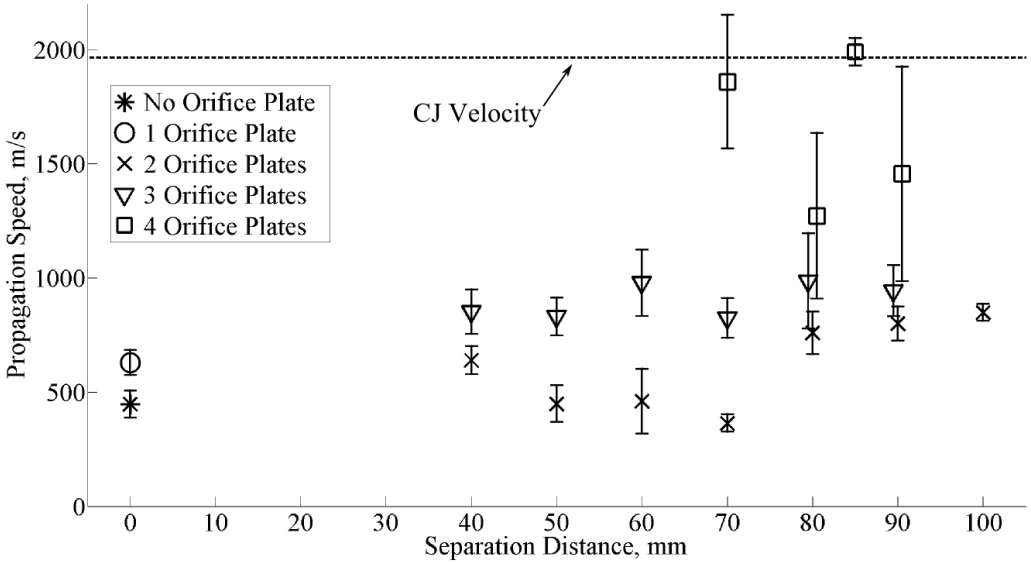

Figure 4.3: Propagation velocity of the reaction front in a stoichiometric hydrogen–air mixture and a tube with an inner diameter of 39 mm for varying number of orifice plates and separation distances. Orifice plates had a blockage ratio of 0.43.

the flame acceleration significantly and, in fact, a decrease in the propagation speed was observed for separation distances of 50–70 mm. This may be due to the reasons cited by Ciccarelli and Dorofeev (2008): If the separation distance is too small, the resulting recirculation zone behind the first obstacle would extend completely to the second obstacle. This prevents the optimal core flow expansion and contraction responsible for the flame folding necessary for initial flame acceleration. At a separation distance of 80 mm, an increase is again seen to a value of around 775 m/s. With three orifice plates, average propagation speeds of 800–1000 m/s were observed; however, only one instance of DDT was observed at a separation distance of 80 mm.

With the addition of a fourth orifice plate, DDT was observed frequently for several separation distances. Here, the propagation velocity was almost always in excess of 1000 m/s. Separation distances of 70, 80, and 90 mm frequently yielded detonations; however, the high variation for the test runs suggested a limiting case. In configurations where DDT occurs, the bars representing the variation may be a bit misleading. This is due to the inherent switching behavior between the occurrence of DDT and no occurrence of DDT. For instance, in the case with a separation distance of 80 mm, DDT occurred in two of the ten test runs with the detonation wave propagating at 1951 m/s and 1937 m/s, respectively. This corresponds nearly to the CJ velocity for this mixture of 1966 m/s. In the other eight test runs, flame propagation velocities varied from 932 m/s to 1250 m/s. The switching behavior between the two modes exacerbates the apparent variation of the configuration. No deflagration propagation velocities were observed between 1250 m/s and 1937 m/s. This also underscores the explanation of Oppenheim et al. (1962) for the onset of detonation, namely, that the deflagration does not accelerate until it merges

with the leading shock, but rather an immediate transition to detonation occurs. This limiting behavior is also underscored by the investigations with three orifice plates. Here, the propagation speed appears less sensitive to the separation distance of the orifices. This speed is around 1000 m/s and corresponds roughly to the speed of sound of the combustion products (1089 m/s). Frequently, this value is simplified to around one half of the CJ velocity and has been shown to be the limiting propagation speed of the deflagration mode of combustion, known as a choked flame (see Sec. 2.7).

A closer investigation at a separation distance of 85 mm resulted in successful DDT in all ten cases. This corresponds to a separation distance of around 2.2 tube diameters. It seems as if separation distances above this value resulted in the other extreme mentioned by Ciccarelli and Dorofeev (2008), namely, that if the spacing is too large, the flame comes into contact with the tube wall and the increase in flame area is suboptimal.

4.3 Results of Experiments on Water Test Bench

Experiments were conducted in a water test bench in order to investigate the flow field for various injection geometries for virtual obstacles. The experimental setup is described in 3.4. As the results of all flow parameter variations are qualitatively similar, focus will be given in this section to variations in the injection geometry and comparisons to the baseline, a standard orifice plate. Therefore, the results presented here are only for a volume flow rate for the main flow of 52.8 L/min, corresponding to a bulk velocity of $U_0 = 0.7$ m/s. As the jet momentum ratio varies greatly for the investigated geometries, comparisons were drawn for test cases also at the same volume flow rates. In fact, the amount of extra flow required for a given process is the parameter most greatly effecting the efficiency in a real machine at any rate. The injected volume flow rate for the virtual obstacles is roughly 7.7 L/min for all cases presented here.

The average axial velocity fields are presented in Fig. 4.4 for the various investigated configurations. These field were obtained by averaging a total of 5000 PIV images pairs. The velocity is normalized by the bulk velocity. The orifice plate results in an acceleration of the flow in the middle of the tube by a factor of two and large areas in the recirculation zone formed behind the orifice plate of very low velocities. This is as to be expected, as a blockage ratio of 0.43 reduces the cross-section by nearly half. The rectangular jets and the round jets result in a similar flow field. However, although the velocity in the middle of the tube is somewhat increased by a factor of around 1.5, it is not as significant as in the case with the orifice plate. Along the walls, the axial velocity exhibits a deficit of only around 20%, indicating little to no recirculation in this domain when compared to the orifice plate. The circumferential jet produces the flow field most similar to the orifice plate. The axial velocity is also not increased as dramatically when compared to the baseline, but is distributed across a larger area of the cross-section. The presence of a small recirculation zone is evident, altough its size and strength are significantly smaller than for the baseline. The fluidic oscillators result in a smoother and more uniform flow with slightly increased axial velocities at the center and slightly decreased velocities along the wall.

A more complete picture of the flow field may be won by considering the turbulent intensities of the investigated test cases. The turbulent intensity is defined as

$$I = \frac{1}{U_0}\sqrt{\frac{U_{\text{rms}} + V_{\text{rms}}}{3}}, \tag{4.1}$$

where U_0 is again the bulk velocity, U_{rms} is the root mean square of the time-dependent axial velocity, and V_{rms}, that of the radial velocity. It is important to note that turbulence is a three-dimensional phenomenon and includes a third component, namely W_{rms}. This is the reason why the average of the root mean square in Eq. 4.1 is taken for three components, although only the contributions of two components are present. In the current configuration, however, this component is considered to be negligible. This is due to the fact that the large coherent structures produced by the orifice plates and injection schemes are expected to be predominantly in the same plane as the measurement plane and not perpendicular to it, which is fortunate, as the experimental setup used did not have the capability of capturing this component. In this situation, the predominant origin of turbulence in the third direction would be indirectly caused by the turbulence in the other two directions.

The turbulence intensity may be understood as the ratio of the fluctuation in the velocity to the bulk velocity. Thus, an intensity of 0.5 corresponds to root-mean-square fluctuations half as large as the mean flow velocity. The turbulence intensity fields for the various configurations are presented in Fig. 4.5. For the case of the orifice plate, the shear layer is depicted very clearly by the high turbulence intensity and the wake is still evident one tube diameter (40 mm) downstream. As with the axial velocity, the turbulence intensity field for the rectangular and round jets do not differ from one another. A much larger area of higher turbulence is apparent in the middle of the tube, where the jets impinge upon one another. This turbulence persists downstream to length of around 50% of the tube diameter. Again, the circumferential jet exhibits the flow field most similar to the orifice plate, however, larger areas of increased turbulence are present and are slightly closer to the wall. There is no impingment at the center of the tube and the turbulence persists to around 50% of the tube diameter downstream, significantly less than the wake for the baseline. The fluidic oscillators appear to distribute the turbulent flow more uniformly in the injection plane and the turbulence decreases fairly monotonically as the flow progresses downstream. The presence of the turbulence does not persist downstream as far as for the other injection geometries and the hypothesis that the fluctuating flow of the fluidic oscillators would increase the turbulence compared to steady-state injection schemes was not substantiated.

In the end, the injection schemes increased the intensity of the turbulent fluctuations as well as the size of the fluctuation domains. Each injection scheme exhibited a spatially different distribution of the turbulence. It remained to be seen how this spatial distribution would affect the occurence of DDT. To this end, a virtual obstacle was developed for use on both the test bench described in Sec. 3.6.1 and that described in Sec. Sec. 3.6.3. However, injection against the pressure rise caused by the propagating turbulent flame proved to be impossible with the available air supply pressure. As a result, no effect was seen on the flame. Furthermore, based on discussions with prominent researchers in the field of detonations at the 9th International Colloquium on Pulsed and Continuous Detonations, where this

work was presented (Gray et al., 2014), it was determined that this scheme would be very unlikely to produce DDT within a reasonable length, due to the absence of shock–obstacle interactions. Based on these two factors, further research in this direction was abandoned.

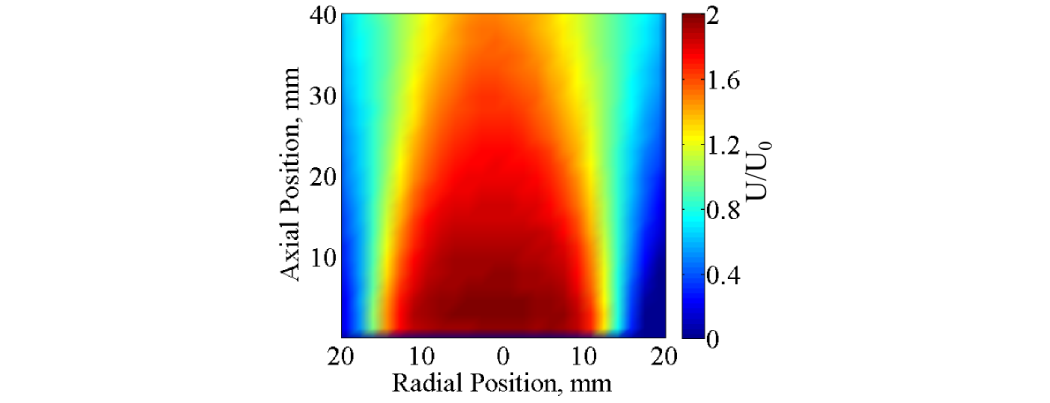

(a) Orifice Plate

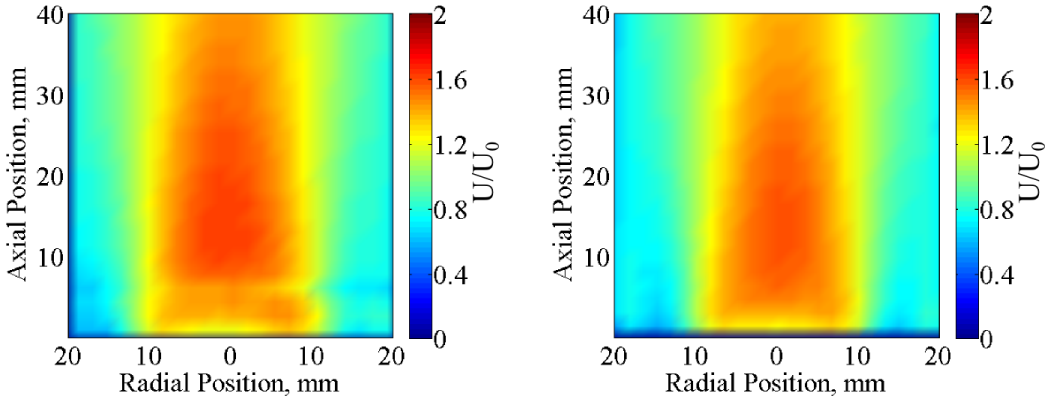

(b) Rectangular Jets

(c) Round Jets

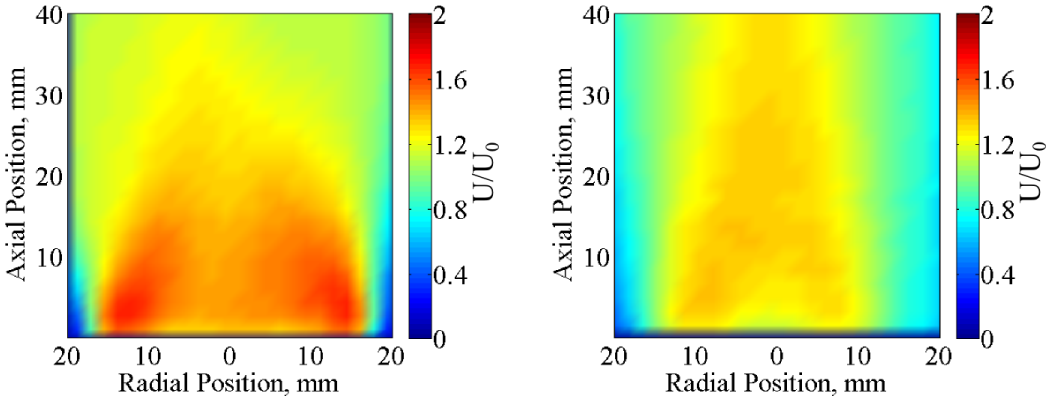

(d) Circumferential Jet

(e) Fluidic Oscillators

Figure 4.4: Average axial velocity fields for various injection geometries of virtual obstacles and a baseline of an orifice plate with a blockage ratio of 0.43. The average was calculated from 5000 images obtained at a framerate of 1500 fps. The bulk velocity U_0 is 0.7 m/s and the tube inner diameter is 40 mm.

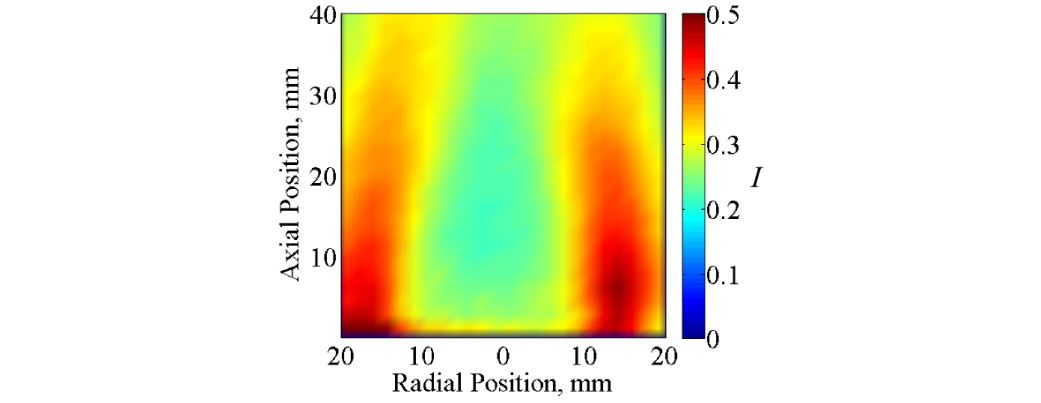

(a) Orifice Plate

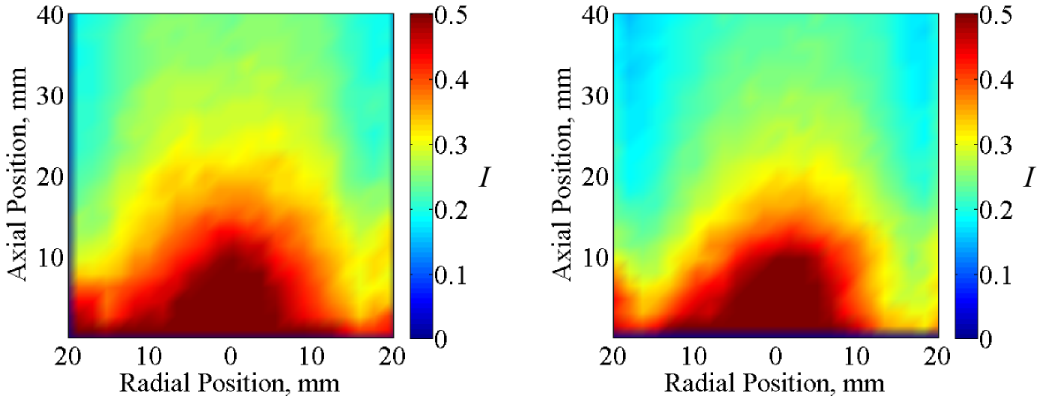

(b) Rectangular Jets

(c) Round Jets

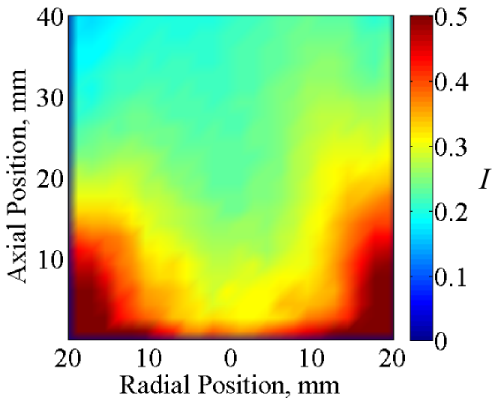

(d) Circumferential Jet

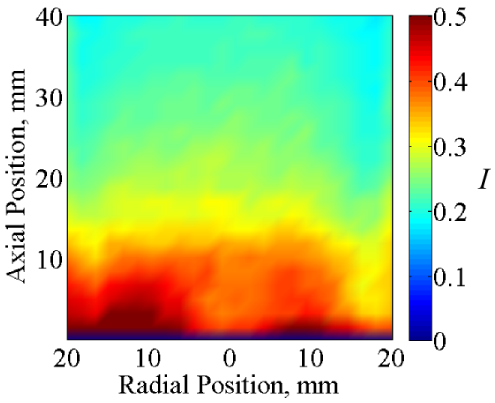

(e) Fluidic Oscillators

Figure 4.5: Turbulence intensity fields for various injection geometries of virtual obstacles and a baseline of an orifice plate with a blockage ratio of 0.43. The turbulence intensity is calculated from Eq. 4.1 with a bulk velocity U_0 of 0.7 m/s. The tube inner diameter is 40 mm.

4.4 Intermediate Conclusions

Initial investigations on the effect of the geometry of a single obstacle on the acceleration of a stoichiometric hydrogen–air flame were conducted using LST. The results indicated that geometry plays only a secondary role when the blockage ratio of the obstacles is held constant. For this reason, orifice plates were chosen as the obstacle geometry of choice for the subsequent preliminary studies, due in part to their frequent use in other cited DDT and PDC investigations. Other benefits of orifice plates include their simplicity and maximum contact surface with the outer wall (to ease in cooling). Investigations for up to three orifice plates indicated that separation distances of 2–2.5 times the tube diameter resulted in the highest flame acceleration.

During investigations of the same mixture on the DDT test bench, it was determined that DDT occurred only in the tube with the largest inner diameter (39 mm) and that three orifice plates were not sufficient for generating DDT within this tube. With the introduction of a fourth orifice plate, sporadic DDT events were observed for several separation distances, where a switching behavior between choked deflagration and detonation was frequently observed. At separation distances of around 2.1–2.2 times the tube diameter, DDT events became very repeatable.

Although non-reacting investigations indicated that turbulence fields and levels of turbulence intensity similar to those created by an orifice plate could be achieved, reacting experiments could not reproduce the injection due to pressure from the propagating turbulent flame. The realizations reached during the preliminary studies influenced many decisions and determined the path of design and development for the modular pulse detonation test bench. Parameters taken from these studies to be used for the design of the modular pulse detonation test bench, were a tube diameter of at least 40 mm, at least four orifice plates exhibiting a blockage ratio of 0.43, and a separation distance between the orifice plates of 85 mm. The results obtained on the new test bench using these parameters as a starting point will be discussed in the following.

4.5 Modular PDC: Results and Discussion

In the following, the results for the investigations on the modular pulse detonation combustion test bench will be presented. The general iterative procedure of testing, analysis, and modification will presented to the best of the authors ability, although it must be noted that many decisions, changes, initial mistakes, and subsequent realizations must be omitted for the sake of comprehension and cohesion in the scope of this work. A road map has been humbly prepared for the reader, which may diverge from the chronological course of events in order to present these developments more clearly.

4.5.1 Some comments on the pressure transducers

In Sec. 3.1.2, the working principle behind piezoelectric pressure transducers was introduced and some drawbacks, such as thermal shock, were discussed. Before discussing the results dealing with these

pressure measurements, it may be prudent to touch on a few more characteristics of these sensors so that the reader may interpret the signals and what they represent more accurately. As mentioned in Sec. 3.6, the pressure sensors used in these studies were the model PCB112A05. The resonant frequency of these sensors is $\geq$ 200 kHz. One unit of a new model series (PCB113B03), with a resonant frequency of $\geq$ 500 kHz was made available by the manufacturer for testing. A comparison between these two pressure transducers is presented in Fig 4.6a for a given detonation wave in a stoichiometric, oxygen-enriched mixutre. Examining these signals, it is immediately apparent that the 113B03 sensor does not suffer as extremely from thermal shock as the 112A05 sensor, although non-physical pressures of around -2 bar are still observed. Looking at the inset in the figure, the influence of the increased resonance frequency is shown by the decreased fluctuations behind the pressure peak. This is an important aspect for the investigation of shock and detonation waves because of the high rate of change in pressure. These signals may be idealized as a type of delta function for the frequencies relevant to the mechano-structural properties of the sensor, essentially exciting those above its resonance frequency and inducing the "ringing" made evident by the fluctuations after the peak. This makes the interpretation of pressure signals after this peak difficult to impossible. The rise time of both sensors is more than sufficient to capture the pressure rise, but the PCB112A sensor registers a higher pressure. This higher pressure is part of the von Neumann (VN) pressure peak, which is not resolved by the PCB113B03 sensor. This aspect will be discussed in further detail in Sec. 4.5.2.

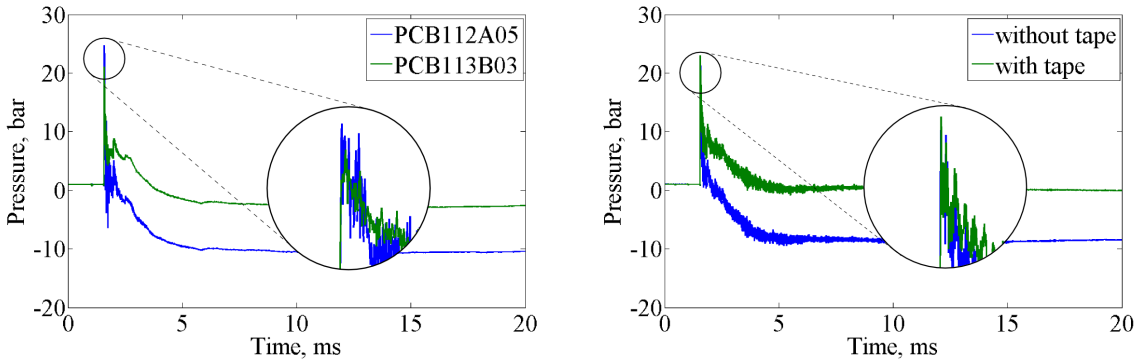

(a) Comparison between the performance of PCB models 112A05 and 113B03.

(b) The effect of thermal shock with and without insulation tape.

Figure 4.6: Comparitive studies investigating several properties of piezoelectric pressure transducers for the measurement of detonation waves.

In order to reduce the effect of thermal shock on the pressure transducers, a thin (0.13 mm) polyvinyl chloride (PVC) tape was cut to the diameter of the sensor membrane and applied to the end of the sensor. This tape is essentially electrical insulation tape and its benefits were shown to decrease the effects of thermal shock due to detonation waves by Janka (2014). A comparison of signals obtained with the PCB112A05 sensors with and without the tape is plotted in Fig. 4.6b. It cannot be determined to what extent the thermal shock is mitigated, but the effect is significant, already evident after a fraction of a millisecond. At the very least, no non-physical pressure are recorded. This benefit comes with no

damping of the initial pressure peak, although this is difficult to discern from the inset of the figure. One drawback of the insulation tape is that it is only suitable for a limited number of test runs. In some cases, it is removed or somewhat melted after a single detonation event. The environment of the detonation wave is very harsh and observing the tape after a detonation event reveals that the triple point of the detonation cells may actually slice through the tape (shown in Fig. 4.7). Therefore, multi-cycle applications, or even quick single-shot campaigns without disassembly of the test bench, are not possible with this method.

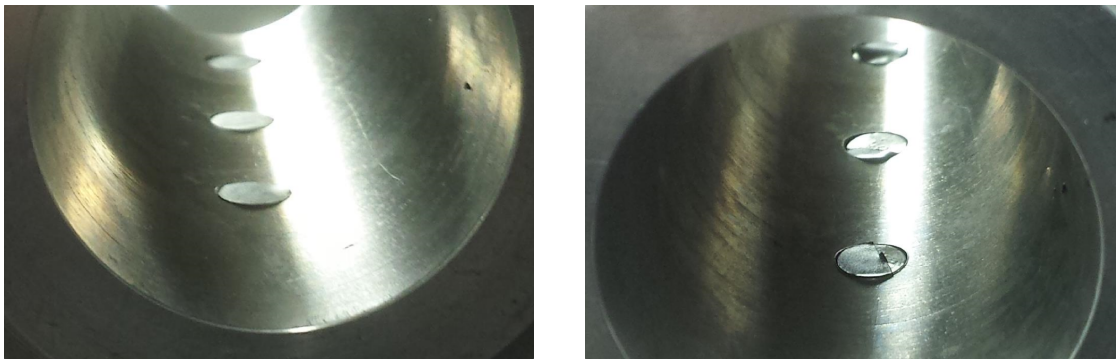

(a) Before detonation event. **(b)** After detonation event.

Figure 4.7: Insulation tape over the membrane of the piezoelectric pressure transducers before and after a detonation event. Notice the clean cut caused by the triple point of the detonation cells and removal of one side of the tape on each of the three sensors.

4.5.2 Investigations with gate-type obstacles and orifice plates

High-speed shadowgraphy was used to investigate the initial flame acceleration caused by a single gate-type obstacle with varying injection velocities. These results are shown in Fig. 4.8 for bulk injection velocities of 0 m/s, 2.7 m/s, 5.4 m/s, and 8.2 m/s using the porous plate inlet geometry described in Sec. 3.6.

In the quiescent mixture, an initially laminar flame results. As the flame travels through the obstacle, it is accelerated not only due to reduced cross-section, but also due to flame folding and turbulence created in the shear layer made evident by the vortices seen in Fig 4.8. The maximum propagation velocity is around 180 m/s. As the bulk injection velocity is increased to 2.7 m/s, 5.4 m/s, and 8.2 m/s, the flame immediately becomes turbulent and the maximum propagation velocity increases to 260 m/s, 280 m/s, and 340 m/s, respectively. These are very modest injection velocities compared to those present in a pulse detonation combustor operating even at frequencies of around 10 Hz. Nevertheless, the resulting increase in flame acceleration due to the added turbulence is evident and establishes a strong link between these two parameters.

Based on the preliminary investigations on the DDT test bench (see Sec. 4.2) four orifice plates were deemed sufficient for obtaining reliable DDT. This was quickly proven to not be the case on the modular

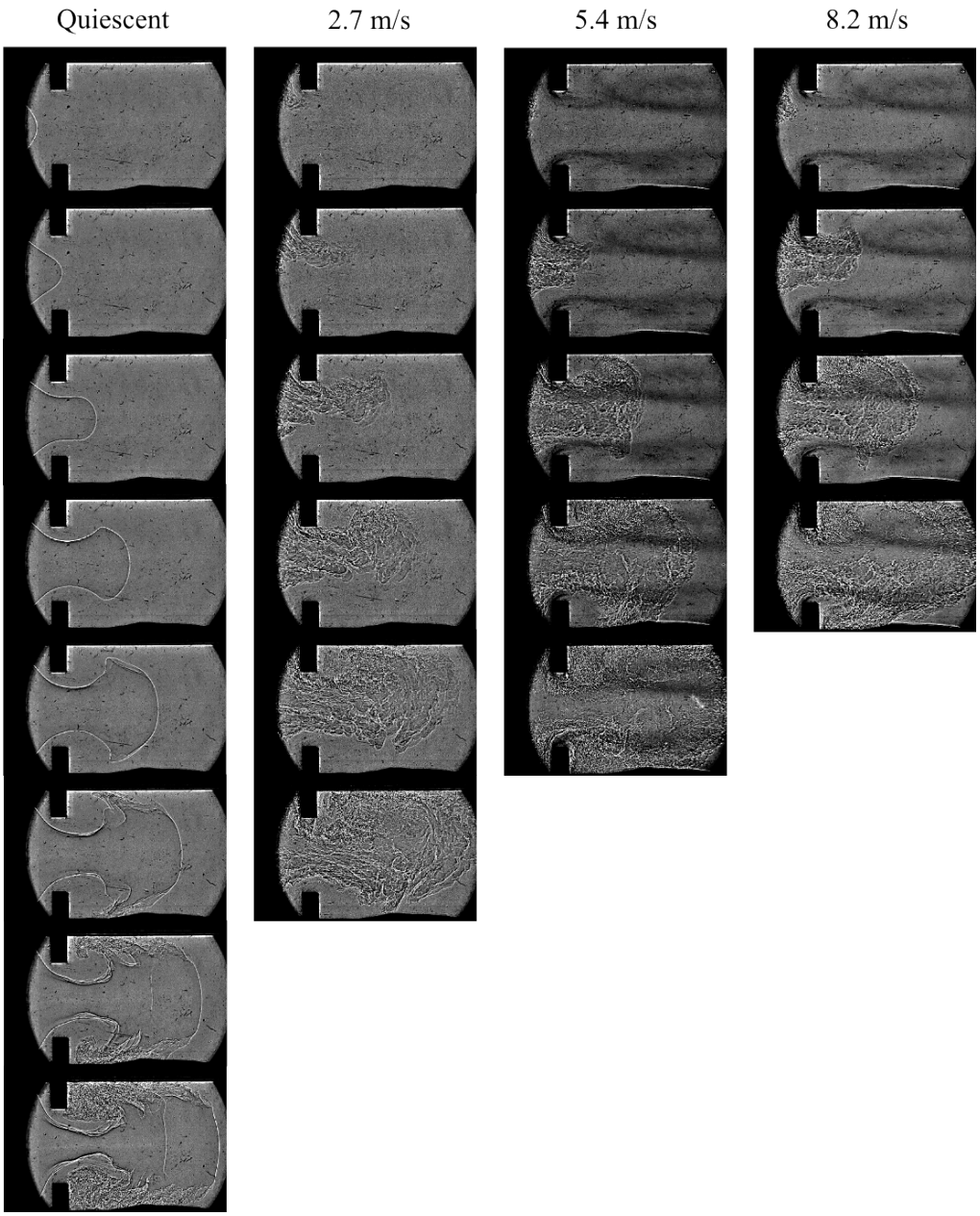

Figure 4.8: High-speed shadowgraphy images of hydrogen–air flames propagating through a gate-type obstacle with a blockage ration of 0.43. Images were obtained at 30 kHz with an exposure time of 1 μs. The bulk injection velocity of the fresh gas mixture varies from left to right, starting with a quiescent mixture. The increased turbulence resulting from the increased injection velocity results in higher initial flame acceleration.

PDC test bench and was found to be due to the valveless design of the new setup. On the previous test bench, the initial flames essentially propagated away from a closed end. Although the supply lines in the previous test bench provided a small volume for the expanding gases to escape, even these were closed by valves after some length. This allowed for pressure to increase more drastically behind the flame, supporting and driving its initial acceleration. The valveless design of the modular PDC, however, was necessary for a simplified apparatus capable of multi-cycle operation at a later time.

Increasing the number of orifice plates incrementally and using the same separation distances resulted in a total of eight orifice plates being installed before DDT was obtained reliably. The confirmation of DDT was determined by obtaining the time-of-flight of the reaction wave using the pressure transducers. An example is given in Fig. 4.9a. The pressure peaks at all four sensors in the measurement section register pressures in excess of the CJ pressure of 15.8 bar. This is because the pressure sensors register some of the VN pressure (28.7 bar), as mentioned earlier. However, due to the fact that the pressure is integrated over the entire transducer membrane and the induction length is much smaller than the width of the membrane, this pressure is somewhat reduced. This is also due in part to the sampling frequency of the sensor, as the time scales of the induction zone are small enough to play a role. Observing the time of flight, a value of 0.098 ms is obtained. The propagation velocity remains very stable along the length of the tube, with variations in time of flight of $\pm 1\ \mu$s (the temporal resolution of the data acquisition system). The corresponding velocity is 2040 m/s, near but slightly above the CJ velocity for this mixture of 1966 m/s. The sampling rate results in an uncertainty of ± 21 m/s.

Installing the wave reflector inlet allowed for a reduction of the necessary number of orifice plates to six for the stoichiometric hydrogen–air mixture. The success of the wave reflector is based on two important factors. First, the thin injection slot has a surface area of 7.5% of the cross-sectional area of the tube, resulting in an injection velocity in this region of more than one order of magnitude higher than the bulk velocity in the tube during the filling phase prior to ignition. This results in a jet-like flow with much higher levels of turbulence which, in turn, leads to a higher initial turbulent flame speed. The second factor is the diode-like characteristic of this geometry, inhibiting flow upstream during the expansion of the propagating flame, increasing the pressure available to support the flame propagation through expanding exhaust gases (see Sec. 2.8.1).

Using oxygen enrichment to increase the reactivity of the reactants to that of the combustion inlet operating conditions of a micro gas turbine (401 K, 3 bar) resulted in a reduction to three orifice plates with a separation distance of 85 mm using the wave reflector. If the separation distance was increased to 120 mm, reliable DDT could be produced using just two orifice plates. It is important to note that this does not, in fact, contradict the previous statement that 85 mm is the optimum spacing for flame acceleration. The processes of flame acceleration and DDT, although inherently tied together, are two different phenomena. It is possible for DDT to occur downstream of the last obstacle, in which case, it also serves to accelerate the flame. More often than not, however, the last obstacle serves as a platform for shock–obstacle interaction and the means for detonation transition, decoupling it from the flame acceleration process.

An example of the pressure plots used to verify the reaction wave velocity using the time-of-flight

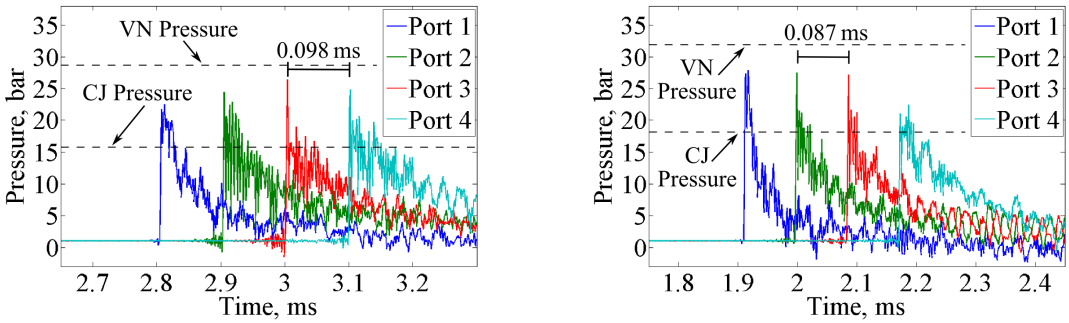

(a) Detonation in stoichoimetric hydrogen–air mixture. Here, eight orifice plates are necessary for DDT. CJ pressure is 15.8 bar, von Neumann pressure is 28.7 bar, and CJ velocity is 1966 m/s.

(b) Detonation in a stoichoimetric mixture and oxygen-enriched air (40%-vol.). Here, three orifice plates are necessary for DDT. CJ pressure is 18.1 bar, von Neumann pressure is 31.9 bar, and CJ velocity is 2287.5 m/s.

Figure 4.9: Pressure measurements from a single CJ detonation obtained by four piezoelectric pressure transducers downstream of multiple orifice plates with a blockage ratio of 0.43 and a separation distance of 85 mm. Note the pressure value falling between the CJ pressure and the VN pressure due to the sampling rate of the sensor and the relatively small size of the von Neumann peak with respect to the sensor membrance.

method is shown in Fig. 4.9b. Notice the higher values of CJ pressure (18.1 bar) and VN pressure (31.9 bar) for this mixture when compared to Fig. 4.9a. Also, a very stable time of flight of 0.087 ms is obtained. This would correspond to a propagation velocity of 2299 m/s, which is very close to the theoretical value for this mixture at 2287.5 m/s. In fact, at this propagation velocity and sampling frequency, the velocity is within the somewhat higher measurement uncertainty of ± 27 m/s.

4.5.3 Investigations with the shock-focusing nozzle

The geometry of the shock-focusing nozzle is described in Sec. 3.6.2. The length of the tube was increased incrementally until DDT could be repeatedly obtained. At a distance of 158 mm, measured from the plane of the spark plug to the beginning of the convergence of the nozzle, the conditions were met for reliably producing DDT. The resulting distances of the pressure tranducers based on this length are summarized in Table 4.1. A series of 100 ignition events confirmed a success rate of 98% with a combination of the wave reflector and the shock-focusing nozzle.

By examining the pressure evolution at various positions in the detonation chamber, it is possible to examine the physics occurring in the chamber and attempt to explain them. These pressures are plotted for several positions in Fig. 4.10. The positions correspond to those shown in Fig. 3.17. The extremely high pressure of 57.5 bar in the first sensor 10 mm downstream of the throat of the nozzle (S2) is immediately evident. This pressure is well above the VN pressure of 32 bar and may only correspond to the blast wave of an over-driven detonation originating from a local explosion. This peak varied greatly in intensity, sometimes in excess of 70 bar, but was always above the VN pressure and almost

Table 4.1: Distances of pressure sensors from the center of the wave reflector.

Pressure Sensor	Distance (mm)
S1 & S9	56.7
S2 & S10	178.3
S3 & S11	198.3
S4 & S12	218.3
S5	495
S6	695
S7	895
S8	1,095

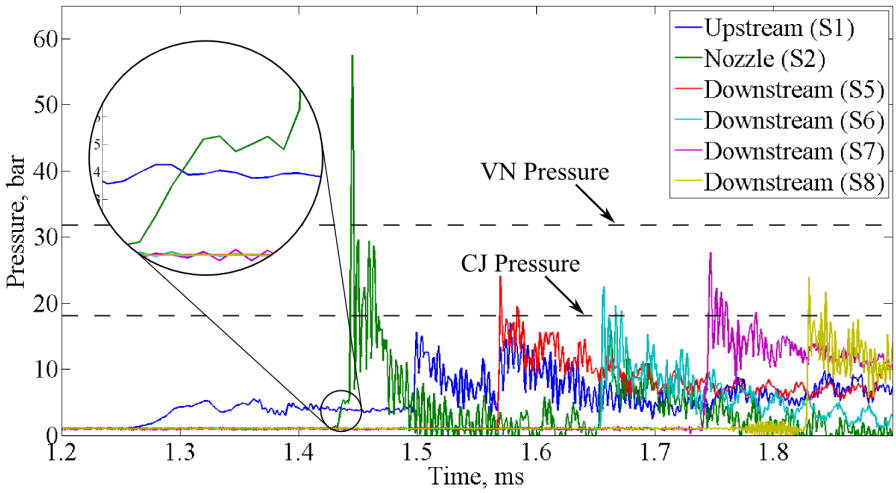

Figure 4.10: Pressure measurements for the DDT process occurring near a shock-focusing nozzle. A large peak from the local explosion is registered just downstream of the throat of the nozzle preceded by a leading shock of around 5 bar. Farther downstream a CJ detonation is observed at sensors S5–S8.

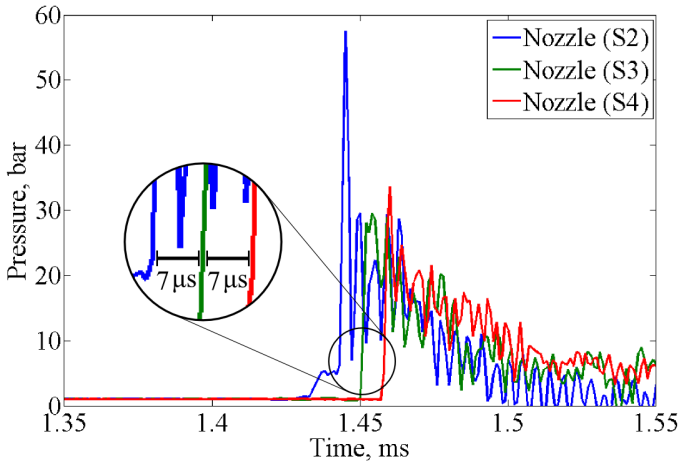

Figure 4.11: Pressure signals of an overdriven detonation obtained downstream of the throat of the shock-focusing nozzle. Time-of-flight indicates propagation velocities of over 2,800 m/s (7 μs at a separation distance of 20 mm). The higher pressure on the order of the VN pressure verify this observation.

always in excess of 40 bar. Although this peak is very short lived and subject to the same variations as the VN peak, due to the limited sampling frequency and the relatively large size of the sensor membrane with respect to the blast wave. Another aspect of this signal is the small pressure increase of around 5 bar just before the arrival of the detonation wave. This is due to the leading shock wave ahead of the turbulent flame and varies in intensity from just over 4 bar to just under 8 bar between test cases. After seeing this effect, the data with the orifice plates were reexamined and a handfull of DDT events showed this behavior, meaning that the DDT did not occur in these cases near the orifice plate, but rather downstream in the vicinity of the pressure sensor. Additionally examining the other two pressure signals just downstream of the throat of the nozzle indicates that an overdriven detonation is present here with a velocity of over 2,800 m/s. Even with a measurement uncertainty of over $\pm$400 m/s, due to the small distance between measurement positions (20 mm), this is well above the CJ velocity. The presence of an overdriven detonation can also be confirmed by the higher pressure peaks on the order of the VN pressure, which as was shown above, is not normally able to be resolved.

The pressure rise upstream of the nozzle (S1) is caused by the expanding gases in the turbulent flame. This pressure reaches a value of around 4 bar and exhibits fluctuations at around 3 kHz. These fluctuations are present in many, but not all, test cases. They may be due to the complex interactions between the pressure waves emanating from the flame and reflections from the wave reflector, the nozzle and the walls of the tube. The upstream propagating shock wave can be seen at around 1.5 ms and its reflection from the wave reflector at 1.57 ms. As the peaks are relatively similar in intensity, it may be assumed that the shock speed does not vary signigficantly during the propagation or reflection processes. This would put its velocity at around 1620 m/s. The downstream pressure signals (S5–S8), indicate a steady-state CJ detonation traveling at the CJ velocity and registered peaks between the CJ pressure and the VN pressure.

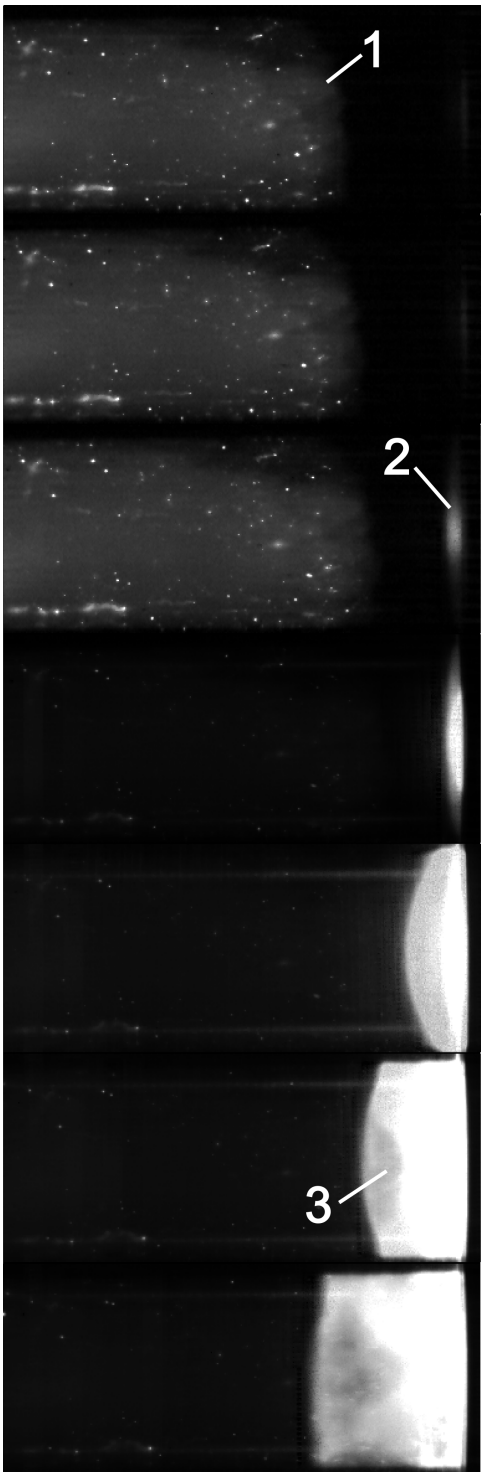

Figure 4.12: High-speed images of DDT in the shock-focusing nozzle taken at 200,000 fps. The nozzle itself is out of frame to the right of the images. The brightness of the first three images is increased by a factor of six in order to see the turbulent flame (1) more clearly, which travels from left to right at a velocity of 660 m/s. The ensuing detonation is seen downstream of the flame (2) and the shock wave travels into the burnt gases (3) at a velocity of 1,580 m/s. This detonation continues in the other direction into the measurement section downstream.

Examining the high-speed images obtained in the acrylic glass section of the tube upstream of the shock-focusing nozzle provides more insight into the processes occurring in the detonation chamber. The images from one test run are presented in Fig. 4.12. These images were obtained at a frame rate of 200,000 fps (5 μs between frames). In the first three frames the comparatively slow propagation of the turbulent flame can be seen, denoted by (1). The velocity calculated by the frame to frame displacement is around 660 m/s. This is much lower than the velocity recorded prior to DDT using obstacles that rely on turbulating effects and shock–obstacle interaction, such as orifice plates. This velocity is typically at least the speed of sound in the combustion products (around half of the CJ velocity) (Peraldi et al., 1986). In the considered mixture, this criterion would be around 1000 m/s. In the third frame, the detonation can be seen exiting the nozzle and traveling upstream clearly before the flame has reached this position, denoted by (2). After reaching the flame, the remaining shock wave travels into the burnt mixture at a velocity of around 1,580 m/s. This agrees very well with the signal S1 shown in Fig. 4.10. In the final two images, an interface can clearly be seen between the gases reacted by the turbulent flame and those reacted by the detonation wave, denoted by (3).

Analyzing the high-speed shadowgraphy images obtained on the test bench with a square cross-section provides even more details to the complex process behind the shock focusing. The test bench is described in Sec. 3.6.3. Other than the geometry, all parameters are kept the same as with the previously described results, including oxygen enrichment. The influence of geometry, however, is not trivial. This will be discussed after the examination of the data. A series of images is presented in Fig. 4.13. The images were taken at a framerate of 100,000 fps (10 μs between frames). The distance of the ramp from the wave reflector for the presented images is related to the optimal distance of the axisymmetric nozzle from the wave reflector by matching the volume between the two geometries and the wave reflector, respectively.

In the first frame, the incident shock wave is visible. This shock travels at a velocity of 1,120 m/s. Assuming atmospheric initial conditions, this corresponds to a Mach number of 2.53, resulting in a pressure increase of 7.3 bar which falls within the previously determined range of variability observed for the leading shock. In the second frame, the reflections of the shock wave are seen, which propagate through the third and fourth frame with a velocity of 342 m/s, where they interact with one another. Due to the precompression from the first shock, the second shock travels with an increased speed through the medium already at the higher temperature and pressure, due to the higher speed of sound. This may be observed in the fifth frame, where each reflected shock is separated into two fronts, one traveling into the upstream gases and one traveling into the doubly compressed gas near the ramp. The velocity of the faster shock wave is 481 m/s. These velocities may be compared to those obtained in Sec. 2.8.4, as the incident shock velocity in this example has been, "coincidentally," very aptly chosen. Comparison reveals that the reflected shock waves exhibit a deficit of around 33% from the calculated value, the deviation of which may come from several sources.

The most significant is the fact that neither the axisymmetric nozzle geometry nor the geometry with the two ramps is equivalent to the v-shaped endwall. The divergence in the cross-section after the throat creates an expansion wave, which travels back upstream weakening the reflected shock wave. Another source of divergence is due to curvature effects, which were not taken into account in the analytical example. The incident shock wave impacts different positions along the converging surface at different points in time and the reflection velocity differs from the incident velocity. The result is a curved reflected shock as seen in Fig. 4.13, resulting in a lower pressure increase as the radius of curvature increases. Finally, losses due to friction, vortex generation, and non-ideal reflection coefficients are also not taken in to account. These effects combined result in a pressure increase in the focussing region less than that calculated analytically. In fact, most of the test runs conducted using the square cross-section did not exhibit DDT within the visualization section and transition occurred farther downstream.

One last aspect that must be mentioned when discussing the shock-focusing nozzle is that successful DDT was not possible when using the previous porous plate geometry. This is likely due to two factors. First, the level of turbulence created by the plate is probably less than that created by the thin injection slot. This was unfortunately not investigated, but a simple isothermal measurement campaign using hot-wire anemometry would allow this to be properly characterized. Second, the diode-like quality of

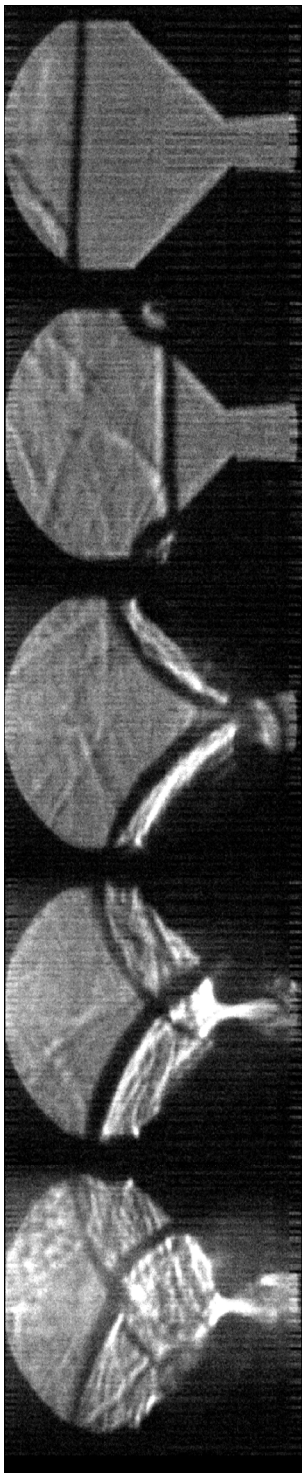

Figure 4.13: High-speed shadowgraphy images of the leading shock ahead of a turbulent flame being focused by two 45° ramps installed at the top and bottom of a 30 mm by 30 mm channel. The shock wave travels from left to right, impinges on the ramps, and is reflected back upstream, increasing the pressure and temperature of the unburnt gas ahead of the turbulent flame. Images taken at 100,000 fps.

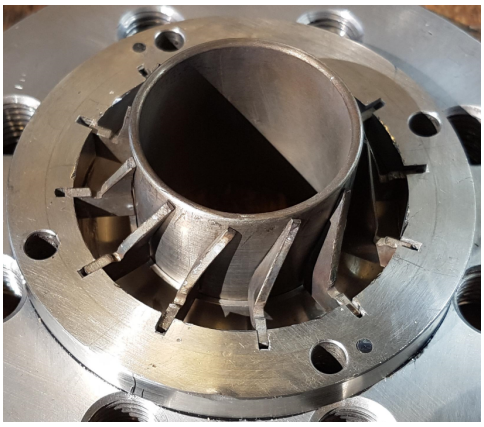

Figure 4.14: Swirl generator developed for the prevention of contact burning between cycles in the PDC. It is installed upstream of the wave reflector. The swirl generator was unsuccessful at preventing or suppressing contact burning.

the combination of centerbody, wave reflector, and injection slot reduced the flow back upstream during the initial flame propagation, resulting in the expanding gases supporting further flame acceleration.

4.5.4 Results of multi-cycle operation

Multi-cycle operation of the modular pulse detonation combustor proved to be a challenging endeavor. Investigations using the combination of wave reflector and shock-focusing nozzle with oxygen-enriched air could not surpass an operating frequency of 3 Hz. At higher frequencies, an event known as contact burning occurs for one or several cycles. Contact burning takes place when fresh fuel is injected and flows into a region with not only a sufficient amount of fresh oxidizer, but also a sufficient amount of product gases at high temperatures, still present from the previous cylce, to result in ignition. This may occur at any point from the fuel injection to the combustor exit, but the flame typically stabilizes at one position, coming to rest where the flow velocity matches the local turbulent flame speed. Increasing the mass flow rates in order to increase the purging of exhaust gases from areas of potential recirculation did not significantly improve the performance. In an attempt to change the flow field inside of the detonation tube, a swirl generator consisting of twelve interchangeable blades with angles of 20°, 30°, and 40° was installed just upstream of the injection slot (see Fig. 4.14). This also had no discernable effect on preventing the contact burning.

The operational domain of the PDC was then determined without oxygen-enrichment for a configuration with the wave reflector and eight orifice plates. This corresponds to a total length of the detonation chamber of 1,580 mm, including the 800 mm measurement section installed downstream of the orifice plates. The occurrence of DDT was determined using two ionization probes and two pressure transducers installed in the measurement section at alternating positions. The measurement positions were separated by a distance of 200 mm. This means 400 mm each between the two ionization probes and the two pressure transducers, respectively. Example signals from the ionization probes are shown for

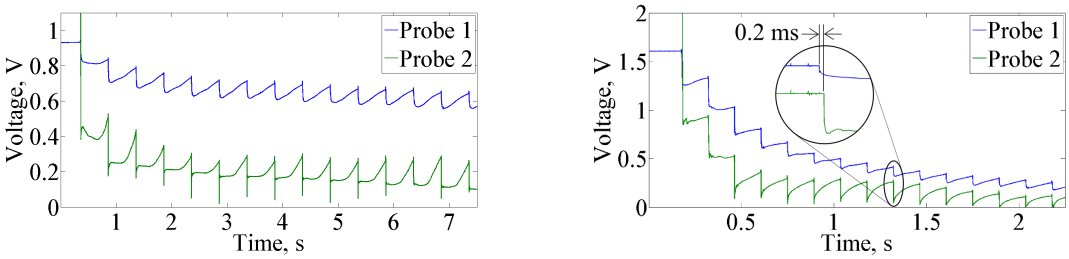

(a) Firing frequency of 2 Hz.

(b) Firing frequency of 7 Hz.

Figure 4.15: Signals from two ionization probes in the measurement section of the test bench for detonations at frequencies of 2 Hz and 7 Hz in stoichiometric hydrogen–air mixtures. Notice the more dramatic drift in the signal at the higher frequency. At separation distances of 400 mm, a time-of-flight of 0.2 ms corresponds to a velocity of 2000 m/s, just above the CJ velocity.

two operating conditions in Fig. 4.15. The initial voltage of the signal varied between runs and sensors. This may be affected by grounding issues within the ionization probe circuit or with the data aquisition system. Since this does not greatly affect the funtionality of this system, the issue was not investigated. At both operating frequencies, a negative drift in the signal is observed over the duration of the test run. This drift is more pronounced for operation at 7 Hz. This is due to insufficient time for the probe to once again obtain the voltage prior to one ignition event before the next event. The ionization probe is based upon a concept of charge buildup. When ionized gases persist long enough at the probe position, this buildup is in competition with the current flowing through the gases. As mentioned in Sec. 3.1.1, the current system is powered by a 9 V battery. The current is limited by a 2.7 $M\Omega$ resistor. This resistor may be sufficient to prevent the circuit from reattaining the initial value within a reasonable time. Updating the system with a dedicated power supply and a smaller resistor, would decrease the charging time of the circuit. For the frequencies obtained thus far, this is not an issue. The distinct voltage drop is still clearly seen in all signals. However, if higher operating frequencies are obtained in the future, the ionization probe system would likely have to be upgraded.

For the determination of the operation envelope, an operating condition is evaluated as successful if the detonation wave could be confirmed between the last two sensors in the measurement section for ten consecutive ignition events at the chosen operating frequency. If in one of ten events, the detonation is confirmed at the beginning of the measurement tube, but decouples before reaching the last sensor, the operating point is detemined to lie on the region boundary. This domain is illustrated in Fig. 4.16 and is separated into five regions. Measurement points are indicated by black dots.

The PID controller for the air supply could not provide a stable flow for mass flow rates of less than 20 kg/h. Beginning at this air mass flow rate, a steady increase of the operating frequency was possible up to 8 Hz for increasing mass flow rates. Above a certain frequency for every mass flow rate, the detonation wave is seen to decouple and lose velocity. This is due to the fact that the detonation wave enters into the region near the end of the tube where the equivalence ratio begins to decrease. The size of this region is based on the mass flow rate and the filling time. The leaner mixture is no longer

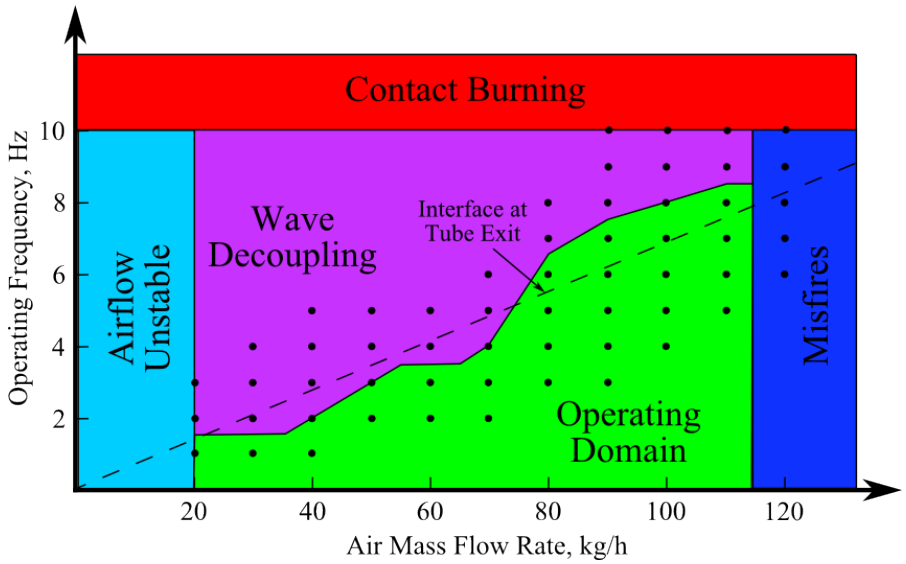

Figure 4.16: Operational envelope of the modular pulse detonation combustor test bench for stoichiometric hydrogen–air mixtures. Five different regions are depicted: four regions in which operation is hampered by various factors and the operating domain, where multi-cycle operation is possible without difficulty. The boundary between the operating domain and the point at which the shock wave decouples from the reaction zone corresponds very well to the theoretical interface between purge gases and reactive gases. A maximum operating frequency of 8 Hz was obtained.

conducive to sustaining a detonation. Assuming that the gases were to behave as a plug flow, there would exist a theoretical interface plane between the fresh gases and the purging air from the previous cycle. At a duty cycle of 50%, the frequency at which the interface plane exactly reaches the end of the detonation chamber for a respective mass flow rate is denoted by the dashed line. The equation from this line may be defined as

$$2f = \frac{\frac{\dot{m}_{\text{air}}}{\rho_{\text{air}}} + \frac{\dot{m}_{\text{H}_2}}{\rho_{\text{H}_2}}}{l\pi\frac{D^2}{2}}, \tag{4.2}$$

where the densities ρ_{air} and ρ_{H_2} are taken for atmospheric conditions, l is the length of the detonation chamber, and d is the tube diameter (40.3 mm). For stoichiometric conditions, $\dot{m}_{\text{H}_2} = 0.2925 \cdot \dot{m}_{\text{air}}$, making Eq. 4.3 simply a function of $\dot{m}_{\text{air}}$:

$$f = 0.0691 \left[\frac{1}{\text{kg}}\right] \cdot \dot{m}_{\text{air}}, \tag{4.3}$$

The boundary between the regions denoted “operating domain” and “wave decoupling” agrees fairly well with the trend of the theoretical interface plane.

At air mass flow rates in excess of 110 kg/h, the occurrence of misfires became common. A misfire is defined as an event in which the reactive mixture is not ignited by the spark. This is known to be the

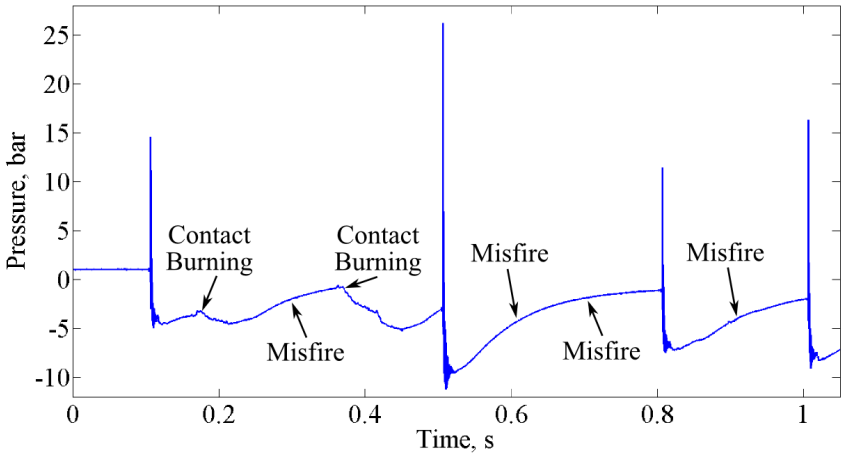

Figure 4.17: Failure modes in the PDC shown with the help of the signal from a single piezoelectric pressure sensor. Contact burning is identified by a non-physical decrease in the signal due to thermal loading of the sensor. A misfire is identified by a steady return of the signal to atmopheric conditions and the obvious absence of a detonation.

case when the turbulence or the velocity at the point of ignition is too high for sufficient heat transfer to the gas (Maly, 1984). Finally, in order to determine whether or not contact burning would occur in this configuration the frequency was increased. At around 10 Hz, contact burning was observed. This occurence appeared to be independent of mass flow rate, as was the case with the oxygen-enriched mixture. The fact that contact burning appears only at a higher frequency is likely due to the decreased pressure and temperature of the stoichiometric hydrogen–air mixture, compared to those of the oxygen-enriched mixture. The difference in misfires and contact burning can be determined by observing the signals from one of the pressure transducers. A test run at 10 Hz and 120 kg/h of air is shown in Fig. 4.17, illustrating both failure modes. Contact burning may be identified by a steady non-physical decrease in pressure not accompanied with a shock due to the thermal loading of the transducer. A misfire may be identified by the slow, unabated return of the pressure signal to atmospheric pressure. These two events proved to be the limiting factors for reliable multi-cycle operation of the modular pulse detonation combustor.

5 Conclusions

In the course of the work contained within this thesis, several topics were handled. Before developing a new program in pulse detonation combustion, initial investigations were conducted dealing with flame acceleration and DDT. Based on these findings, a modular pulse detonation combustion test rig was developed and studies were conducted using orifice plates as obstacles for producing DDT. Oxygen-enrichment was used to simulate the operating conditions in a micro gas turbine, increasing the reactivity of the fuel–oxidizer mixture. A novel, shock-focusing technique was developed and investigated in order to eliminate the need for turbulence creating obstacles. Finally, investigations were conducted for the multi-cycle operation of the test bench in various configurations.

Initial investigations dealing with flame acceleration and DDT of a stoichiometric hydrogen–air mixture offered several important findings. Some of these were useful in verifying those found in literature, some proved to enhance previous findings. The flame acceleration caused by a single obstacle proved to be predominantly due to the blockage ratio and independent of the geometry of the obstacle. The separation distance of multiple orifice plates with a blockage ratio of 0.43 resulting in optimum flame acceleration was somewhat over two tube diameters with a tube diameter of 30 mm. Experiments in a tube with 39 mm corroborated this separation distance, leading to reliable DDT with four orifice plates at a separation distance of 85 mm (2.18 tube diameters). The run-up distance for smaller tube diameters was beyond the length of the test bench. Although the application of virtual obstacles for DDT appeared promising based on initial flow field experiments conducted in a water test bench, reacting experiments proved difficult and this strategy was subsequently abandoned.

The modular pulse detonation test bench was successfully operated using eight orifice plates with a separation distance of 85 mm. The increased number of necessary orifice plates for reliable DDT was due to the valveless design of the test stand, decreasing the support of initial flame propagation. Introduction of a wave reflector geometry, serving as a fluidic diode at the inlet of the combustor, reduced the number of necessary orifice plates to six. Enriching the air to 40% oxygen by volume resulted in a further reduction of the number of orifice plates to two or three depending on the separation distance.

A shock-focusing concept was developed based on a geometry consisting of the aforementioned wave reflector and an axisymmetric, conical, converging-diverging nozzle with a converging area ratio of 4.0. The nozzle exhibited a convergent half-angle of 45°ànd a divergent half-angle of 4°. The combination of the wave reflector and shock-focusing nozzle proved to be very successful at producing DDT within a distance of only 158 mm for oxygen-enriched mixtures. This success is based on three different aspects of the geometry. First, the thin injection slot of 0.75 mm at the edge of the wave reflector results in a high injection velocity and a high level of turbulence. This leads to very high turbulent flame speeds immediately after ignition. Second, the fluidic diode characteristic of the wave reflector supports the further acceleration of the already relatively fast turbulent flame, as it prevents some of the pressure waves produced by the flame from traveling upstream and directs them instead back towards the flame. The combination of these two effects results in a fast accelerating turbulent flame over a very short distance. The velocity of the flame is sufficiently high for a leading shock to form. The third aspect of the geometry is then the focusing of the leading shock by the nozzle into a region ahead of the flame, producing an area of sufficiently high pressure and temperature to create a local explosion that propagates through the combustor in the form of a detonation wave. Pressure measurements, high-speed imagery, and high-speed shadowgraph measurements were used to characterize the process in more detail. This concept is not only unique in the extremly short DDT run-up length, but also in the means of producing the shock that is focused in the nozzle, namely by using a fast, accelerating turbulent flame.

Due to difficulties dealing with contact burning, multi-cycle operation using oxygen-enriched mixtures and the shock-focusing geometry was limited to 3 Hz. For a stoichiometric hydrogen-air mixture, the operating domain could be characterized up to a frequency of 10 Hz, at which contact burning also occurred for this mixture. Reliable DDT with a detonation wave still present between the last two sensors was achieved at frequencies up to 8 Hz for an air mass flow rate of 110 kg/h. Above this frequency, the detonation wave decouples towards the end of the combustor into a shock and a turbulent flame, as the equivalence ratio in this region becomes more lean.

A short and reliable means of producing DDT, such as that presented here, is imperative to the future of pulse detonation combustion applications. Proof of concept has been provided and the underlying mechanisms behind the success of this technique have been sufficiently explained. Once the problem of contact burning has been resolved and higher operating frequencies are able to be obtained, this concept is a promising technique for pulse detonation combustion applications.

6 Outlook and Future Work

The first immediate course of action for a follow-up of this work is to mitigate the problem of contact burning. This is most severe for the case of oxygen-enriched air, limiting the operating conditions of the PDC to only 3 Hz. As the exact location of the origin of contact burning was not able to be ascertained, this work was considered inconclusive. For this reason, it is included in this section of the thesis, rather than with the results. However, it was determined that two factors contributed to the problem at hand. First, the presence of a combustible mixture upstream of the injection slot allowed the flame to travel into the mixing chamber immediately after ignition. This was not able to be avoided, as closing the injection valves slightly before ignition led to an increasing number of misfires and delays of merely 3 ms prevented controlled operation of the combustor. These misfires were due to the mixture at the point of ignition already being to lean. Second, the high pressures in the detonation chamber during flame propagation and after DDT forced even more hot exhaust gases upstream into the mixing chamber, well beyond the point of fuel injection, shown in Fig. 6.1. These gases were not able to be sufficiently purged and were able to be seen in the images at times beyond 100 ms after ignition. A constricting cross-section just downstream of the hydrogen injection followed by a sufficiently long section before the entrance to the detonation chamber may prevent both the flame and high-pressure exhaust gases from penetrating so far upstream as well as allow for a more controlled timing of the fuel injection.

For the continuation of pulse detonation combustion within SFB 1029, a test bench has been designed with multiple detonation tubes in order to investigate tube–tube interaction at multi-cycle operating conditions. Nicholls et al. (1957) envisioned such a concept even at the very dawn of PDC research and several investigations have been conducted by various groups in recent years (Rasheed et al., 2011; Lu et al., 2015). A newly designed test bench (see Fig. 6.2) will be used to study various firing frequencies and strategies. Additionally, a plenum has been forseen to damp the high pressure fluctuations inherent to this combustion process before entrance into a turbine. This plenum will also be the object of further investigations.

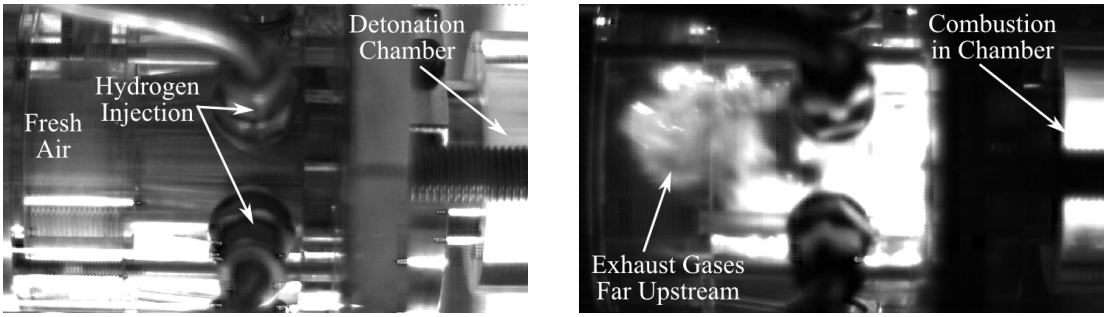

(a) Image of upstream geometry constructed out of acrylic glass.

(b) Image after ignition.

Figure 6.1: Image illustrating the extent to which hot exhaust gases are forced upstream during an ignition event. These exhaust gases are not sufficiently purged and lead to contact burning during hydrogen injection in the subsequent cycle.

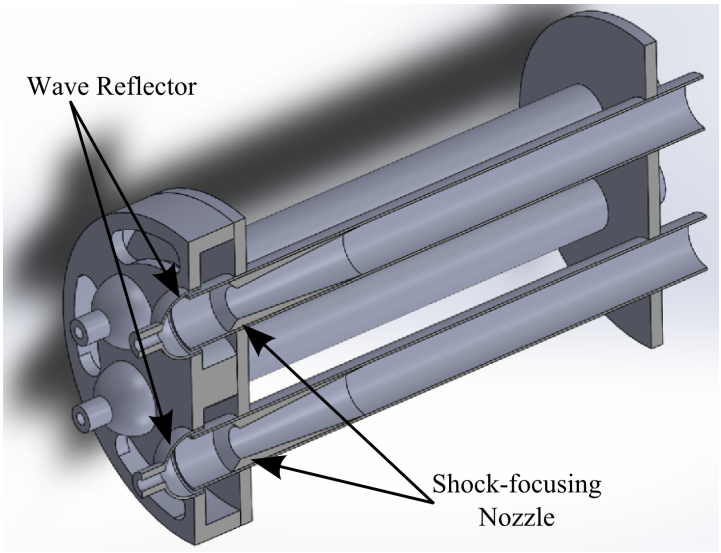

Figure 6.2: Conceptual drawing of a multi-tube pulse detonation combustor.

As mentioned in Sec. 2.5, detonation cell width is not only a function of mixture, but also a function of pressure and temperature. Using oxygen enrichment, this cell width has been matched in the current work for that at operating conditions in a micro gas turbine. However, exactly what implications pressure and temperature effects will have on the run-up distance and on the DDT process itself are not known. Therefore, it is imperative that the process be investigated at increased pressure and temperature. This is planned on both the current test bench and an intermediate pressure test bench within the framework of SFB 1029.

The various uses of hydrogen in power-to-gas applications were discussed in Sec. 1.1. One of these was the addition of hydrogen to natural gas. Another was the methanation of hydrogen. Both of these paths indicate that methane may still play a role in combustion energy in the near future. However, methane is extremely insensitive to detonation, with cell widths at atmospheric conditions exceeding 200 mm (see Fig. 2.6). Experimental investigations of cell width at elevated pressure and temperature is a topic of ongoing investigation (Stevens et al., 2014). Mixtures of hydrogen and methane may provide sufficiently small cell widths for utilization in PDCs. These investigations should be continued at TU Berlin at atmospheric pressure for high hydrogen concentrations transitioning to elevated pressures and temperatures for subsequently lower hydrogen concentrations.

As mentioned in Sec. 1.2, the high temperatures due to the extreme detonative combustion process are counterproductive to today's standards of lowering emissions of NO_x. Initial computational studies indicated that a PDC operated on pure hydrogen–air would result in NO_x emissions in excess of 1000 ppm (Hanraths, 2013). This is orders of magnitude above state-of-the-art gas turbine limits today, which have reached levels below 10 ppm. Methods of mitigating these emissions are to be investigated on the current test bench and at elevated pressures. These methods include the simulation of exhaust gas recirculation by injection of excess nitrogen to the mixture as well as steam injection. Although being proven as successful methods in the gas turbine industry for decreasing NO_x emissions, both of these methods have a negative impact on the reactivity of detonative mixtures. This impact is to be characterized as well as the effectiveness of the respective methods in decreasing emissions. Lowering the combustion temperature using hydrogen–methane mixtures may also have a positive influence in conjunction with these methods.

Finally, through collaboration with the Clean Combustion Research Center at King Abdullah University of Science and Technology[1], preliminary investigations have been conducted on the use of nanosecond repetitively pulsed (NRP) plasma discharges for enhancing DDT. Initial tests have delivered promising results indicating that DDT is indeed enhanced and that NRP plasma may successfully replace orifice plates if properly utilized.

[1] Assistant Professor Deanna Lacoste

Bibliography

Achasov, O., Kondrasov, V., and Penyazkov, O. (1997). Direct Initiation of Gaseous Detonation by Interacting Supersonic Jets. *IUTAM Symposium on Combustion in Supersonic Flows, eds. M. Champion and B. Deshaies*, 39:359–363.

Achasov, O. V., Labuda, S. A., Penyaz'kov, O. G., Pushkin, P. M., and Tarasov, A. I. (1994). Initiation of Detonation in Reflection of a Shock Wave from a Concave Curvilinear Surface. *Journal of engineering physics and thermophysics*, 67(1):739–744.

Agora (2014). Website, Agora Energiewende: https://www.agora-energiewende.de/.

Angrist, S. (1964). Fluid Control Devices. *Scientific American*, (211):80–89.

Barnard, J. A. and Bradley, J. N. (1984). *Flame and Combustion*. Springer US, Boston, MA.

Barr, L. (2008). Pulse Detonation Engine Flies into History. *Press Release, Air Force Material Command*.

Becker, R. (1917). Zur Theorie der Detonation (in German). *Z. Elektrochemie*, 23(40-49).

Becker, R. (1922). Stosswelle und Detonation (in German). *Zeitschrift für Physik*, 8(1):321–362.

Becker, R. (1936). Über Detonation (in German). *Z. Elektrochemie*, 76:457–461.

Berthelot, M. and Vieille, P. (1882). Sur la vitesse des propagation des phenomenes explosifs dans le gaz (in French). *Compt. Rend. Acad. Sci. Paris*, 94:101–108.

Birman, V. (1996). Thermal Effects on Measurements of Dynamic Processes in Composite Structures using Piezoelectric Sensors. *Smart materials and structures*, 5(4):379.

Bobusch, B. (2015). Fluidic Devices for Realizing the Shockless Explosion Combustion Process, Ph.D. Thesis, TU Berlin.

Bobusch, B. C., Woszidlo, R., Bergada, J. M., Nayeri, C. N., and Paschereit, C. O. (2013). Experimental Study of the Internal Flow Structures inside a Fluidic Oscillator. *Experiments in Fluids*, 54(6):1559.

Borisov, A. (1999). Initiation of Detonation in Gaseous and Two-Phase Mixtures. In Roy, G., Frolov, S., Kailasanath, K., and Smirnov, N., editors, *Gaseous and Heterogeneous Detonations: Science to Applications*, pages 3–24. ENAS Publishers, Moscow.

Bray, K. N. C. (1990). Studies of the Turbulent Burning Velocity. *Proceedings of the Royal Society A: Mathematical, Physical and Engineering Sciences*, 431(1882):315–335.

Brokaw, R. S. (1968). Viscosity of Gas Mixtures, NASA Technical Note D-4496.

Burke, M. P., Chaos, M., Ju, Y., Dryer, F. L., and Klippenstein, S. J. (2012). Comprehensive H2/O2 Kinetic Model for High-Pressure Combustion. *International Journal of Chemical Kinetics*, 44(7):444–474.

Campbell, C. and Woodhead, D. W. (1926). CCCCI.—The Ignition of Gases by an Explosion-Wave. Part I. Carbon Monoxide and Hydrogen Mixtures. *Journal of the Chemical Society (Resumed)*, 129:3010–3021.

CCES (2017). Website, Center for Climate and Energy Solutions: https://www.c2es.org/technology/factsheet/natural-gas.

Chan, C. K., Dewit, W. A., and Koroll, G. W. (1995). Criteria for Transition from Deflgration to Detonation in H2-Air-Steam Mixtures. In *ICHMT Digital Library Online*. Begel House Inc.

Chan, C. K., Lau, D., Thibault, P. A., and Penrose, J. D. (1990). Ignition and Detonation Initiation by Shock Focussing. volume 208, pages 161–166.

Chapman, D. L. (1899). VI. On the Rate of Explosion in Gases. *The London, Edinburgh, and Dublin Philosophical Magazine and Journal of Science*, 47(284):90–104.

Chew, T. C., Britter, R. E., and Bray, K. N. C. (1989). Laser Tomography of Turbulent Premixed Bunsen Flames. *Combustion and Flame*, 75(2):165–174.

Ciccarelli, G., Boccio, J. L., Ginsberg, T., Finfrock, C., Gerlach, L., Tagawa, H., and Malliakos, A. (1995). Hydrogen Detonation and Detonation Transition Data from the High-Temperature Combustion Facility. Technical report, Brookhaven National Lab., Upton, NY (United States).

Ciccarelli, G. and Dorofeev, S. (2008). Flame Acceleration and Transition to Detonation in Ducts. *Progress in Energy and Combustion Science*, 34(4):499–550.

Cooper, M., Jackson, S., Austin, J., Wintenberger, E., and Shepherd, J. E. (2002). Direct Experimental Impulse Measurements for Detonations and Deflagrations. *Journal of propulsion and power*, 18(5):1033–1041.

Crussard, J. (1907). Sur Quelque Propriétés de l'Onde Explosive (in French). *Comptes-Rendus Académie des Sciences*, 144:417–420.

Denisov, Y. and Troshin, Y. (1959). Pulsating and Spinning Detonation in Channels (Original in Russian). *Dokl. Akad. Nauk SSSR*, 125:110–113.

Döring, W. (1943). Über den Detonationsvorgang in Gasen (in German). *Annalen der Physik*, 435(6-7):421–436.

Driscoll, R., Stoddard, W., St. George, A., Munday, D., and Gutmark, E. (2013). Experimental Study of Sustained Shock Initiated Detonation in a Multiple Pulse Detonation-Crossover System. 51st AIAA Aerospace Sciences Meeting.

Eriksson, L. and Nielsen, L. (1997). Ionization Current Interpretation for Ignition Control in Internal Combustion Engines. *Control Engineering Practice*, 5(8):1107–1113.

Frolov, S. and Gelfand, B. (1993). Limiting Tube Diameter of Gaseous Detonation. In Kuhl, A. L., Borisov, A. A., Leyer, J.-C., and Sirignano, W. A., editors, *Dynamic Aspects of Detonations*, pages 298–311. American Institute of Aeronautics and Astronautics, Washington DC.

Frolov, S. M. (2014). Natural-Gas-Fueled Pulse-Detonation Combustor. *Journal of Propulsion and Power*, 30(1):41–46.

Frolov, S. M. and Aksenov, V. S. (2009). Initiation of Gas Detonation in a Tube with a Shaped Obstacle. *Doklady Physical Chemistry*, 427(1):129–132.

Gelfand, B., Khomik, S., Bartenev, A., Medvedev, S., Grönig, H., and Olivier, H. (2000). Detonation and Deflagration Initiation at the Focusing of Shock Waves in Combustible Gaseous Mixture. *Shock Waves*, 10(3):197–204.

Gülen, S. C. (2016). Étude on Gas Turbine Combined Cycle Power Plant—Next 20 Years. *Journal of Engineering for Gas Turbines and Power*, 138(5):051701.

Goodwin, D. G., Moffat, H. K., and Speth, R. L. (2016). Cantera: An Object-Oriented Software Toolkit for Chemical Kinetics, Thermodynamics, and Transport Processes. http://www.cantera.org. Version 2.2.1.

Gordon, S. and McBride, B. (1996). Computer Program for Calculation of Complex Chemical Equilibrium Compositions and Applications. NASA Reference Publication 1311.

Gray, J., Moeck, J., and Paschereit, C. (2014). Non-Reacting Investigations of a Pseudo-Orifice for the Purpose of Enhanced Deflagration-to-Detonation Transition. In Roy, G. and Frolov, S., editors, *Transient Combustion and Detonation Phenomena: Fundamentals and Applications*, Combustion and Detonation, pages 176–181. Torus Press.

Gray, J. A. T., Vinkeloe, J., Moeck, J., Paschereit, C. O., Stathopoulos, P., Berndt, P., and Klein, R. (2016). Thermodynamic Evaluation of Pulse Detonation Combustion for Gas Turbine Power Cycles. In *ASME Turbo Expo 2016: Turbomachinery Technical Conference and Exposition*. American Society of Mechanical Engineers.

Guirao, C. M., Knystautas, R., and Lee, J. H. S. (1989). *A Summary of Hydrogen-Air Detonation Experiments*. Division of Systems Research, Office of Nuclear Regulatory Research, US Nuclear Regulatory Commission.

Hanraths, N. (2013). Parameterstudie zur Emission bei der Simulation einer 1d-Pulsdetonationsbrennkammer mit Wasserstoff-Luft-Gemisch, Bachelor's Thesis, TU Berlin (in German).

Heiser, W. H. and Pratt, D. T. (2002). Thermodynamic Cycle Analysis of Pulse Detonation Engines. *Journal of Propulsion and Power*, 18(1):68–76.

Helman, D., Shreeve, R., and Eidelman, S. (1986). Detonation Pulse Engine. AIAA/ASME/SAE/ASEE 22nd Joint Propulsion Conference.

Hoffmann, H. (1940). Reaction-Propulsion Produced by Intermittent Detonative Combustion, Rept. ATI-52365, German Research Institute for Gliding, Ministry of Supply (Original in German, Volkenrode Translation).

Hooke, R. (1665). *Micrographia*. J. Martyn & J. Allestry, London.

Jackson, S. I., Buraczewski, P. M., and Shepherd, J. E. (2005). Initiation of Detonations and Deflagrations by Shock Reflection and Focusing. 20th International Colloquium on the Dynamics of Explosions and Reactive Systems.

Janka, A. (2014). Methods of Diffusing Pulse Detonation Combustion, Ph.D. Thesis, Virginia Polytechnic Institute and State University.

John, J. E. A. (1984). *Gas Dynamics*. Allyn and Bacon series in engineering. Allyn and Bacon, Boston, 2nd edition.

Jones, S. M. and Welch, G. E. (1996). Performance Benefits for Wave Rotor-Topped Gas Turbine Engines. ASME International Gas Turbine and Aeroengine Congress and Exhibition.

Jouguet, E. (1905). Sur la propagation des réactions chimiques dans les gaz (in French). *Journal de Mathématiques Pures et Appliquées*, 6(1):347–425.

Kailasanath, K. (2000). Review of Propulsion Applications of Detonation Waves. *AIAA journal*, 38(9):1698–1708.

Kailasanath, K. (2009). Research on pulse detonation combustion systems–a status report. *AIAA paper*, 631:2009.

Kaneshige, M. and Shepherd, J. E. (1997). Detonation Database. Technical Report FM97-8, GALCIT.

Kao, S. and Shepherd, J. E. (2008). Numerical Solution Methods for Control Volume Explosions and ZND Detonation Structure. *GALCIT Report FM2006.007*.

Knox, B. W., Forliti, D. J., Stevens, C. A., Hoke, J. L., and Schauer, F. R. (2010). Unsteady Flame Speed Control and Deflagration-to-Detonation Transition Enhancement using Fluidic Obstacles. *AIAA Journal*, (151):1–9.

Knox, B. W., Forliti, D. J., Stevens, C. A., Hoke, J. L., and Schauer, F. R. (2011). A Comparison of Fluidic and Physical Obstacles for Deflagration-to-Detonation Transition. In *49th AIAA Aerospace Sciences Meeting*.

Knystautas, R., Guirao, C., and Lee, J. H. (1985). Measurements of Cell Size in Hydrocarbon–Air Mixtures and Predictions of Critical Tube Diameter, Critical Initiation Energy, and Detonability Limits. In Bowen, J., Manson, N., Oppenheim, A., Soloukhin, R., and Sulmistras, A., editors, *Dynamics of Shock Wave, Explosions, and Detonations*.

Knystautas, R. and Lee, J. (1976). On the Effective Energy for Direct Initiation of Gaseous Detonations. *Combustion and Flame*, 27:221–228.

Kowalkowski, M., Matsutomi, Y., and Heister, S. (2009). Flame Sensing in Pulsed Combustion Using Ion Probes, Diodes and Visual Indications. In *45th AIAA/ASME/SAE/ASEE Joint Propulsion Conference & Exhibit*, page 4945.

Krehl, O.K., P. (2009). *History of Shock Waves, Explosions and Impact*. Springer Berlin Heidelberg.

Lee, J. H. (1984). Dynamic Parameters of Gaseous Detonations. *Annual Review of Fluid Mechanics*, 16(1):311–336.

Lee, J. H., Knystautas, R., and Chan, C. K. (1985). Turbulent Flame Propagation in Obstacle-Filled Tubes. In *Symposium (International) on Combustion*, volume 20, pages 1663–1672. Elsevier.

Lee, J. H., Knystautas, R., and Yoshikawa, N. (1978). Photochemical Initiation of Gaseous Detonations. *Acta Astronautica*, 5(11-12):971–982.

Lee, J. H. and Matsui, H. (1977). A Comparison of the Critical Energies for Direct Initiation of Spherical Detonations in Acetylene–Oxygen Mixtures. *Combustion and Flame*, 28:61–66.

Lee, J. H. S. (2008). *The Detonation Phenomenon*. Cambridge University Press, Cambridge; New York. OCLC: 252236721.

Litchfield, E. L., Hay, M. H., and Forshey, D. R. (1963). Direct Electrical Initiation of Freely Expanding Gaseous Detonation Waves. In *Ninth Symposium (International) on Combustion*, pages 282–286.

Litke, P., Schauer, F., Paxson, D., Bradley, R., and Hoke, J. (2005). Assessment of the Performance of a Pulsejet and Comparison with a Pulsed-Detonation Engine. In *43rd AIAA Aerospace Sciences Meeting and Exhibit*.

Lu, F. K. and Braun, E. M. (2014). Rotating Detonation Wave Propulsion: Experimental Challenges, Modeling, and Engine Concepts. *Journal of Propulsion and Power*, 30(5):1125–1142.

Lu, J., Zheng, L., Wang, Z., Peng, C., and Chen, X. (2015). Operating Characteristics and Propagation of Back-Pressure Waves in a Multi-Tube Two-Phase Valveless Air-Breathing Pulse Detonation Combustor. *Experimental Thermal and Fluid Science*, 61:12–23.

Mallard, E. and Le Chatelier, H. (1883). Recherches experimentales et theoretiques sur la combustion des melange gaseux explosifs (in French). *Ann. Mines*, 8(4):274–568.

Maly, R. (1984). Spark Ignition: Its Physics and Effect on the Internal Combustion Engine. In Hilliard, J. C. and Springer, G. S., editors, *Fuel Economy in Road Vehicles Powered by Spark Ignition Engines*, pages 91–145. Springer Science + Business Media, LLC.

Melaina, M. W., Antonia, O., and Penev, M. (2013). Blending Hydrogen into Natural Gas Pipeline Networks: A Review of Key Issues. Technical report, National Renewable Energy Laboratory.

Michelson, W. (1889). Ueber die normale Entzündungsgeschwindigkeit explosiver Gasgemischen (in German). *Annalen der Physik*, 273(5):1–24.

Ng, H., Ju, Y., and Lee, J. (2007). Assessment of Detonation Hazards in High-Pressure Hydrogen Storage from Chemical Sensitivity Analysis. *International Journal of Hydrogen Energy*, 32(1):93–99.

Ng, H. D., Radulescu, M. I., Higgins, A. J., Nikiforakis, N., and Lee, J. H. S. (2005). Numerical Investigation of the Instability for One-Dimensional Chapman–Jouguet Detonations with Chain-Branching Kinetics. *Combustion Theory and Modelling*, 9(3):385–401.

Nicholls, J. A., Wilkinson, H. R., and Morrison, R. B. (1957). Intermittent Detonation as a Thrust-Producing Mechanism. *Journal of Jet Propulsion*, 27(5):534–541.

Ono, R., Nifuku, M., Fujiwara, S., Horiguchi, S., and Oda, T. (2007). Minimum Ignition Energy of Hydrogen–Air Mixture: Effects of Humidity and Spark Duration. *Journal of Electrostatics*, 65(2):87–93.

Oppenheim, A. K., Laderman, A. J., and Urtiew, P. A. (1962). The Onset of Retonation. *Combustion and Flame*, 6:193–197.

Oppenheim, A. K. and Soloukhin, R. I. (1973). Experiments in Gasdynamics of Explosions. *Annual Review of Fluid Mechanics*, 5(1):31–58.

Panicker, P. K. (2008). The Development and Testing of Pulsed Detonation Engine Ground Demonstrators, Ph.D. Thesis, University of Texas at Arlington.

Panicker, P. K., Wilson, D. R., and Lu, F. K. (2006). Operational Issues Affecting the Practical Implementation of Pulsed Detonation Engines. In *14th AIAA/AHI Space Planes and Hypersonic Systems and Technologies Conference*.

Paxson, D., Schauer, F., and Hopper, D. (2009). Performance Impact of Deflagration to Detonation Transition Enhancing Obstacles. In *47th AIAA Aerospace Sciences Meeting including The New Horizons Forum and Aerospace Exposition*.

Peraldi, O., Knystautas, R., and Lee, J. H. (1986). Criteria for Transition to Detonation in Tubes. *Twenty-first Symposium (International) on Combustion*, pages 1629–1637.

Rasheed, A., Furman, A. H., and Dean, A. J. (2011). Experimental Investigations of the Performance of a Multitube Pulse Detonation Turbine System. *Journal of Propulsion and Power*, 27(3):586–596.

Roy, G., Frolov, S., Borisov, A., and Netzer, D. (2004). Pulse Detonation Propulsion: Challenges, Current Status, and Future Perspective. *Progress in Energy and Combustion Science*, 30(6):545–672.

Salas, M. D. (2009). *A Shock-Fitting Primer*. CRC Press.

Schaaf, T., Grünig, J., Schuster, M. R., Rothenfluh, T., and Orth, A. (2014). Methanation of CO2 - Storage of Renewable Energy in a Gas Distribution System (Online) https://doi.org/10.1186/s13705-014-0029-1. *Energy, Sustainability and Society*, 4(1).

Schauer, F., Stutrud, J., and Bradley, R. (2001). Detonation Initiation Studies and Performance Results for Pulsed Detonation Engine Applications. In *39th AIAA Aerospace Sciences Meeting and Exhibit*.

Schultz, E. and Shepherd, J. (2000). Validation of Detailed Reaction Mechanisms for Detonation Simulation. *GALCIT Technical Report, FM99-05, California Institute of Technology, USA*.

Settles, G. S. (2001). *Schlieren and Shadowgraph Techniques*. Springer Berlin Heidelberg, Berlin, Heidelberg.

Shchelkin, K. I. (1949). Rapid Combustion and Spin Detonation in Gases. Moscow, Voenizdat.

Shchelkin, K. I. and Troshin, Y. K. (1965). *Gas Dynamics of Combustion. English Translation by B.W. Kuvshinoff and L. Holtschlag*. Mono Book Corp., Baltimore.

Shepherd, I. (1996). Flame Surface Density and Burning Rate in Premixed Turbulent Flames. *Symposium (International) on Combustion*, 26(1):373–379.

Shy, S., Lin, W., and Peng, K. (2000). High-Intensity Turbulent Premixed Combustion: General Correlations of Turbulent Burning Velocities in a New Cruciform Burner. *Proceedings of the Combustion Institute*, 28(1):561–568.

Soria, J. (1996). An Investigation of the Near Wake of a Circular Cylinder using a Video-Based Digital Cross-Correlation Particle Image Velocimetry Technique. *Experimental Thermal and Fluid Science*, 12(2):221–233.

Stevens, C. A., Hoke, J., and Schauer, F. (2014). Cell Width of Methane Air Mixtures at Elevated Initial Pressure and Temperature. In *52nd AIAA Aerospace Sciences Meeting*.

Stoddard, W., St. George, A. C., Driscoll, R. B., Anand, V., and Gutmark, E. J. (2016). Experimental Validation of Expanded Centerbodiless RDE Design. In *54th AIAA Aerospace Sciences Meeting*.

Strehlow, R. A. and Crooker, A. J. (1974). The Structure of Marginal Detonation Waves. *Acta Astronautica*, 1(3-4):303–315.

Teodorczyk, A., Drobniak, P., and Dabkowski, A. (2009). Fast Turbulent Deflagration and DDT of Hydrogen–Air Mixtures in Small Obstructed Channel. *International Journal of Hydrogen Energy*, 34(14):5887–5893.

Urtiew, P. A. and Oppenheim, A. K. (1966). Experimental Observations of the Transition to Detonation in an Explosive Gas. *Proceedings of the Royal Society A: Mathematical, Physical and Engineering Sciences*, 295(1440):13–28.

von Neumann, J. (1942). Progress Report to the National Defense Research Committee Div. B, OSRD-549 (April 1, 1942. PB 31090).

White, D. R. (1961). Turbulent Structure of Gaseous Detonation. *Physics of Fluids*, 4(4):465.

Willert, C. E. and Gharib, M. (1991). Digital Particle Image Velocimetry. *Experiments in Fluids*, 10(4):181–193.

Willert, C. E., Mitchell, D. M., and Soria, J. (2012). An Assessment of High-Power Light-Emitting Diodes for High Frame Rate Schlieren Imaging. *Experiments in Fluids*, 53(2):413–421.

Wintenberger, E. and Shepherd, J. E. (2006). Thermodynamic Cycle Analysis for Propagating Detonations. *Journal of Propulsion and Power*, 22(3):694–698.

Zdenek, J. and Anthenien, R. (2004). Ion Based High-Temperature Pressure Sensor. In *42nd AIAA Aerospace Sciences Meeting and Exhibit*.

Zel'dovich, Y. B. (1940a). On the Theory of the Propagation of Detonations on Gaseous System (Original in Russian). *Journal of Experimental and Theoretical Physics*, 10:542–568.

Zel'dovich, Y. B. (1940b). To the Question of Energy use of Detonation Combustion (original in Russian). *Zhurnal tekhnicheskoi fiziki (Journal of Technical Physics)*, 10(17):1453–1461.

Zel'dovich, Y. B. (1944). Teoriya goreniya i detonatsii gazov (Theory of Combustion and Detonation of Gases, in the USSR).

Zel'dovich, Y. B., Librovich, V., Makhviladze, G., and Sivashinsky, G. (1970). On the Development of Detonation in a Non-Uniformly Preheated Gas. *Astronaut Acta*, 15:313–321.

Zeleznik, F. J. (1962). Calculation of Detonation Properties and Effect of Independent Parameters on Gaseous Detonations. *ARS Journal*, 32(4):606–615.

Zhang, Y., Chew, T., and Bray, K. N. C. (1988). Particle Image Displacement Velocimetry, Lecture Series at von Karman Institute for Fluid Dynamics, Belgium.